Spontaneous Pattern Formation in Photoelectrodeposited Semiconductor Films

Thesis by
Nicolas Anthony Batara

In Partial Fulfillment of the Requirements for the
degree of
Doctor of Philosophy

CALIFORNIA INSTITUTE OF TECHNOLOGY
Pasadena, California

2017
(Defended October 24th, 2016)

Nicolas Anthony Batara
ORCID: 0000-0002-9154-4577

ACKNOWLEDGEMENTS

This work would not have been possible without the support of numerous colleagues, friends and family members. First and foremost, I would like to thank my advisors Harry Atwater and Nate Lewis for their erudite advising, boundless optimism and encouragement to develop my own scientific identity. Additionally, I am deeply grateful to my undergraduate mentors at UCSB, Moriah Sandy, Allison Butler, Alessandro Varotto and Fred Wudl, whom introduced me to the practice of academic research. My graduate mentor and collaborator Bryce Sadtler taught me the importance of being deeply aware and personally engaging in one's reseach field. My close collaborator and friend Azhar Carim was willing to thoughtfully discuss this research at any hour of the day. Departmental and group staff members Christy Jenstad, Tiffany Kimoto, Jennifer Blankenship, Liz Jennings, Lyann Lau and Barbara Miralles worked tirelessly to foster an inclusive, productive and fun workplace which is integral to Caltech's eminence.

There are so many talented graduate students, post-docs and staff scientists I've had the privilege of meeting and learning from. I would like to explictly thank my first year office-mates and fellow p-set warriors Saurabh Bajaj, Fadl Saadi, Sam Johnson, David Chen, Erik Verlage, Sunita Darbe, Andrew Hoff, John Lloyd, Fadl Saadi, Ana Brown and Chen Xu for their solidarity, comedy and support while making our way through rigorous course-work. Additionally, Atwater group office-mates Jeff Bosco, Sam Wilson, Seyoon Kim, Yulia Tolstova, Colton Bukowsky and Muhammad Alam and the Lewis and Atwater groups in general, consistently made it a pleasure to come to work and practice science.

Most personally, I would like to thank my family and friends for their love and for encouraging me to follow my interests while remaining open to a broad range of perspectives. Lastly, I would like to thank my extraordinary partner Kelsey Murphy who helped me grow in so many ways, strive for balance, seek support, and self-reflect during the difficult periods of my graduate career.

This work was supported by the "Light-Material Interactions in Energy Conversion" Energy Frontier Research Center funded by the U.S. Department of Energy, Office of Science, Office of Basic Energy Sciences under Award Number DE-SC0001293.

Nicolas A. Batara
Fall 2016, Pasadena, CA

ABSTRACT

The ability to manipulate matter with ever-increasing precision has enabled the fabrication of nanoscale structures with unprecedented utility. Scalable patterning technologies have dramatically transformed diverse application spaces such as computing and photonics, in part due to diminishing cost per unit area. The work in this thesis presents a template-free, bottom-up technique based on photoelectrodeposition which allows the direct fabrication of periodically nanostructured thin films of semiconductor material over large areas.

First, we examine the effects of wavelength, polarization and incidence angle of illumination on the film morphology. We develop an understanding of the pattern formation to be the result of interference of light scattered across the surface of the growing interface. We also examine the morphological effects of more complex illumination conditions. For example, when deposited under two different illumination wavelengths, the period of patterned films self-optimizes to concentrate light absorption to the tips of the nanostructures . Additionally, we find that the relative polarization angles and phases of two illumination sources can be tuned to produce film morphologies ranging from isotropic mesh-type patterns to orthogonally arranged, intersecting lamellar structures with independent periodicities.

We deepen our understanding of these observations by building a probabilistic computational model that correlates the local light absorption with a local growth probability at the interface of the film with few material parameters. We find that this model is able to reproduce experimentally observed morphological features for all illumination conditions investigated in this work. Through Fourier analysis, we find quantitative agreement between the simulated and experimental periods. Separately, we use electrodynamic simulations on idealized lamellar structures to understand the effect of two coincident illumination sources on the spatial absorption profile.

PUBLISHED CONTENT AND CONTRIBUTIONS

The chapters in this thesis have been drawn from the following publications. N.A.B. performed all computational work, except that of section 2.2, and contributed to the writing of each manuscript.

1. Sadtler, B., Burgos, S. P., Batara, N. A., Beardslee, J. A., Atwater, H. A. & Lewis, N. S. Phototropic growth control of nanoscale pattern formation in photoelectrodeposited Se-Te films. *Proceedings of the National Academy of Sciences of the United States of America* **110,** 19707–19712 (Dec. 2013). doi: 10.1073/pnas.1315539110.

2. Carim, A. I., Batara, N. A., Premkumar, A., Atwater, H. A. & Lewis, N. S. Self-Optimizing Photoelectrochemical Growth of Nanopatterned Se–Te Films in Response to the Spectral Distribution of Incident Illumination. *Nano Letters* **15,** 7071–7076 (Oct. 2015). doi: 10.1021/acs.nanolett.5b03137.

3. Carim, A. I., Batara, N. A., Premkumar, A., Atwater, H. A. & Lewis, N. S. Polarization Control of Morphological Pattern Orientation During Light-Mediated Synthesis of Nanostructured Se–Te Films. *ACS Nano* **10,** 102–111 (Jan. 2016). doi: 10.1021/acsnano.5b05119.

4. Carim, A. I., Batara, N. A., Premkumar, A., May, R., Atwater, H. A. & Lewis, N. S. Morphological Expression of the Coherence and Relative Phase of Optical Inputs to the Photoelectrodeposition of Nanopatterned Se–Te Films. *Nano Letters* **16,** 2963–2968 (May 2016). doi: 10.1021/acs.nanolett.5b04999.

TABLE OF CONTENTS

LIST OF ILLUSTRATIONS

LIST OF TABLES

Chapter 1

INTRODUCTION

1.1 State of the Art in Nanoscale Semiconductor Patterning

The ability to manipulate matter with ever-increasing precision has enabled the fabrication of nanoscale structures with unprecedented utility. Scalable patterning technologies have dramatically transformed diverse application spaces such as computing, renewable energy, and photonics among others, in-part due to diminishing cost per unit area.

Commercial semiconductor patterning currently relies on photolithography, where regions of a photoresist are selectively exposed to electromagnetic radiation. In this technique a lithographic mask is used to spatially localize photochemical reactions [1–3]. Recent extensions of photolithography, such as plasmonic nanolithography and interference lithography, have enabled the generation of three-dimensional light intensity patterns and have thus been used to fabricate more complex structures with feature sizes below 100 nm [4–9]. However, these top-down photopatterning approaches require a different mask design to create each new structure and typically are used in combination with a separate non area-selective deposition or etching process.

To address these processing complexities, maskless methods have been investigated that rely on the manipulation of localized illumination, such as direct-write methods and photoelectrochemical etching based on scanning laser illumination [10–13]. These methods can produce arbitrary two-dimensional patterns but are not generally amenable for processing over large areas.

Alternatively, anisotropic light-material interactions can be utilized as the basis for patterning structures. In addition to variation of the local illumination intensity, other properties of the incident optical field such as the wavelength, polarization, and coherence of the illumination can be used to generate unique morphologies in response to variations to the optical excitation. These processes provide multiple physical input parameters that may be varied concurrently, or in sequential combination, to direct the formation of an intended structure [14–16]. More specifically, techniques have been developed for patterning surfaces via photoinduced ablation, melting, deposition, and etching. Periodic ripple patterns have been observed during

laser-induced damage, melting, and etching of dielectric and metal surfaces as well as for photolytic decomposition of organometallic precursors onto these substrates [17–25]. Laser-induced periodic surface structuring (LIPSS, also referred to as the stimulated Wood's anomaly) resulting from interference between an intense laser source (i.e., between 10 W/cm^2 and 10 MW/cm^2 for continuous laser irradiation or between 75 and 800 mJ/cm^2 per pulse for pulsed irradiation in the above references) and surface-scattered waves to produce a periodic modulation of the surface profile. In LIPSS, patterns are produced with periodicity in the directions perpendicular or parallel to the polarization of the incident illumination, and the characteristic period lengths are fractions of, and scale with, the excitation wavelength [20, 26–28]. Analogous behavior has also been demonstrated for the laser-induced photodeposition of metals from organometallic precursors on metal and dielectric substrates [24, 29–31].

Light-directed growth of photoresponsive materials, independent of the optical properties of the growth substrate, could, in turn, enable the design of complex 3D mesostructures such as self-assembled photonic structures [32–34], 3D electrode architectures [35–38], chiral and negative index metamaterials [39–41], as well as optoelectronic devices that exhibit wavelength-and-polarization-selective photoconductivity [42, 43]. Such processes require dynamic feedback between the illumination conditions and the morphology that develops in response to the optical excitation, and also require a method to control the instantaneous light intensity profile at the growth front of the photoresponsive material. One such example is the plasmon-mediated shape control of silver colloids, which have been observed to transform into larger, triangular nanoprisms when the colloidal particles are irradiated with visible light [44–46]. The transformation process has been attributed to the excitation of surface plasmon resonances in the metal nanostructures, such that the particles grow until the frequency of the plasmon resonance matches that of the incident illumination. Moreover, this method enables the size-selective generation of prisms, plates, rods, and cubes as well as other structures, and allows the shape of the structures to be tuned via control of the illumination wavelength [15].

Electrodeposition has been used in commercial processes since the late 1800's for depositing large area metal films and corrosion resistant coatings (anodization) also due to its low cost, high throughput, and scalability. More recently, a significant amount work was carried out to electrodeposit semiconductor films for solar energy applications beginning in the 1970's [47, 48]. Group IV elemental semi-

conductors typically require ionic-liquid or high-temperature molten salt deposition baths. However, semiconductors with increased ionic bonding such as III-IV and in particular II-VI binary semiconductors can be deposited from aqueous solutions [47]. One notable achievement was the production of CdTe based solar cells with an efficiency of >10% in the late 1980's [49]. However, certain challenges have prevented electrodeposited semiconductors from being widely adopted in to technologies such as process reproducibility and poor material quality relative to that of vacuum-deposition processes.

In the following chapters, we detail a maskless, bottom-up patterning technique based on photoelectrodeposition. We observe morphologies similar to LIPSS from the electrodeposition of Se-Te alloys under unstructured illumination. Specifically, template-free photoelectrochemical growth of Se-Te films using linearly polarized illumination spontaneously produces deposits that display highly anisotropic, ordered morphologies. As with LIPSS, the direction of the anisotropy is set by the polarization vector, and the magnitude of the periodicity is a fraction of the illumination wavelength [50, 51]. However, structured Se-Te deposits are produced with mW cm^{-2} intensities, whereas LIPSS formation typically requires intensities on the scale of kW cm^{-2} or MW cm^{-2}. Generation of LIPSS also requires the use of a highly coherent illumination source, whereas the formation of patterns via the photoelectrochemical process proceeds even with highly incoherent light sources. Additionally, in LIPSS, surface material is ablated or rearranged, whereas the formation of patterns via the photoelectrochemical process occur through selective deposition.

1.2 Background: Semiconductor Photoelectrochemistry

When two conductive materials are electrically contacted, charge is transferred across the interface until the electrochemical potentials of the two materials have equilibrated. For a semiconductor/liquid junction, these potentials are referred to as the Fermi level (E_f), and redox potential $E(A/A^-)$ for the two sides of the junction respectively. The distribution of charge in the semiconductor forms an accumulation, depletion or inversion region which refer to the majority carrier (electrons or holes) concentrations being either increased, decreased, or strongly decreased such that the dominant carrier type switches. Sze and Ng's book [52] provides a thorough reference for semiconductor physics topics.

For a reductive photoelectrochemical process, electrons in the semiconductor need

to be transported to the semiconductor/liquid junction interface. This is typically facilitated by an electric field oriented away from the junction and towards the semiconductor domain. A band diagram depicts this as a downward-bending of the bands for positions approaching the interface. The band-bending region can range in length from tens of nanometers to many microns based on the doping of the semiconductor and is referred to as a depletion or inversion in a p-type semiconductor or accumulation in an n-type semiconductor. In addition to the relative values of (E_f) and $E(A/A^-)$, the the band bending can also be modulated by applying a voltage between the semiconductor and solution. However, band bending at the interface is often effected by trapped charges at the interface (Fermi level pinning). An idealized depiction of band bending in the semiconductor for a p-type semiconductor in depletion near the interface is shown in Figure 1.1

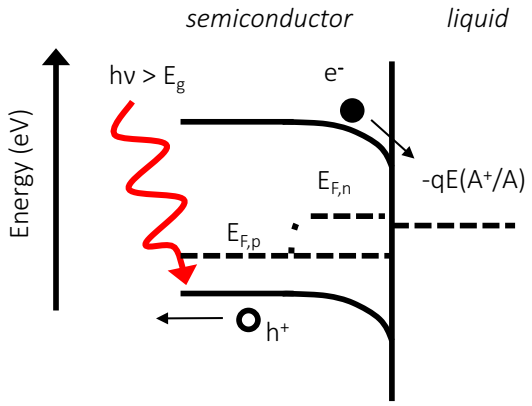

Figure 1.1: Idealized band diagram during photoelectrochemical deposition.

When a semiconductor/liquid junction is illuminated, photogenerated electrons in the semiconductor can be swept by the electric field to the junction to participate in an electrochemical reaction. The increase in hole and electron concentrations is described by the hole and electron quasi-Fermi levels ($E_{f,n}$ and $E_{f,p}$ respectively). Typically it is assumed that electrons generated within the band bending (and less than one diffusion length away) are collected at the interface (see Walter et. al. for a review article on the topic [53]).

At equilibrium, the charge in the band-bending region is balanced in solution by oppositely charged ionic species. This arrangement of charged ionic species in solution is referred to as the electrical double layer (EDL). The charge distribution in the EDL has been modeled as a parallel plate capacitor arrangement (Helmholtz), an exponentially decaying distribution (Gouy-Chapman), or a combination of both of

them (Stern) which has been modified to take into account ion adsorption (Ghram), and the orientation of solvent molecules near the interface due to the electric field (Bockris/Devanthan/Müller, BMD). The double layer is typically much smaller than the band-bending region in the semiconductor and has been modeled as a Schottkey junction in device physics simulations. Introductory textbooks on the structure of the double layer and electrochemistry have been written by Bard [54] and Bockris [55].

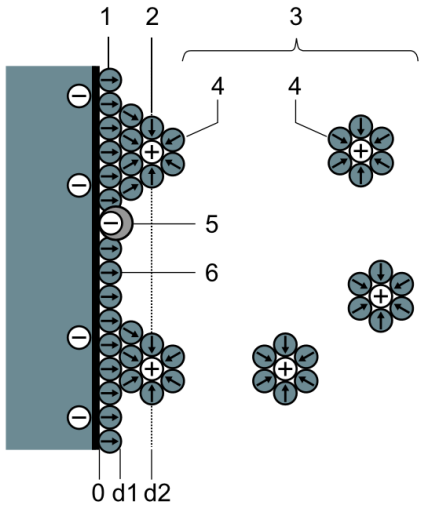

Figure 1.2: Schematic representation of a double layer on an electrode (BMD) model. 1. Inner Helmholtz plane, (IHP), 2. Outer Helmholtz plane (OHP), 3. Diffuse layer, 4. Solvated ions (cations) 5. Specifically adsorbed ions, 6. Molecules of the electrolyte solvent. Figure reproduced from en.wikipedia.org/wiki/Double_layer_(surface_science).

A deposition process is an electrochemical process in which the electrochemical reaction produces a solid reaction product. To begin this process an the ionic species is guided under the influence of the electric potential gradient (drift), concentration gradient (diffusion), and solution flow (convection) if the solution is being stirred. Electrons then discharge across the interface when the ionic species approaches 1-100 nm from the interface. The necessary molecular rearrangements occur to incorporate the adatoms onto the substrate. These adatoms undergo a process of nucleation and growth to build the deposit which can involve surface diffusion of atoms along the interface. For a complete introduction to semiconductor electrodeposition, the author suggests perusal of Pandy's *Handbook of Semiconductor Electrodeposition* [56].

The electric current through an electrode for a given redox species is typically

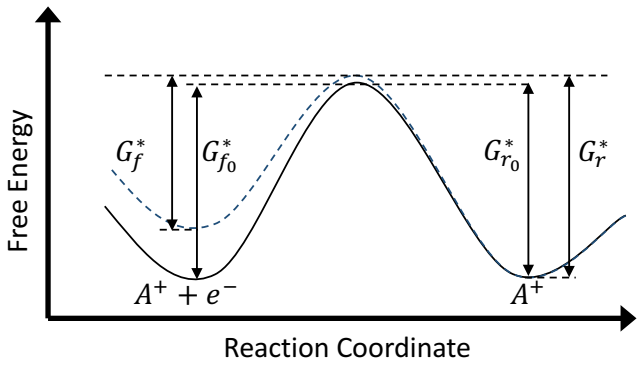

Figure 1.3: Effect of applied potential to forward and reverse activation energies for a one-electron reduction reaction.G_{f0}^* & G_{r0}^* are the forward and reverse activation energies at equilibrium and G_f^* & G_r^* are the activation energies with a negative bias.

modeled through the Butler-Volmer theory. This formalism assumes, from transition state theory, that the forward and reverse rates of a reaction take Arrhenius' form with an activation energy, which is the difference between the reactant or product's free energy and the intermediate transition state's free energy as depicted in 1.3. The activation energies can be decomposed into the activation energy at zero applied potential (typically hidden in the exchange current density) and the changes in forward and reverse activation energies due to the applied field. For a single redox couple, the Butler-Volmer equation can be written as:

$$j = j_0 \left(\exp \frac{\alpha_a z F \eta}{RT} - exp \frac{\alpha_c z F \eta}{RT} \right), \tag{1.1}$$

where in SI units j_0 is the exchange current density (A m^{-1}), which has an exponential dependence on equilibrium activation energy, z is the number of electrons involved in the reaction, F is the Faraday constant (C $mole^{-1}$), R is the molar gas constant (J mol^{-1} K^{-1}), T is the temperature (K), α_a and α_c are the dimensionless charge transfer coefficients for the anodic and cathodic reactions, respectively, which take into account that the applied potential may only shift the forward and backward activation energies some fraction of the applied potential, as depicted in Figure 1.3.

Chapter 2

SPONTANEOUS PATTERN FORMATION UNDER A SINGLE ILLUMINATION SOURCE

In this chapter we describe the formation of nanoscale patterns in Se–Te alloys that are deposited electrochemically in the presence of illumination. Additionally, several models are detailed which provide an understanding for the origin and dynamics of pattern formation. Aqueous solution-phase electrodeposition provided a convenient method to deposit the material and to simultaneously illuminate the growth surface.

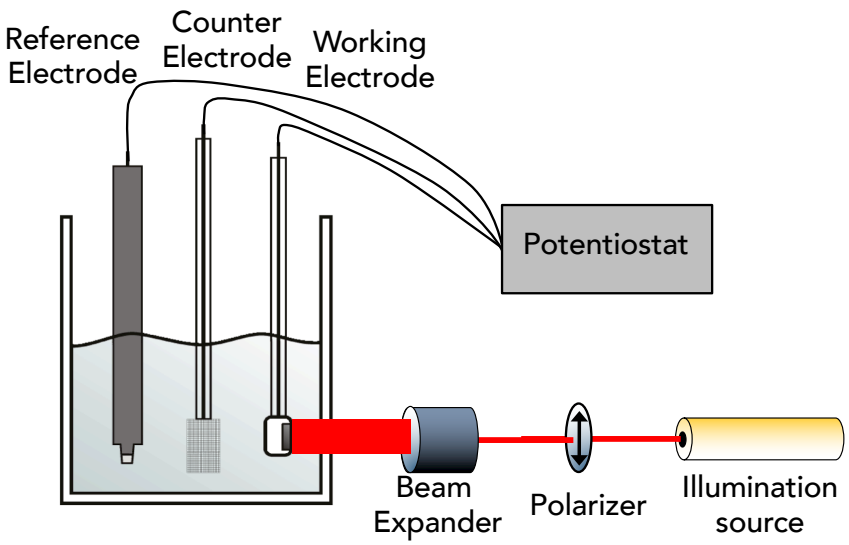

Figure 2.1: Photoelectrodeposition setup.

Figure 2.1 depicts a three-electrode deposition configuration that was used to deposit films of Se-Te. This configuration enabled the absolute potential of the working electrode to be biased with respect to the solution potential. In the photoelectrochemical growth experiments described in this chapter, the illumination conditions were varied during growth to investigate the dependence of the film morphology on the intensity, wavelength, polarization, and incident angle of the illumination. A growth model was developed which suggested that pattern formation correlated to the local absorption profile along the deposit/solution interface.

2.1 Experimental Observation of Pattern Formation

Se–Te films were grown via potential-controlled cathodic electrodeposition from an aqueous solution that contained selenium oxide and tellurium oxide. A non-coherent light source, typically a light-emitting diode (LED), was used to illuminate the working electrode during electrodeposition of the Se–Te films. The LEDs had emission wavelengths ranging from 365 to 940 nm with spectral bandwidths between 7 and 37 nm. The illumination intensity produced by the LEDs was varied between 2.8 and 32.5 mW/cm^2.

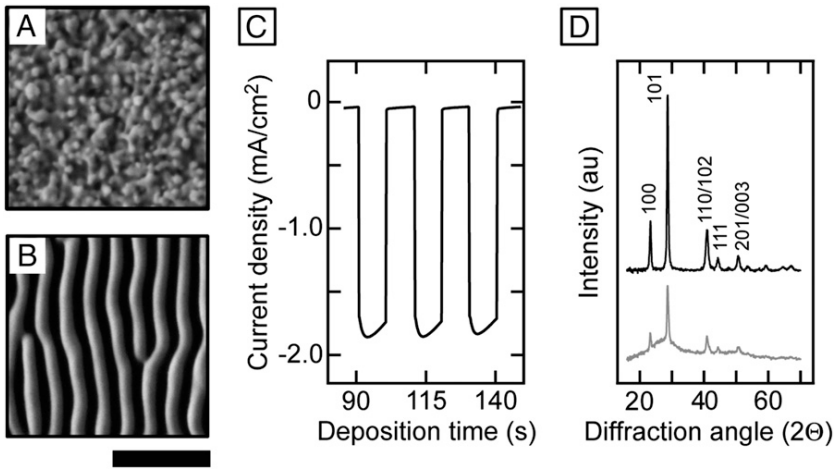

Figure 2.2: Light-directed pattern formation in electrodeposited Se–Te films. (A) Electrodeposited Se–Te film grown in the dark. (B) Electrodeposited Se-Te film grown under linearly polarized, 625-nm illumination from a non-coherent, LED source with an intensity of 16.9 mW/cm^2. [Scale bars: 1 μm (for both A and B).] (C) Deposition current density for growth of a Se–Te film under chopped illumination at E = -0.40 V vs. SCE. The current density increased from an average value of -0.05 mA/cm^2 in the dark to -1.79 mA/cm^2 under an illumination intensity of 18.2 mW/cm^2. (D) X-ray diffraction patterns showing Se–Te films grown in the dark (Top trace) and under illumination (Bottom trace). The (hkl) indices were assigned to diffraction peaks according to ref. [57].

Fig. 2.2 A and B show scanning electron microscope (SEM) images of Se-Te films electrodeposited on degenerately doped, n-type Si(111) substrates at an applied potential (E) = -0.80 V vs. a standard calomel electrode (SCE) until -1.9 C/cm^2 of charge had passed between the counter and working electrodes. The film grown in the dark displayed a granular morphology with no long-range morphological order (Fig. 2.2A). In contrast, the film grown under linearly polarized, 625-nm LED-based illumination with an intensity of 16.9 mW/cm^2 (Fig. 2.2B) exhibited a nanoscale lamellar morphology. The lamellae were oriented parallel to the incident

light polarization direction, exhibited uniform size and period, and were continuous across the entire substrate (typically 1 cm^2 in area). The deposition current density was enhanced under illumination compared with growth in the dark. Fig. 2.2C shows the current density measured during electrodeposition at E = -0.40 V vs. SCE under chopped illumination. At an intensity of 18.2 mW/cm^2 for 625-nm light, the current density showed a 36-fold enhancement compared with that observed during film deposition in the dark. Similar lamellar patterns were obtained using other illumination sources, including a halogen light bulb as well as a low-intensity He–Ne laser (Section 2.8, Fig. 2.10).

Energy-dispersive spectroscopy (EDS) indicated that the films shown in Fig. 2.2 A and B possessed similar compositions of selenium and tellurium. The Se:Te atomic ratio was 58:42 for the film in Fig. 2.2A and 57:43 for the film in Fig. 2.2B. Films that were grown at different applied potentials, on various growth substrates, and under different illumination conditions exhibited Se:Te compositional ratios that ranged from 47:53 to 65:35 (Section 2.8, Fig. 2.11 and Table 2.2). X-ray photoelectron spectra (XPS) recorded at various depths through the films showed that the films consisted of elemental Se and Te. The addition of $CdSO_4$ to the deposition solution improved both film adhesion and the uniformity of the films. XPS depth profiling detected the presence of Cd only at the interface between the Si growth substrate and the Se–Te film (Section 2.8, Figs. 2.12 and 2.16). X-ray diffraction (XRD) patterns further indicated that films grown in the dark and under illumination were both composed of a Se–Te alloy with nanocrystalline domains. The diffraction peaks in the patterns were at angles intermediate between that of pure, elemental Se and pure, elemental Te, both with a hexagonal crystal structure, similar to colloidally synthesized Se–Te alloy nanocrystals (Fig. 2.2) [57]. Debye–Scherrer analysis of the widths of the diffraction peaks was consistent with a crystallite size on the order of tens of nanometers. The film grown under illumination possessed an additional amorphous background. Photo-vitrification has previously been observed in other chalcogenide compounds such as As–Se and As–S [58, 59]. Thus, illumination during electrodeposition of the Se–Te film substantially altered the nanoscale morphology, but produced nearly the same atomic-scale composition and structure as films grown in a dark ambient.

Fig. 2.3 illustrates how the growth of the lamellar patterns depended on the incident light intensity, deposition time, and applied potential. Cross-sectional SEM images of Se–Te films electrodeposited for 500 s at E = -0.40 V vs. SCE, under linearly

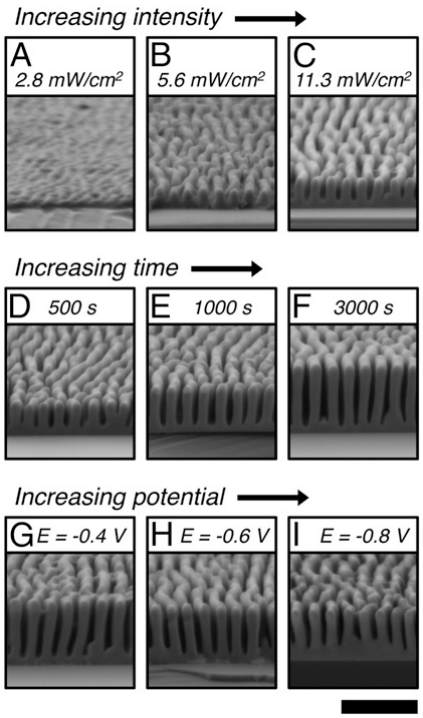

Figure 2.3: Effect of light intensity, deposition time, and applied potential on the growth of Se–Te lamellar films. All films were grown under linearly polarized, 625-nm illumination from an LED source. (A–C) Films grown for 500 s at E = -0.40 V vs. SCE with light intensities of (A) 2.8 mW/cm^2, (B) 5.6 mW/cm^2, and (C) 11.3 mW/cm^2. (D–F) Films grown at E = -0.40 V vs. SCE and with a light intensity between 18.6 and 18.9 mW/cm^2 for deposition times of (D) 500 s, (E) 1,000 s, and (F) 3,000 s. (G–I) Films grown with a light intensity between 18.6 and 18.8 mW/cm^2 until -1.3 C/cm^2 of charge had passed at (G) E = -0.40 V, (H) E = -0.60 V, and (I) E = -0.80 V vs. SCE. [Scale bar: 1 μm (applies to all images).]

polarized, 625-nm light at intensities of 2.8, 5.6, and 11.3 mW/cm^2, respectively, indicated that increasing the light intensity increased the growth rate (i.e., total amount of material deposited) and increased the height anisotropy (i.e., the peak-to-trough height) of the lamellar features (Fig. 2.3 A–C). Under constant illumination conditions, the lamellae also grew taller with increasing deposition time (Fig. 2.3 D–F). For example, at E = -0.40 V vs. SCE under linearly polarized, 625-nm illumination with an intensity between 18.6 and 18.9 mW/cm^2, the average height of the lamellae at their peaks was 460 ± 28 nm (average ± first SD from 50 measurements) for a film grown for 500 s and was 938 ± 18 nm for a film grown for 3,000 s. At a fixed applied potential during electrochemical deposition, the dark contribution to film growth decreased with time due to the increasing resistance of the Se–Te film. Thus, the deposition current and resulting change in lamellae height slowly decreased with

time (Section 2.8, Fig. 2.13). In contrast, the film thickness of the troughs between lamella remained approximately the same at 122 ± 23 nm for the film grown for 500 s and 116 ± 25 nm for the film grown for 3,000 s. The width of the lamella also remained nearly constant, at 143 ± 10 nm for the film grown for 500 s and 164 ± 9 nm for the film grown for 3,000 s.

The relative contributions to the total deposition current density that were produced by the photocurrent and the dark current could be adjusted by changing the light intensity and the applied potential, respectively. Fig. 2.3 G–I show lamellar films for which the light intensity and total amount of charge passed were held constant, but with values of E = -0.40, -0.60, and -0.80 V vs. SCE, respectively. At a light intensity of 18.6 mW/cm^2 and E = -0.40 V vs. SCE, the enhancement ratio of the photocurrent to the dark current ratio was 36, whereas under the same light intensity, this ratio decreased to 5 at E = -0.80 V vs. SCE (Section 2.8, Fig. 2.14 and Table 2.3). Fig. 2.3 G–I show that, as the applied potential was made more negative, the lamellar height decreased and the amount of growth at the bottom of the troughs increased. Although more negative potentials and higher light intensities both enhanced the average current density, the dark-current contribution led to non-selective film growth, whereas the photocurrent contribution promoted anisotropic growth of the lamellar features.

Variations in the polarization, wavelength, and angle of the incident illumination altered the pattern that developed during light-directed growth of the Se–Te films. Fig. 2.4 A–E shows the effect of polarization on film growth. Under randomly polarized light, the lamellae did not display orientational order (2.4A). However, under linearly polarized illumination, the lamellae grew to be aligned parallel to the electric-field vector of the incident illumination, with the growth pattern evident across the entire substrate (2.4 B and C). When the polarization was changed, further growth of the lamellae occurred with an orientation toward the new direction of the electric field. Woodpile-like nanostructures were therefore created through 90° shifts in the polarization, and spiral structures were produced through continuous rotation of the polarization (2.4 D and E). The period of the lamellae varied from a value of 130 ± 4 nm (average ± first SD from 25 measurements) for UV (365 nm) illumination to 412 ± 19 nm for near-infrared (940 nm) light (Figs. 2.4 F–I and 2.5). A change in the illumination wavelength from 940 to 455 nm during growth induced branching in the lamellae in response to the change in lamellar period (2.4J). Thus, complex nanoscale structures in 3D can be produced in a continuous, designed

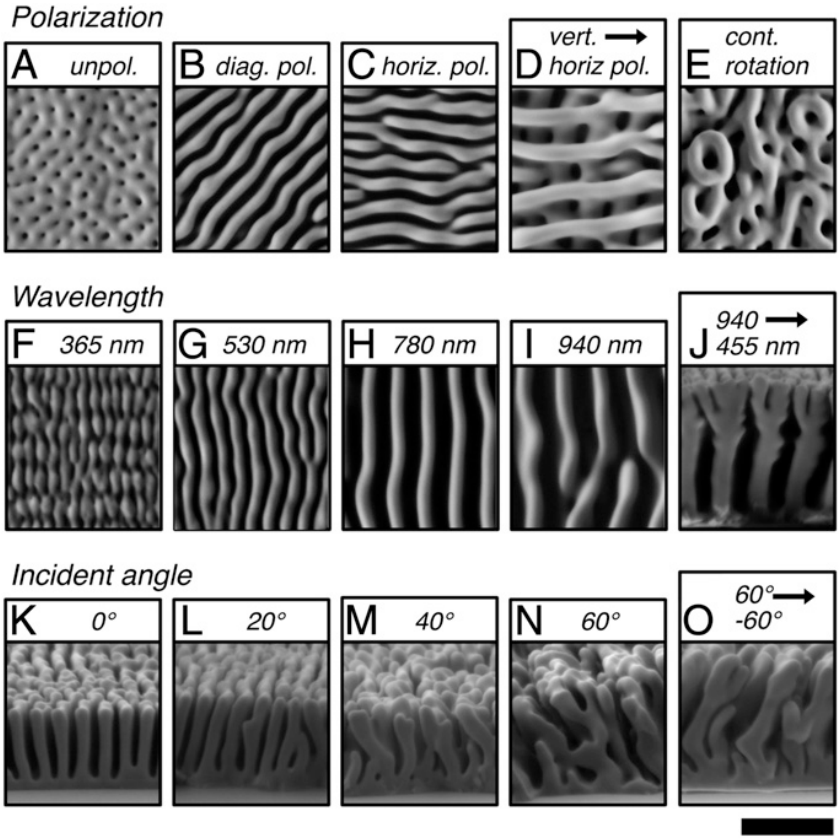

Figure 2.4: Effect of polarization, wavelength, and angle of the incident light on the growth of Se–Te lamellar films. (A–E) Polarization dependence under normally-incident illumination. Films grown under (A) randomly polarized, 625-nm illumination, (B) linearly polarized, 625-nm illumination with the electric field of the incident light oriented at a 45° angle to vertical, (C) same as B, but with the electric field of the incident light oriented horizontally, (D) growth under 940-nm illumination with the polarizer oriented vertically for 300 s and then horizontally for 300 s, and (E) growth under 940-nm illumination with continuous rotation of the polarization in 5° increments for a total rotation of 550°. (F–J) Wavelength dependence for normally-incident, linearly polarized light. Films grown under illumination wavelengths of (F) 365 nm, (G) 530 nm, (H) 780 nm, (I) 940 nm, and (J) 940 nm until -1.5 C/cm^2 charge had passed, followed by 455 nm until -1.5 C/cm^2 charge had passed. (K–O) Dependence on the incident angle for linearly polarized, 625-nm illumination. Films grown under illumination at an angle of (K) 0° from normal, (L) 20° from normal, (M) 40° from normal, (N) 60° from normal, and (O) +60° from normal until -0.9 C/cm^2 of charge had passed, followed by an angle of -60° from normal until -1.1 C/cm^2 of charge had passed. [Scale bar: 1 μm (applies to all images).]

process based on the dynamic response of the evolving film morphology to changes in the incident wavelength and polarization direction.

The growth direction of the lamellae changed with the angle of the incident light (2.4 K–O). For example, the lamellae grew normal to the substrate under normally incident illumination (Figs. 2.3 D–F and 2.4K), whereas at an angle of 20° from normal, the lamellae appeared to tilt slightly away from the direction of the incident light. However, at more oblique angles of 40° and 60° from normal, respectively, the lamellae grew toward the illumination source. When the angle of illumination was changed from 60° to -60° during growth, some of the lamellae (54% of 200 counted) reoriented to grow toward the new direction of the incident light forming zigzag structures. However, the growth of some lamellae (46%) was stunted, consistent with the shadowing of these lamellae by their neighbors, which inhibited their growth when the incident angle was reversed. Because the growth rate of the Se–Te nanostructures was enhanced under higher illumination intensities, and because the lamellae grew toward the source of illumination, the growth of the inorganic structures can therefore be designated as phototropic, by analogy to the similar phenomenon exhibited by living plants.

The lamellar patterns produced during photoelectrodeposition of the Se–Te alloy qualitatively resemble the ripple patterns formed during LIPSS of metal and dielectric surfaces. Ripple patterns have been observed during laser-induced damage and melting of sodium chloride, silicon, germanium, gallium arsenide, aluminum, brass, as well as other dielectrics and metals [17, 19, 21, 22, 60, 61], etching of platinum in a chlorine atmosphere [23], and photolytic decomposition of organometallic cadmium, zinc, aluminum, and copper precursors onto silicon [24, 25]. Both processes involve the light-induced formation of a periodic profile on an initially flat surface, but LIPSS and phototropic growth of the Se–Te lamellar patterns arise from fundamentally different phenomena. Experimentally observable differences include the fact that the typical light intensities used for LIPSS are much higher than those used for phototropic growth of the Se–Te films (i.e., between 10 W/cm^2 and 10 MW/cm^2 for continuous laser irradiation during LIPSS, whereas the illumination intensities used in this work were less than 50 mW/cm^2). LIPSS therefore requires laser irradiation to achieve the necessary intensity, whereas we have demonstrated the formation of lamellar patterns via phototropic growth using a variety of different illumination sources, including LEDs, a halogen light bulb, as well as a low-intensity laser. The ripple patterns formed during LIPSS under normally incident laser irradiation typically run perpendicular to the electric field of the incident laser irradiation with a period of λ/n, where λ is the illumination wavelength and n is the refractive index of the medium above the surface of the substrate. In contrast, phototropic

growth produced lamellar patterns that were parallel to the incident electric field with a period of $\lambda/2n$ at short illumination wavelengths (i.e., <600 nm) but exhibited longer periods at longer wavelengths (Fig. 2.5). Additionally, phototropic growth is capable of producing structures that cannot be produced by LIPSS, such as dynamically directed growth toward the incident light beam as well as stacked woodpile structures in layers that are optically and physically weakly coupled, or largely uncoupled, from the growth substrate (Fig. 2.4). (In LIPSS, variations in the angle of the incident laser irradiation only affect the period and orientation of the ripple patterns.) Fundamentally, phototropic growth differs from LIPSS in that the phototropic growth is a property of the growing Se–Te film under noncoherent, low-intensity illumination, as opposed to relying on and exploiting specific optoelectronic properties, using a high-powered laser, of the substrate. Thus, the formation of the initial periodic pattern during phototropic growth, the dependence of the lamellar period and orientation on the wavelength and polarization of the incident illumination, as well as dynamic feedback between the illumination conditions and the evolving nanoscale structure require further examination.

2.2 Origin of pattern formation

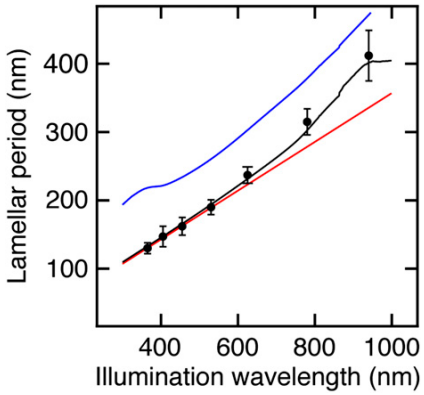

Figure 2.5: Comparison of the experimentally observed wavelength dependence of the lamellar period with simulated periods produced by different scattering models. The black circles are the experimentally observed values of the period for lamellae grown under different illumination wavelengths. Each circle represents the average of 25 measurements and the error bars represent 2 SDs in the average value. The red trace is the simulated interference period due to dipole scattering at the surface of a flat Se–Te film. The blue trace is the simulated period due to Bloch mode scattering from a periodically structured Se–Te surface. The black trace is the simulated period combining both scattering modes where the contributions from the surface and Bloch modes are weighted based on the penetration depth of the incident light.

To more fully understand the onset of phototropic pattern formation in the Se–Te material, an optical response model was constructed for a flat Se–Te film with scattering centers at its surface. Full-wave finite-difference time-domain (FDTD) simulations were performed on a 100-nm-thick Se–Te film sandwiched between a Si substrate and a medium with a refractive index of n = 1.4 (i.e., similar to that of the aqueous sulfuric acid solution used in the electrodeposition). The complex dielectric function of the Se–Te material used in the simulations was obtained by fitting spectroscopic ellipsometry data measured for a 170-nm-thick film grown in the dark (Fig. 2.6). In the full-wave electromagnetic simulations, dipole radiation sources were used to simulate localized scattering of incident illumination at the surface of a Se–Te film arising from either surface roughness or electronic defects [17, 22]. Interference of the scattered light from different points on the surface produced a sinusoidal modulation of the optical intensity at the film surface with a period of λ/2n. (In this model, the intensity pattern was generated by interference between multiple scattering centers, whereas in LIPSS the intensity pattern is due to interference between the incident laser irradiation and surface scattered waves arising from the specific optoelectronic properties of the substrate.) Assuming the growth profile of the Se–Te film is proportional to the intensity of the interference pattern, this scattering model for a flat Se–Te surface produced a simulated period that matched well with the experimentally observed lamellar periods for short illumination wavelengths (Fig. 2.5). At illumination wavelengths above 600 nm, in which the incident light penetrated more deeply into the Se–Te film, the experimental period deviated to longer values from the periods produced by this dipole scattering model. The addition of a Bloch mode component to the intensity profile arising from the periodically curved Se–Te lamellar surface produced good agreement between the experimental and simulated periods across the entire experimental wavelength range. These results suggest that, although a sinusoidal variation in the surface absorption profile may produce a periodic modulation in the local growth rate of the initially unstructured film, feedback between the evolving nanophotonic structure with the incident radiation guides the growth of the final morphology.

The interference pattern generated by two aligned dipoles on the surface of a flat Se–Te film sandwiched between a Si substrate and a 1.4 index solution was simulated using full-wave finite-difference time-domain (FDTD) simulations. All FDTD simulations were performed using the Lumerical Solutions, Inc. FDTD software package. In the simulations the 100 nm thick Se–Te film was modeled using the n and k data obtained from spectroscopic ellipsometry in the range of 300 to 1000 nm

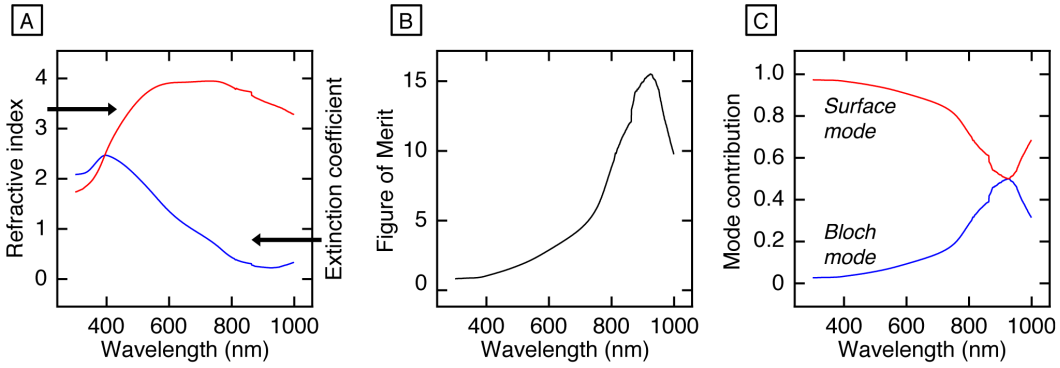

Figure 2.6: Optical modeling used to simulate the lamellar period as a function of illumination wavelength. (A) Refractive index, n, and extinction coefficient, k, for the Se–Te alloy modeled from spectroscopic ellipsometry measurements. The discontinuity in the spectra at 850 nm is due to the change in illumination source. (B) Photonic figure of merit, fom = n/k, used to model the contribution of the surface and Bloch modes to the scattered intensity profile. (C) The relative contributions for the surface and Bloch modes, which were assumed to be equal when the fom was at a maximum.

and the electrodeposition solution was modeled as a uniform 1.4 index environment. The dipoles were placed 2 μm apart, and oriented either parallel or perpendicular to the line of separation to simulate their excitation with plane-waves polarized along these directions.

To obtain the interference pattern generated between the dipoles, the dipoles were excited in phase with a broadband pulse, and the steady state coherent superposition of the fields was obtained by Fourier transforming the field response at the Se–Te/solution interface and normalizing it by the Fourier transform of the source. The resulting steady state field profile generated along the line connecting the two dipoles was then fitted with a sinusoid to obtain the peak-to-peak periodicity of the standing wave pattern. The resulting period of the standing wave intensity pattern at the surface of the Se–Te film, p_{surf}, is given by:

$$p_{surf} = \frac{\lambda_0}{2n_{surf}} \tag{2.1}$$

In equation 2.1, λ_0 is the free space illumination wavelength and n_{surf} is the effective index at the surface of the Se–Te film. The effective index was found to be slightly larger than the 1.4 index of the solution, consistent with radiation modes supported at the Se–Te/solution interface that are oscillatory in the 1.4 index solution environment and decay exponentially into the higher index of the absorbing Se–Te material.

Although both dipole orientations generate the same period in the resulting field profile, the interference pattern is more pronounced for the parallel-aligned dipoles as there is a higher density of states for the modes supported along this direction based on the complex dielectric function of the Se–Te material. We note that in this model the physical separation of the dipoles only affects the overall position, but not the actual peak-to-peak period of the interference pattern, as the distance between dipoles only adds an overall phase shift to the interference pattern.

Assuming the growth profile of the Se–Te film is proportional to the intensity of the interference pattern, the model for scattering off the surface of a flat Se–Te film matches the experimentally observed lamellar periods at short illumination wavelengths (see Fig. 2.5). However, at longer wavelengths (i.e. > 600 nm) the experimental period deviates towards longer values compared to those simulated by the surface scattering model. The addition of a Bloch mode component to the field profile that is supported by the evolving periodic lamellar structure produced good agreement between the experimental and simulated periods over the entire wavelength range used to grow the Se–Te films (365 to 940 nm). The relative contributions of the Bloch mode and surface mode to the period were modeled based on the wavelength-dependent penetration depth of the incident light into the Se–Te material.

To understand the contribution from the Bloch scattering mode to the lamellar period, full-wave FDTD simulations were used to visualize the intensity distribution of lamellar structures with various defined periods as a function of illumination wavelength. The intensity distributions for lamellar structures with a 900 nm height, a 205 nm width, and a 410 nm period under plane-wave illumination with wavelengths of 780, 940, and 1200 nm are plotted in Fig. 2.7. We identify the resonant wavelength of the structure as being 940 nm since this wavelength generates a field intensity maximum near the top of the lamella structure. At this resonant wavelength there are two intensity peaks per unit cell (one on either side of the lamella structure near the top), so the Bloch wave can be treated as being half in the Se–Te lamellae and half in the surrounding solution. Thus, the periodicity of the Bloch wave intensity pattern, p_{Bloch}, is set to be the average of the effective wavelength in the two materials:

$$p_{bloch} = \frac{1}{2}\left(\lambda_{sete} + \lambda_{soln}\right) = \frac{\lambda_0}{2}\left(\frac{1}{n_{sete}} + \frac{1}{n_{soln}}\right) \tag{2.2}$$

In equation 3, λ_{SeTe}, and n_{SeTe} are the effective wavelength and refractive index, re-

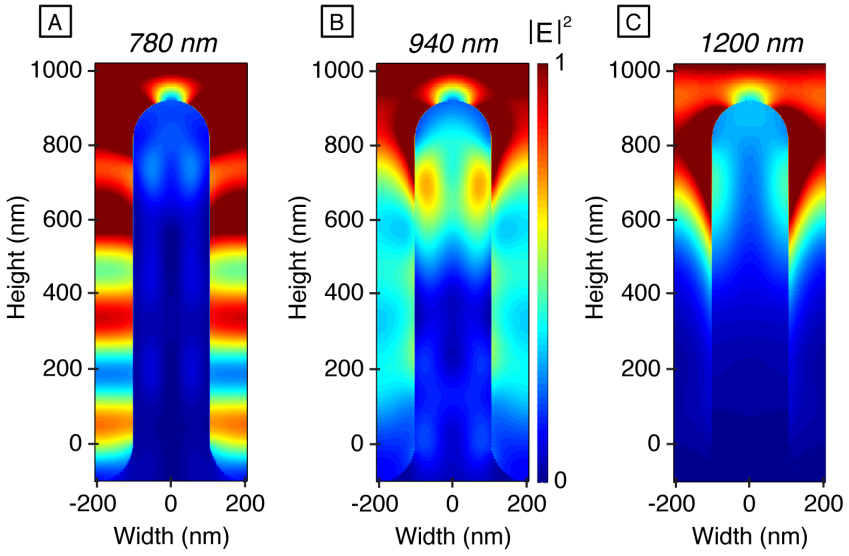

Figure 2.7: FDTD simulations of the intensity profile for periodic Se–Te structures under plane-wave illumination. The lamellar structures were constructed with a 900 nm height, a 205 nm width, and a 410 nm period. The images show one unit cell, and periodic boundary conditions were used for the simulations. The intensity distributions are shown for the structures under plane-wave illumination with wavelengths of (A) 780 nm, (B) 940 nm, and (C) 1200 nm. The intensity scale, $|E|^2$, shown in B applies to all three images.

spectively, within the Se–Te material, and λ_{soln} and n_{soln} are the effective wavelength and refractive index, respectively, in the solution. Because the lamellar structures are illuminated from the top, the incident field scatters into both the Se–Te/solution Bloch mode and the surface mode with an efficiency that is proportional to the photonic figure-of-merit, fom = (n/k) of the Se–Te material. The ratio, n/k, is proportional to the number of field oscillations that occur in the material before decaying to a value of 1/e. Using this figure-of-merit, the system is dominated by the Se–Te/solution surface mode at wavelengths where the Se–Te material has a high loss (i.e. a low fom). Consistent with this model, the period produced by the dipole scattering model closely matches the experimental lamellar period at short illumination wavelengths, where the fom is close to 0 (Fig. 2.5, red trace). However, at longer illumination wavelengths where the value of the fom sharply increases there is an increasing contribution from the Bloch mode to the wave intensity pattern.

The wavelength dependence of the fom is shown in Fig. 2.6 B. Assuming that the incident light scatters into both modes with equal weight when the fom is at a maximum, fom_{max}, within the experimental wavelength range, we set the fractional

weights of the Bloch mode, f_{Bloch}, and surface mode, f_{surf}, to:

$$f_{bloch} = \frac{fom}{2 \cdot fom_{max}} \tag{2.3}$$

$$f_{surf} = (1 - f_{bloch}) \tag{2.4}$$

The wavelength dependence of f_{Bloch} and f_{surf} are shown in Fig. 2.6 C. Using these fractional weights, the effective period of the structure, p_{eff}, is given by the sum of the weighted Bloch and surface wave periodicities,

$$p_{eff} = (f_{bloch} \cdot p_{bloch} + f_{surf} \cdot p_{surf}) \tag{2.5}$$

This modified scattering model is plotted in Fig. 2.5 (black trace) and shows good agreement with the experimental period at both short wavelengths (where the loss is high, so the fom is low, and the scattered field is dominated by the surface mode index) and at long wavelengths (where the loss is low, so the fom is high, and scattering occurs into both the surface and Bloch modes of the periodic structure).

2.3 Monte Carlo – FDTD Growth Model

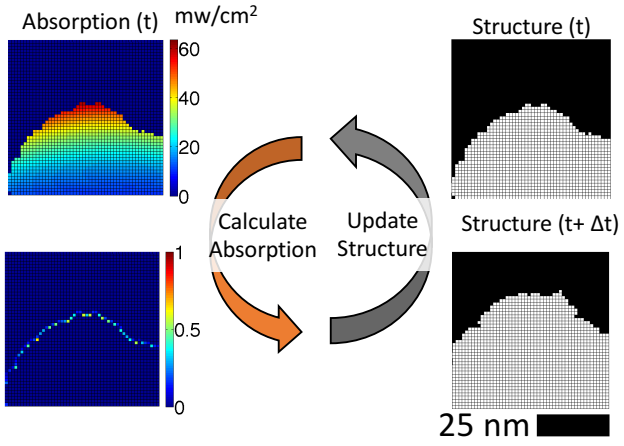

Figure 2.8: Graphic illustrating iterative growth model.

To simulate feedback between the local light intensity and the film growth, an iterative model was used in which the photocarrier generation rate calculated from

electromagnetic simulations controlled the probability for mass addition in Monte Carlo simulations of the evolution of the surface (Fig. 2.8). The only input parameters for these simulations were the complex dielectric functions of the Se–Te film and of the surrounding media, as well as estimates of the charge-carrier concentrations and excited-state lifetimes in the material. During the first Monte Carlo iteration, mass was added to a bare Si substrate immersed in water. The local photocarrier generation rate of this initial Se–Te surface layer was calculated under linearly polarized, plane-wave illumination. Mass was then added iteratively to the surface of the same film, with the Monte Carlo probability of mass addition to the surface taken to be proportional to an Arrhenius type of rate constant. The driving force of the rate constant was explicitly related to the local splitting of the electron and hole quasi-Fermi levels in the Se–Te film based on the local power absorbed within the film, which was recalculated for each iteration in the evolving structure. The growth model produced patterns in which the lamellar stripes were parallel to the polarization direction of incident illumination and exhibited periods under a given illumination wavelength that were remarkably similar to those observed in the experimental structures (Fig. 2.9 A–J). Fig. 2.9 A–F illustrates several stages of growth in the model. During the initial stages of simulated growth, mass was added randomly to the surface, thereby creating a flat Se–Te film with nanoscale surface roughness (Fig. 2.9A). This roughness, in turn, produced local variations in the photogeneration rate across the surface of the film (Fig. 2.9 B and C), which caused subsequent deposition preferentially in regions with enhanced absorption. At later stages of growth, the local absorption maxima became periodically spaced, producing a lamellar pattern similar to the pattern that was observed experimentally (Fig. 2.9 D–F). The period of the simulated structures increased with illumination wavelength and at each simulated wavelength was within 15% of the period observed experimentally (Fig. 2.9 G–I). Furthermore, the evolving morphology in this iterative growth model dynamically responded to the instantaneous illumination conditions. When the wavelength was changed during the simulations, the lamellae branched to adjust to the new period (Fig. 2.9J), also in accord with the experimental observations (Fig. 2.4J).

The two-step growth algorithm was performed on a two-dimensional square mesh starting on a bare silicon substrate. First, the absorbance of the structure under linearly polarized, plane-wave illumination was simulated using FDTD with periodic boundary conditions in the in-plane direction. A planar silicon sheet with a thickness of 3 μm was used for the initial structure. Matlab was used to perform Monte

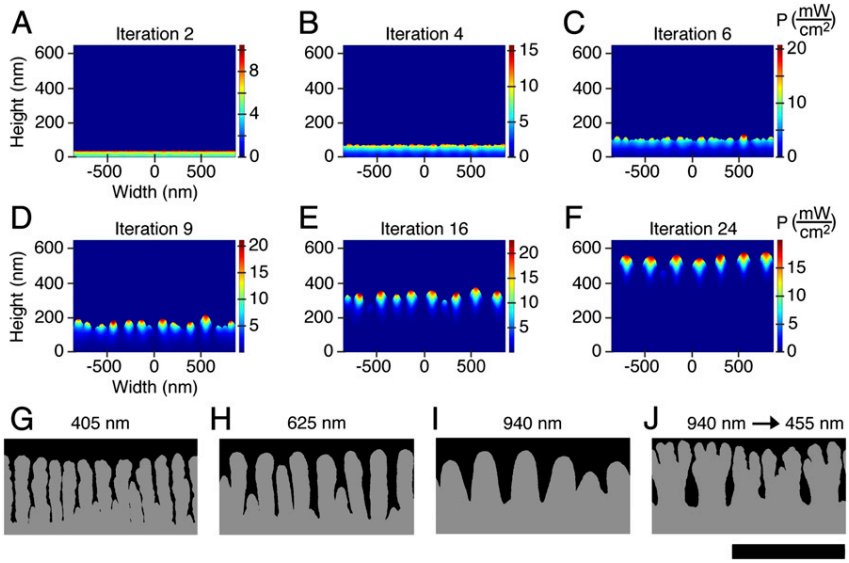

Figure 2.9: Iterative growth model to simulate feedback between the local absorption profile and phototropic growth of the Se–Te films. (A–F) Simulated absorption profiles at different iterations of growth for Se–Te lamellar patterns under 625-nm normally-incident, plane-wave illumination with the electric field vector of the illumination perpendicular to the plane of the page. The images in A–F have been stretched vertically for clarity and have an aspect ratio of 1.8. (G–J) Simulated structures formed under different illumination wavelengths using the iterative growth model. Films grown under linearly polarized, plane-wave illumination at wavelengths of (G) 405 nm, (H) 625 nm, (I) 940 nm, and (J) in which the illumination wavelength was switched from 940 to 455 nm during the growth simulation. [Scale bar: 1 μm (applies to the images in G–J, which have an aspect ratio of 1).]

Carlo simulations where mass was added to the upper surface of the structure with probability, F, based on an Arrhenius constant (Eq. 2.6). The absorbance of the new, structured film was then calculated in the same manner as the initial planar film. The absorbance calculation – mass addition process was iterated until the desired cross section was achieved. An overview of the simulation code and link to a repository can be found in Appendix A of this thesis.

$$F(G) = \left[1 + G\left(n_0\tau_p + p_0\tau_n\right) + G^2\frac{\tau_p\tau_n}{n_i^2}\right]\prod_{i=1}^{3}\frac{x_i}{r_i} \tag{2.6}$$

In Eq. 2.6, G is the absorbed power normalized by the photon energy, hν, n_i is the intrinsic carrier concentration, n_0 is the electron concentration, p_0 is the hole concentration, τ_n is the electron lifetime, τ_p is the hole lifetime, x_i is the fraction of i$^{\text{th}}$ nearest neighbors occupied in the square lattice, and r_i is the distance to the

i^{th} nearest neighbor. The model assumes Arrhenius kinetics for reductive electron transfer leading to mass addition with the driving force equal to the splitting of the quasi Fermi levels. However, it should be noted that the second term in brackets was originally intended to be multiplied by a factor of $1/n_i^2$ (see Eq. 2.10). This factor was omitted due to an error in the simulation code, which effectively linearized the dependence of F(G) on G. The success of Eq. 2.6 in reproducing the experimental morphologies could be due to an over estimation of the carrier lifetimes which would have minimized the effect of the G^2 term thus making Eq. 2.6 effectively linear in G. The multiplicative sum reduces the surface roughness of the film so as to mimic the experimentally observed surface roughness.

For these simulations, the Se–Te films were assumed to be undoped (i.e. $n_0 = p_0 = n_i$) and a value of $n_i = 10^{10}$ cm^{-3} was used for the intrinsic carrier concentration based on previous electrical measurements of Se–Te alloy films [62]. A value of 1 μs was used for both the electron and hole carrier lifetimes [63]. A two-dimensional square mesh with a lattice constant of 1 nm was used for the simulations. A power flux of 16.5 mW/cm^2 was used for the plane-wave illumination source with the electric field perpendicular to the square mesh.

2.4 Derivation of Mass Addition Distribution function

The current flux at the interface was assumed to follow a Butler-Volmer one-step, irreversible relationship:

$$j \propto \exp\left(-\frac{\eta}{k_b T}\right), \tag{2.7}$$

where k_b is the molar gas constant (eV K^{-1}), T is the temperature (K). The over-potential η is assumed to be equal to the photo-voltage produced in the semiconductor material as a result of light absorption. This value was taken to be equal to the quasi-fermi level splitting:

$$\eta = E_{f,p} - E_{f,n} = -k_b T \log\left(\frac{np}{n_i^2}\right), \tag{2.8}$$

Plugging 2.8 into 2.7 we get:

$$j \propto \frac{np}{n_i^2} = \frac{(n_0 + \Delta n)(p_0 + \Delta p)}{n_i^2} = \frac{n_0 p_0 + n_0 \Delta p + p_0 \Delta n + \Delta p \Delta n}{n_i^2} \tag{2.9}$$

Where the carrier concentrations have been expanded to their equilibrium values (n_0, p_0) plus deviation due to generation due to light absorption (Δ_n, Δ_p). Assuming low-level injection ($\Delta p << p_0$ for a p-type semiconductor) and no carrier transport due to drift or diffusion, the current flux can be written as:

$$j \propto 1 + \frac{G\left(n_0\tau_p + p_0\tau_n\right) + G^2\tau_p\tau_n}{n_i^2} \tag{2.10}$$

where G is the generation rate due to absorption of photons, and τ_p and τ_n are the hole and electron lifetimes in the deposit. And we've used the assumption for non-degenerately doped semiconductors that $n_0 p_0 = n_i^2$. However, due to an error in the simulation code, a modified equation was used (Eq. 2.6).

2.5 Conclusions

We have described an adaptive inorganic system that produces predesigned patterns in 3D space from unstructured matter, i.e., in an isotropic solution on an isotropic substrate, directed in space by the properties of a light beam as it interacts with the growing matter. This demonstration of this phenomenon does not arise from any preexisting pattern or classical interference effect in the substrate, but is an emergent phenomenon that occurs dynamically during film growth in response to the incident illumination conditions. This phenomenon provides the ability to grow structures of entirely different geometries, periods, and directions abruptly on top of one another, and the ability to change the physical growth direction of the material by changing the direction of the incident light beam. A model in which the local optical absorption at the surface of the growing film controlled the probability for mass addition reproduced the experimentally observed nanoscale lamellar patterns and also reproduced their dependence on the wavelength and polarization of the incident illumination. This model required relatively few input parameters as it used only the complex dielectric function of the Se–Te alloy and estimates of the carrier concentration and excited-state carrier lifetimes. Other chalcogenide-based materials possess similar optoelectronic properties to those used as input parameters in the phototropic growth simulations [58, 59, 64–68]. The extension of phototropic growth to these material systems could enable a process for dynamic photolithography in which complex 3D structures are built up through temporal variations in the illumination conditions.

2.6 Film Characterization

Scanning electron microscopy (SEM) was performed using a Zeiss model 1550VP field-emission scanning electron microscope operated at an acceleration voltage of 2 keV. After the growth substrate was detached from the Sn–Cu wire as described above, the substrate was affixed to the SEM sample chuck using copper tape. A below-lens secondary electron detector was used to image the samples. Energy-dispersive spectroscopy (EDS) was performed at an acceleration voltage of 20 keV using either an Oxford INCA 300 or a X-Max SDD X-ray EDS system. The average height, width, and period of the lamellar features were measured from SEM images using Image-J analysis software. To measure the variation in lamellar peak heights and widths as a function of growth time, 50 measurements were taken for each sample. The average value and 1st standard deviation are reported in the text. To measure the variation in lamellar period as a function of illumination wavelength, 25 measurements were taken for each sample. The average value and 2nd standard deviation are shown in Fig. 2.5.

X-ray diffraction (XRD) patterns were obtained using a Bruker D2 Phaser with a Cu radiation source (1.54184 Å) and a Lynxeye line detector. The samples were prepared by scraping the Se–Te films off the Si(111) growth substrate using a tungsten carbide razor blade and transferring the material onto a zero background Si(511) XRD plate. Each sample was scanned from 16°to 80°in 2θ with a step size of 0.06°and an acquisition time of 10 s per step. The samples were rotated at 10 rpm during the measurement. The diffraction peak line widths were analyzed using Diffrac Suite EVA software.

X-ray photoelectron spectroscopy (XPS) depth profiling was performed on a Kratos Axis Ultra system with a base pressure below 1×10^{-9} Torr. An octopole ion gun operating at 3 keV was used to etch through the sample at a rate of 1 nm sec^{-1} in 5 to 10 nm intervals. XPS data were acquired using the 1486.6 eV line from a monochromated Al Kα source at 150 W with a multichannel detector set to a pass energy of 10 eV for the high-resolution scans. Acquisition times were approximately 300 s per step, depending on the energy region being probed.

To model the complex dielectric function of the Se–Te alloy, spectroscopic ellipsometry was used to measure the complex reflectance ratio, ρ, for p- and s-polarized

light given by:

$$\rho = \frac{r_p}{r_s} = \tan(\Psi)\exp^{i\Delta} \tag{2.11}$$

In Eq. 1, Ψ is the amplitude ratio and Δ is the phase difference for p-polarized, r_p, and s-polarized, r_s, light reflected off the surface of the Se–Te film. A Sentech Instruments SE 850 spectroscopic ellipsometer equipped with a Xe lamp as the UV-Vis source (300-849 nm) and a halogen lamp combined with an FT-IR spectrometer as the NIR source (850-2200 nm) was used for the measurements. The Se–Te film was grown in the dark on a n+Si(111) substrate and had a thickness of 170 nm as measured by cross-sectional SEM. The Ψ and Δ spectra were recorded at angles of 50°, 55°, 60°, 65°, and 70°in a polarizer-sample-analyzer configuration. The model to determine the complex dielectric function of the Se–Te alloy consisted of a 170 nm thick isotropic film sandwiched between air and a semi-infinite layer of Si(111). Polynomial fitting of the Ψ and Δ spectra was used to calculate values of the refractive index, n, and extinction coefficient, k, at 1 nm intervals, where the optical constants were made to be continuous over a 50 nm width at each interval.

The n and k spectra are shown in Fig. 2.6A. The electrodeposited Se–Te films exhibit similar n and k spectra to those previously measured for Se–Te alloys grown by thermal evaporation [69]. The first direct band gap transitions occur at approximately 1.85 eV for selenium and at approximately 0.33 eV for tellurium. The band gap values can vary by as much as 0.12 eV depending on whether the material is amorphous or crystalline [70–72]. Alloys of Se and Te have band gap energies between these two values, which vary systematically with the Se:Te ratio [70–72]. For the spectra in Fig. 2.6A the extinction coefficient reaches a minimum value of 0.23 at a wavelength of 925 nm (1.3 eV). Structural disorder induced by the addition of Te to Se produces significant tailing of the band edges as well as the formation of localized states within the band gap, which may explain why the extinction coefficient does not go all the way down to zero and begins to increase at longer wavelengths [71, 72].

2.7 Experimental Methods

Materials. All materials were used as received without further purification. Gallium powder (Ga, 99.999% metals basis), cadmium sulfate 8/3-hydrate ($CdSO_4$•2.67 H_2O, ≥ 99+%), zinc sulfate monohydrate ($ZnSO_4$•1 H_2O, ≥ 99+%), tellurium (IV) oxide (TeO_2, 99+%), and platinum gauze (Pt, 100 mesh, 99.9% metals basis) were purchased from Sigma-Aldrich. Indium shot (In, 99.999% metals basis),

selenium (IV) oxide (SeO_2, 99.4% metals basis), and Pt wire (0.5 mm diameter, 99.997% metals basis) were purchased from Alfa Aesar. Acetone (99.9%, ACS grade) and concentrated hydrochloric acid (HCl, ACS grade) were purchased from VWR. Buffered fluoride-bifluoride hydrofluoric acid was purchased from Transene (Buffer HF Improved). High purity, conductive silver (Ag) paint was purchased from Structure Probe Inc. (SPI) supplies. Double-coated conductive carbon and copper tape were purchased from Ted Pella. Loctite Hysol 9460 epoxy adhesive was purchased from McMaster Carr.

Electrode preparation. Single crystal, n-type silicon wafers with the (111) orientation and doped with arsenic were purchased from Addison Engineering Inc. The wafers had a diameter of 125 mm, a thickness of 400 ± 15 μm, and an average resistivity between 0.004 and 0.006 Ω•cm. Single crystal, p-type silicon wafers with the (100) orientation and doped with boron were purchased from Silicon Quest International. The wafers had a diameter of 4 inches, a thickness between 500 and 550 μm, and an average resistivity between 7 and 9 Ω•cm. Gold (Au) substrates were prepared by depositing 100 nm of 99.999% Au via electron beam evaporation onto a quartz slide using a Temescal BJD 1800 vacuum deposition system from Technical Engineering Services, Inc. Highly oriented pyrolytic graphite (HOPG, Grade SPI-2) was purchased from SPI supplies. These four types of substrates were used as working electrodes to electrodeposit Se–Te films are referred to as n+Si(111), pSi(100), Au, and HOPG throughout the rest of this chapter.

For Si substrates, the wafer was cleaved into rectangular pieces with areas between 0.8 and 1.8 cm^2. A Ga–In liquid eutectic alloy was prepared by pulverizing the two metals together in a 75:25 weight ratio. Ohmic contact was made to the back of the Si wafer by scratching the Ga–In eutectic into the unpolished side of the wafer. A coiled tinned copper (Sn–Cu) wire was attached to back of the Si substrate with Ga–In eutectic and coated with conductive Ag paint to seal the wire onto the substrate. The wire was then threaded through a glass tube such that the surface-normal direction of the Si substrate was perpendicular to the glass tube. Hysol 9460 epoxy was used to seal the opening of the glass tube. The epoxy was allowed to dry in air for at least one hour before placing in a drying oven at 65°C for one hour. Nail polish was then used to cover the sides and back of the Si substrate such that electrodeposition of the Se–Te film occurred only on the polished, front side of the electrode.

For Au electrodes, a Sn–Cu wire was made into a ring around the perimeter of the

front side of the substrate and attached to the Au surface using Ag paint. The rest of the wire was threaded through a glass tube as described above. The exposed wire and Ag paint on the substrate were covered with nail polish. For HOPG electrodes, a layer of graphite was peeled from the HOPG substrate and affixed onto a fluorine doped tin oxide (FTO) glass substrate using carbon tape. Electrical contact was made to the HOPG layer in a similar way as for the Au substrates. The Au and HOPG electrodes had approximate areas of 0.5 cm^2 Immediately before use, each electrode was rinsed with 18.3 MΩ•cm resistivity H_2O from a Barnsted Nanopure water purification system and dried under a stream of nitrogen gas. The electrode was then briefly exposed to concentrated HCl by placing a drop of the acid on the electrode and letting it spread to cover the electrode surface. The nail polish surrounding the sides of the electrode prevented the drop of acid from spreading past the edge of the exposed electrode surface. To remove the surface oxide on Si substrates, the electrodes were additionally exposed to buffered HF using a similar procedure as for HCl. After each acid exposure the electrode was rinsed with 18.3 MΩ•cm resistivity H_2O and dried under a stream of nitrogen gas.

Photoelectrodeposition of Se–Te films. A Solartron Analytical potentiostat (Model 1287) was used to electrodeposit the Se-Te films using a three-electrode configuration. An Accumet glass-body standard calomel reference electrode (SCE) from Fisher Scientific was used to reference the potential applied to the working electrode via the potentiostat. A glass adapter was fitted around the SCE, which possessed a male 14/20 ground glass joint and ended in a glass tube. A Vycor frit was connected to the glass tube using heat shrink tubing. The counter electrode consisted of a piece of Pt gauze with approximate dimensions of 2 by 1.5 cm. A Pt wire was threaded through the gauze and soldered to a Sn–Cu wire. The Sn–Cu wire was then threaded through a glass tube and sealed with epoxy as described above. The cylindrical electrochemical cell had three female 14/20 ground glass joints to hold the counter, working, and reference electrodes. One side of the cell possessed a flat glass window such that the working electrode could be illuminated during electrodeposition.

The Se–Te films were electrodeposited under cathodic bias from aqueous solutions that contained 20 mM SeO_2, 10 mM TeO_2, 2 M H_2SO_4, and 0.2 M of $CdSO_4$. The addition of 0.2 M $CdSO_4$ to the deposition solution was found to improve both film adhesion and film quality as compared to 0.2 M $ZnSO_4$ or deposition without a metal sulfate. Fig. 2.16 shows that $CdSO_4$ is not a necessary ingredient to

produce the lamellar patterns formed under illumination, which are apparent both when $CdSO_4$ was replaced with $ZnSO_4$ or when no metal sulfate was added. When the deposition solution contained 0.2 M $CdSO_4$, films that were deposited at more negative potentials (e.g. at E = -0.80 V vs. SCE) showed presence of Cd only near the interface between the Se–Te film and the Si substrate as measured by x-ray photoelectron spectroscopy (Fig. 2.12).

Low resistivity, single crystal Si substrates that were n-type with a (111) orientation were typically used as the working electrode to deposit the Se–Te films. Si substrates that were p-type with a (100) orientation, evaporated Au films, and cleaved layers of HOPG, were also used as working electrodes, with similar results obtained on all substrates (Fig. 2.17). The potential, E, between the working and reference electrodes was typically held constant at E = -0.40, -0.60, or -0.80 V vs. SCE during deposition of the Se–Te films. Cyclic potential sweeps, linear potential sweeps, and square wave potentials were also used to electrodeposit films with similar results obtained for these different potential waveforms (see Table 2.1).

High power, light-emitting diodes (LEDs) were used to illuminate the working electrode during growth of the Se–Te films. LEDs with wavelengths of 365, 405, 455, 530, 625, 780, and 940 nm were purchased from Thor Labs. The LED illumination was passed through a 30 mm diameter, aspheric condenser lens (Thor, ACL3026) and a mounted Glan–Thompson calcite polarizer (Thor, GTH10M). The distance between the LED and the electrochemical cell were typically adjusted such that the beam diameter overfilled the area of the working electrode. The calcite polarizer was mounted in a rotation holder to rotate the polarization direction of the incident light. In some cases the glass tube of the working electrode was also mounted in a rotation holder to vary the angle of the incident light. An ELH halogen light bulb and a 633 nm He–Ne laser were also used as illumination sources. A 10× beam expander (Melle–Griot) was used to spread the beam of the He–Ne laser.

A calibrated Si photodiode (Thor, FDS 100–CAL) was used to measure the incident light intensity. Sn–Cu wires were soldered to the leads of the photodiode. The wires were threaded through a glass rod, which was sealed to the photodiode with epoxy in a similar manner as described above. The surface normal of the photodiode was oriented perpendicular to the glass tube. Before each run, the photodiode was placed in the electrochemical cell at the same position where the working electrode would be placed during film growth. The incident light intensity was measured, and the photodiode was removed and then replaced with the working electrode.

The specific conditions used to electrodeposit each sample are provided in Tables 2.1 and 2.2 below. Table 2.1 lists the type of substrate used as the working electrode, the area of the electrode, and the potential waveform applied during deposition. Table 2.2 lists the illumination conditions including the wavelength, polarization, incident angle, and intensity of the light source. The compositions of several samples were measured by energy dispersive spectroscopy and are provided in Table 2.2.

After film growth each electrode was rinsed with 18.3 MΩ•cm resistivity H_2O and then soaked in acetone. As the nail polish and Ag paint dissolved in the acetone, the substrate detached from the Sn–Cu wire, facilitating characterization of the film as described below. Cross-sections of the Se–Te films were prepared by scribing a line in the back of the Si substrate and then snapping the Si substrate into two pieces over a glass slide.

2.8 Supporting Figures and Tables

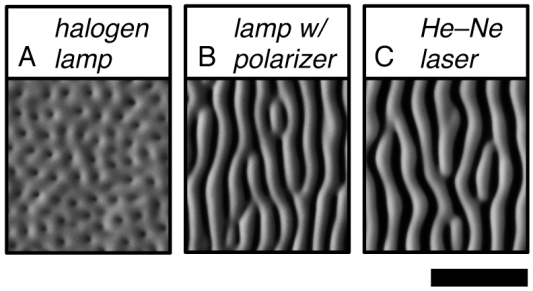

Figure 2.10: Photoelectrodeposition of Se–Te films using different illumination sources. (A) SEM image of a film grown under randomly polarized illumination from a halogen light bulb with an intensity of 46.5 mW/cm^2. (B) SEM image of a lamellar film grown under linearly polarized illumination from a halogen light bulb with an intensity of 44.7 mW/cm^2. (C) SEM image of a lamellar film grown under linearly polarized illumination from a 633 nm He–Ne laser with an intensity of 20.3 mW/cm^2. The scale bar is 1 μm and applies to all images.

Figure 2.10 shows SEM images of Se–Te films that were grown using different illumination sources. In Fig. 2.10A the lamellar pattern was grown under randomly polarized, broadband, non-coherent illumination from a halogen light bulb. The ELH bulb had a maximum irradiance at approximately 620 nm, and the pattern was similar to that formed under randomly polarized, 625 nm LED illumination (see Fig. 2.4A). However, when a linear polarizer was placed in front of the halogen light bulb, the lamellae oriented parallel to the polarization direction (Fig. 2.10B) similar to those formed using linearly polarized, 625 nm LED illumination (see Fig. 2.4).

Sample #	Sample shown in Figure X	Electrode area (cm^2)	Substrate	Potential wave form	Potential range (V)[a]	Sweep rate (mV/s)[b]	No. potential cycles[b]	Deposition time (s)[c]	Total charge passed (C/cm^2)[c]
1	1A, S2, S3	1.29	n+Si(111)	Constant	-0.80				-1.9
2	1B, S2	1.37	n+Si(111)	Constant	-0.80				-1.9
3	1D	1.84	n+Si(111)	Constant	-0.60				-1.9
4	1D	1.7	n+Si(111)	Constant	-0.80				-1.9
5	2A, S4A	1.29	n+Si(111)	Constant	-0.40			500	
6	2B, S4A	1.26	n+Si(111)	Constant	-0.40			500	
7	2C, S4A	1.15	n+Si(111)	Constant	-0.40			500	
8	2D, S4A	1.10	n+Si(111)	Constant	-0.40			500	
9	2E	1.16	n+Si(111)	Constant	-0.40			1000	
10	2F, S4B	1.20	n+Si(111)	Constant	-0.40			3000	
11	2G	1.34	n+Si(111)	Constant	-0.40				-1.25
12	2H	1.23	n+Si(111)	Constant	-0.60				-1.25
13	2I	1.29	n+Si(111)	Constant	-0.80				-1.25
14	3A	1.08	n+Si(111)	Cyclic sweep	0 to -1.0	20	3		
15	3B	1.07	n+Si(111)	Cyclic sweep	0 to -1.0	20	3		
16	3C	1.03	n+Si(111)	Cyclic sweep	0 to -1.0	20	3		
17, Run 1[d]	3D	0.80	n+Si(111)	Cyclic sweep	0 to -1.0	20	3		
17, Run 2	3D	0.80	n+Si(111)	Cyclic sweep	0 to -1.0	20	3		
18	3E	1.06	n+Si(111)	Square wave	0 V, 3 s -0.75 V, 4 s		110		
19	3F, 4	0.96	n+Si(111)	Constant	-0.40				-1.5
20	3G, 4	1.12	n+Si(111)	Constant	-0.40				-1.5
21	3H, 4	1.19	n+Si(111)	Constant	-0.40				-1.5
22	3I, 4	1.02	n+Si(111)	Constant	-0.40				-1.5
23, Run 1[d]	3J	1.42	n+Si(111)	Constant	-0.40				-1.5
23, Run 2	3J	1.42	n+Si(111)	Constant	-0.40				-1.5
24	3K	1.0	n+Si(111)	Constant	-0.40				-1.3
25	3L	1.12	n+Si(111)	Constant	-0.40				-1.3
26	3M	1.02	n+Si(111)	Constant	-0.40				-1.3
27	3N	1.10	n+Si(111)	Constant	-0.40				-1.3
28, Run 1[d]	3O	1.12	n+Si(111)	Constant	-0.40				-0.9
28, Run 2	3O	1.12	n+Si(111)	Constant	-0.40				-1.1
29	S1A	1.04	n+Si(111)	Constant	-0.40				-1.25
30	S1B	1.16	n+Si(111)	Constant	-0.40				-1.25
31	S1C	1.10	n+Si(111)	Constant	-0.40				-1.25
32	S3	0.98	n+Si(111)	Constant	-0.80				-1.2
33	S3	1.23	n+Si(111)	Constant	-0.40				-1.2
34	4, S6A	1.08	n+Si(111)	Constant	-0.40				-1.5
35	4, S6B	1.23	n+Si(111)	Constant	-0.40				-1.5
36	4, S6C	1.08	n+Si(111)	Constant	-0.40				-1.5
37	S7A, B	1.49	n+Si(111)	Constant	-0.60				-2.5
38	S7C, D	1.40	n+Si(111)	Constant	-0.60				-2.1
39	S7E, F	1.27	n+Si(111)	Constant	-0.60				-2.1
40	S8A	0.51	Au	Linear sweep	0 to -0.75	20	6		
41	S8B	0.49	Au	Linear sweep	0 to -0.75	20	6		
42	S8C	0.44	HOPG	Linear sweep	0 to -0.75	20	6		
43	S8D	0.45	HOPG	Linear sweep	0 to -0.75	20	6		
44	S8E	1.08	n+Si(111)	Cyclic sweep	0 to -1.0	20	5		
45	S8F	1.16	n+Si(111)	Cyclic sweep	0 to -1.0	20	5		
46	S8G	1.54	pSi(100)	Cyclic sweep	0 to -1.0	20	5		

Table 2.1: Table of deposition parameters

[a] A single potential value is provided for constant potential depositions. The initial and final potentials are provided for cyclic and linear potential sweeps.

[b] For a potential sweep, the sweep rate and number of cycles determined the total deposition time. In a cyclic sweep the potential was swept from the initial to the final value and then swept back to the initial value at the same rate before the next cycle. For a linear sweep, the potential was swept from the initial to the final value and then reset back to the initial potential before the next cycle. For a square wave potential the number of cycles refers to the number of times switched between the two listed potential values.

[c] For potentiostatic depositions, the growth was stopped either after a fixed amount of time or after a fixed amount of charge was passed between the working and counter electrodes.

[d] Run number indicates that deposition was stopped, and the illumination conditions were changed before the deposition was resumed on the same electrode.

Sample #	Sample shown in Figure X	Illumination wavelength (nm)[a]	Polarization orientation[b]	Angle of incidence (degrees)[b]	Light intensity (mW/cm^2)	Se:Te ratio from EDS
1	1A, S2, S3	Dark	-	-	-	58:42
2	1B, S2	625	Vertical	0	16.9	57:43
3	1D	Dark	-	-	-	56:44
4	1D	625	Vertical	0	18.7	60:40
5	2A, S4A	625	Vertical	0	2.8	-
6	2B, S4A	625	Vertical	0	5.6	54:46
7	2C, S4A	625	Vertical	0	11.3	56:44
8	2D, S4A	625	Vertical	0	18.9	62:38
9	2E	625	Vertical	0	18.7	63:37
10	2F, S4B	625	Vertical	0	18.6	64:36
11	2G	625	Vertical	0	18.6	-
12	2H	625	Vertical	0	18.8	-
13	2I	625	Vertical	0	18.6	-
14	3A	625	Unpolarized	0	14.6	53:47
15	3B	625	45°	0	14.5	49:51
16	3C	625	Horizontal	0	14.7	55:45
17, Run 1	3D	940	Vertical	0	31.0	-
17, Run 2	3D	940	Horizontal	0	31.0	-
18	3E	940	Rotated 5° CCW each cycle, 550° total	0	Did not record	-
19	3F, 4	365	Vertical	0	32.5	55:45
20	3G, 4	530	Vertical	0	14.6	53:47
21	3H, 4	780	Vertical	0	17.2	50:50
22	3I, 4	940	Vertical	0	29.8	57:43
23, Run 1	3J	940	Vertical	0	29.5	-
23, Run 2	3J	455	Vertical	0	29.0	55:45
24	3K	625	Vertical	0	18.8	58:42
25	3L	625	Vertical	20°	19.1	58:42
26	3M	625	Vertical	40°	18.8	58:42
27	3N	625	Vertical	60°	18.8	56:44
28, Run 1	3O	625	Vertical	60°	18.8	-
28, Run 2	3O	625	Vertical	-60°	18.8	62:38
29	S1A	ELH lamp	Unpolarized	0	46.5	56:44
30	S1B	ELH lamp	Vertical	0	44.7	58:42
31	S1C	633 nm He–Ne laser	Vertical	0	20.3	60:40
32	S3	625	Vertical	0	18.9	65:35
33	S3	625	Vertical	0	18.4	63:37
34	4, S6A	405	Vertical	0	23.2	57:43
35	4, S6B	455	Vertical	0	23.0	61:39
36	4, S6C	625	Vertical	0	16.0	52:48
37	S7A, B	625	Vertical	0	18.7	63:37
38	S7C, D	625	Vertical	0	18.7	62:38
39	S7E, F	625	Vertical	0	18.6	62:38
40	S8A	Dark	-	-	-	-
41	S8B	530	Vertical	0	8.9	-
42	S8C	Dark	-	-	-	54:46
43	S8D	530	Vertical	0	10.7	56:44
44	S8E	Dark	-	-	-	47:53
45	S8F	625	Vertical	0	18.6	51:49
46	S8G	530	Vertical	0	12.1	52:48

Table 2.2: Table of illumination parameters

[a] The illumination source was an LED unless otherwise noted.

[b] All top-down SEM images of the Se–Te films are oriented such that if the substrate was parallel to the plane of the page during growth then the illumination direction would have been normal to the page for a 0° incident angle. A vertical polarization orientation means the electric field vector of the incident light would have been parallel to the long edge of the page. For cross-sectional SEM images, the illumination direction would be in the plane of the page and parallel to the long edge of the page for a 0° incident angle. The polarization direction in cross-sectional images is normal to the plane of the page.

Fig. 2.10C shows that similar lamellar patterns were also formed using coherent and monochromatic 633 nm illumination from a He–Ne laser source. Thus, when the central wavelength and polarization direction were similar, the lamellar patterns resulting from illumination using a halogen light bulb, a LED, and a laser exhibited a similar period and orientation. All other lamellar patterns apart from Fig. 2.10 were grown using LED illumination.

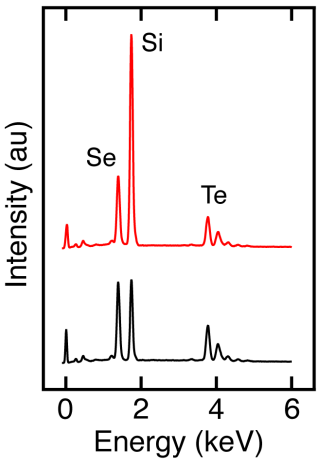

Figure 2.11: Energy dispersive spectra of Se–Te films grown in the dark and under illumination. The film grown in the dark (bottom, black trace) possessed an Se:Te atomic ratio of 58:42, while the film grown under illumination (top, red trace) possessed an Se:Te atomic ratio of 57:43. SEM images of the films are shown in Fig. 2.2A, B.

Figure 2.11 shows representative energy dispersive spectra, EDS, for the Se–Te films shown in Fig. 2.2A, B. Both films were electrodeposited on n+Si(111) substrates at E = -0.80 V vs. SCE until -1.9 C/cm^2 of charge had passed between the counter and working electrodes. One film was grown in the dark (black trace) and the other under linearly polarized, 625 nm illumination with an intensity of 16.9 mW/cm^2 (red trace). EDS indicated that the two films were composed of selenium and tellurium with the atomic ratio, Se:Te, equal to 58:42 for the film grown in the dark and 57:43 for the film under illumination. The Se:Te ratios for other samples are provided in Table 2.2. The composition of the Se–Te films was probed further by XPS, by use of an ion-sputtering gun to remove material while the spectra were recorded as a function of the film depth.

Figure 2.12A shows spectra in the binding energy regions for Te 3d (left graph) and Se 3d (right graph) photoelectron peaks for two Se–Te films grown at E = -0.80 V vs. SCE. One film was grown in the dark (black traces) and the other film was grown

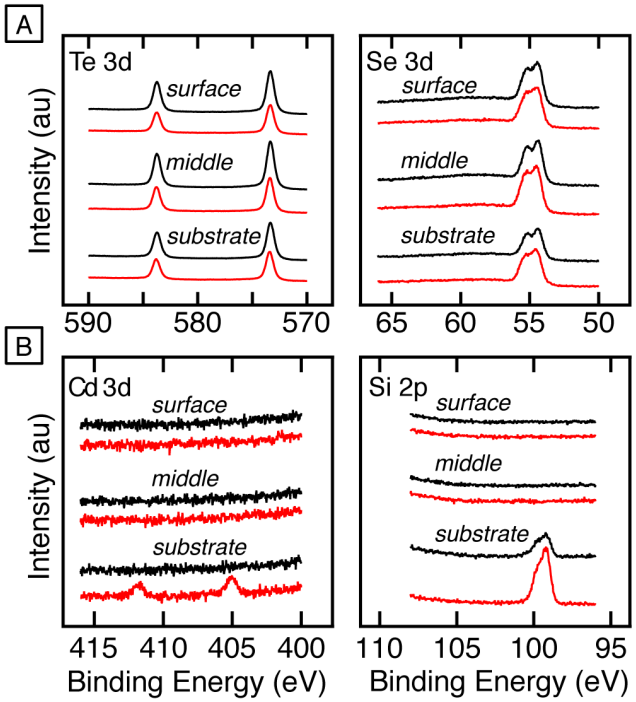

Figure 2.12: XPS depth profiling of Se–Te films grown under different illumination and electrochemical conditions. (A) Binding energy regions for Te 3d (left graph) and Se 3d (right graph) photoelectron peaks for two Se–Te films grown at a potential of E = -0.80 V vs. SCE in the dark (black traces) and under linearly polarized, 625 nm illumination with an intensity of 18.9 mW/cm^2 (red traces). From top to bottom in both graphs, the spectra were recorded after 30, 150, and 240 seconds of sputtering for the film grown in the dark (black traces) and after 30, 180, and 360 seconds of sputtering for the film grown under illumination (red traces). (B) Binding energy regions for Cd 3d (left graph) and Si 2p (right graph) photoelectron peaks for Se–Te films grown under linearly polarized, 625 nm illumination with an intensity of 18.9 mW/cm^2 at E = -0.80 V vs. SCE (red traces) and with an intensity of 18.4 mW/cm^2 at E = -0.40 V vs. SCE (black traces). From top to bottom in both graphs, the spectra were recorded after 30, 180, and 360 seconds of sputtering the film grown at E = -0.80 V vs. SCE (red traces) and after 30, 150, and 300 seconds of sputtering for the film grown at E = -0.40 V vs. SCE (black traces). A Cd signal was only observed for the film grown at E = -0.80 V vs. SCE at the interface with the Si substrate.

under linearly polarized, 625 nm illumination with an intensity of 18.9 mW/cm^2 (red traces). The peak positions are indicative of elemental Se and elemental Te and the relative peak intensities are similar for the two films. Fig. 2.12B shows spectra in the binding energy regions for Cd 3d (left graph) and Si 2p (right graph) photoelectron peaks for the same Se–Te film electrodeposited at E = -0.80 V vs. SCE under illumination (red traces) and another film that was grown under similar

illumination conditions but at E = -0.40 V vs. SCE (black traces). The two films possessed a similar bulk composition as measured by EDS (see rows 32 and 33 in Table 2.2). However, XPS depth profiling revealed the presence of Cd at the interface between the Se–Te film and the underlying Si substrate only for the film grown at the more negative potential of E = -0.80 V vs. SCE.

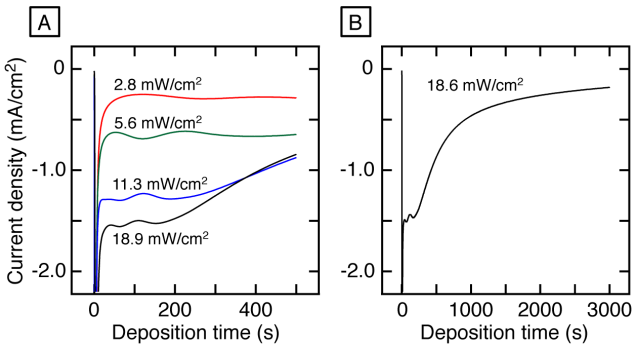

Figure 2.13: Current density during potentiostatic photoelectrodeposition of Se–Te films. (A) Plots of current density vs. deposition time for Se–Te films grown at E = -0.40 V vs. SCE for 500 s under linearly polarized, 625 nm light with intensities of 2.8, 5.6, 11.3, and 18.9 mW/cm^2. SEM images for these films are shown in Fig. 2.3A–D. (B) Plot of current density vs. deposition time for an Se–Te film grown at E = -0.40 V vs. SCE for 3000 s under linearly polarized, 625 nm light with an intensity of 18.6 mW/cm^2. An SEM image of this film is shown in Fig. 2.3F.

Figure 2.13A shows the deposition current density for films grown at E = -0.40 V vs. SCE for 500 s under linearly polarized, 625 nm illumination with intensities of 2.8, 5.6, 11.3, and 18.9 mW/cm^2. SEM images of the films are shown in Fig. 2.3A–D. Fig. 2.13B shows the deposition current density for the film shown in Fig. 2.3F, which was grown E = -0.40 V vs. SCE for 3000 s under linearly polarized, 625 nm illumination with an intensity of 18.6 mW/cm^2. The current density slowly decreased during electrodeposition at a constant potential due to the increasing resistance drop across the film.

Fig. 2.14A shows the current densities for Se–Te electrodeposition on n+Si(111) substrates under chopped illumination at E = -0.40, -0.60, and -0.80 V vs. SCE. In all three traces the illumination was linearly polarized at a wavelength of 625 nm with an intensity between 18.2 and 18.3 mW/cm^2. Fig. S5B shows the current density for Se–Te electrodeposition on a Au substrate at E = -0.40 V vs. SCE under chopped illumination that was linearly polarized at a wavelength of 625 nm with an intensity of 16.6 mW/cm^2. Table 2.3 provides the current densities in the dark and under illumination along with the photocurrent enhancement (i.e. ratio of the

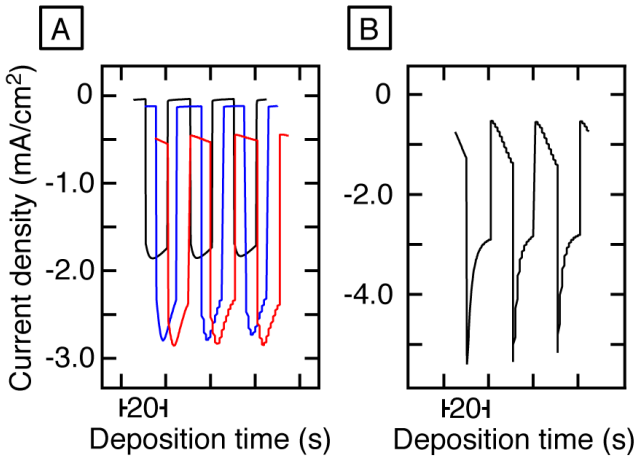

Figure 2.14: Current density for Se–Te electrodeposition under chopped illumination at different applied potentials and using different growth substrates. (A) Films grown on n+Si(111) substrates under chopped, linearly polarized, 625 nm with an intensity between 18.2 and 18.3 mW/cm^2 at E = -0.40 V (left, black trace), -0.60 V (middle, blue trace), and -0.80 V (right, red trace) vs. SCE. The traces have been offset in time for clarity. (B) Film grown on a Au substrate under chopped, linearly polarized, 625 nm with an intensity of 16.6 mW/cm^2 at E = -0.40 V. The average current densities in the dark and under illumination and the photocurrent enhancement ratio for these traces are provided in Table S3.

current density under illumination to the current density in the dark) for these four samples.

Substrate	Applied potential (V vs. SCE)	Dark current density (mA/cm^2)	Light intensity (mW/cm^2)	Current density under illumination (mA/cm^2)	Photocurrent enhancement ratio
n+Si(111)	-0.40	-0.05	18.2	-1.79	36
n+Si(111)	-0.60	-0.12	18.3	-2.55	21
n+Si(111)	-0.80	-0.48	18.3	-2.62	5
Au	-0.40	-0.88	16.6	-3.42	4

Table 2.3: Current densities in the dark and under illumination for Se–Te electrodeposition at different applied potentials and on different substrates.

Figure 2.15 shows SEM images of lamellar patterns grown under linearly polarized illumination with wavelengths of 405, 455, and 625 nm. These three samples along with the four samples shown in Fig. 2.4–I were used to measure the lamellar period vs. illumination wavelength shown in Fig. 2.5.

Figure 2.16 shows the effect of adding $CdSO_4$ or $ZnSO_4$ at a concentration of 0.2 M to the electrodeposition solution. Phototropic growth of the lamellar patterns was

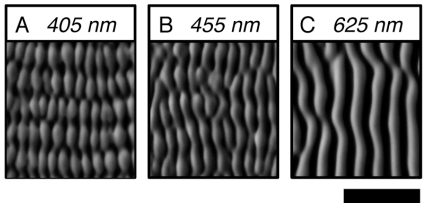

Figure 2.15: Wavelength dependence of lamellar period continued from Fig. 2.4. SEM images of lamellar patterns grown under linearly polarized illumination with wavelengths of (A) 405 nm, (B) 455 nm, and (C) 625 nm. These three samples along with the four shown in Fig. 2.4F–I were used to plot the lamellar period vs. illumination wavelength shown in Fig. 2.5. The scale bar is 1 μm and applies to all images.

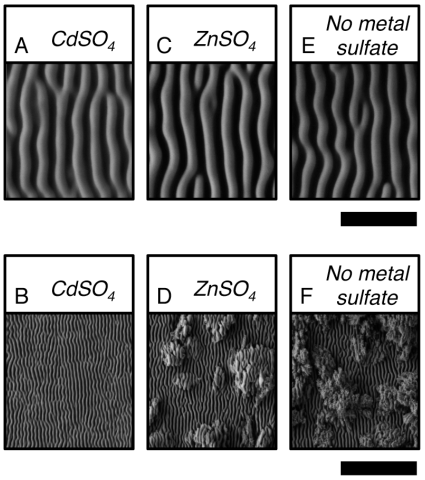

Figure 2.16: Photoelectrodeposition of Se–Te films with different metal sulfates added to the deposition solution. All deposition solutions contained 20 mM SeO_2, 10 mM TeO_2, and 2 M H_2SO_4. All films were electrodeposited at E = -0.60 V vs. SCE under linearly polarized, 625 nm illumination with an intensity between 18.6 and 18.7 mW/cm^2. (A) High magnification and (B) low magnification SEM images of a film grown using a deposition solution that also contained 0.2 M $CdSO_4$. (C) High magnification and (D) low magnification SEM images of a film grown using a deposition solution that also contained 0.2 M $ZnSO_4$. (E) High magnification and (F) low magnification SEM images of a film grown using a deposition solution that did not contain a metal sulfate. The scale bar is 1 μm for the top row of images (A, C, E) and 5 μm for the bottom row of images (B, D, F).

observed in both cases as well as in the case where no metal sulfate was added (see high magnification images in Fig. 2.16A, C, E). The addition of $CdSO_4$ improved both adhesion of the Se–Te films to the Si substrate as well as the uniformity of the Se–Te films (see low magnification images in Fig. 2.16B, D, F). Therefore,

the deposition solution contained 0.2 M $CdSO_4$ for all other films described in the work. While the presence of Cd was detected by XPS at the interface between the Si substrate and the Se–Te film, analysis by XRD (Fig. 2.2), EDS (Fig. 2.11), and XPS (Fig. 2.12) all indicate that the bulk of the films were composed of an alloy of elemental Se and elemental Te.

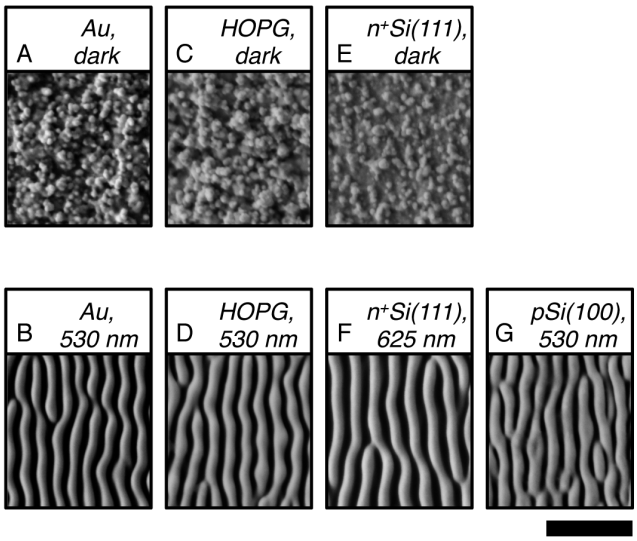

Figure 2.17: Electrodeposition of Se–Te films on different substrates in the dark and under illumination. (A) Dark electrodeposition of Se–Te on an evaporated Au film. (B) Electrodeposition on an evaporated Au film under linearly polarized, 530 nm illumination with an intensity of 8.9 mW/cm^2. (C) Dark electrodeposition of Se–Te on a HOPG film. (D) Electrodeposition on HOPG under linearly polarized, 530 nm illumination with an intensity of 10.7 mW/cm^2. (E) Dark electrodeposition of Se–Te on a n+Si(111) substrate. (F) Electrodeposition on n+Si(111) under linearly polarized, 625 nm illumination with an intensity of 18.6 mW/cm^2. (G) Electrodeposition of Se–Te on pSi(100) under linearly polarized, 530 nm illumination with an intensity of 12.1 mW/cm^2. The scale bar is 1 μm and applies to all images.

Figure 2.17 shows SEM images of Se–Te films grown on different substrates used as the working electrode during electrodeposition. Electrodeposited Se–Te films grown in the dark on n+Si(111), Au, and HOPG substrates showed a similar granular morphology (Fig. 2.17A, C, E). Phototropic growth of the lamellar patterns was observed for films grown under illumination on these same substrates as well as for pSi(100) substrates (Fig. 2.17B, D, F, G). The Se–Te films could only be deposited on the photoconductive pSi(100) substrates under illumination due to the high resistivity (7 to 9 Ω•cm) of these substrates in the dark.

2.9 Optical Properties of Photoelectrochemically Deposited Films

Reflection of Films

The reflection of electrochemically deposited films grown under polarized illumination were measured in an integrating sphere setup as described in Michael Kelzenberg's Ph.D. thesis [73]. The measurements were done with respect to the usual angular, wavelength and polarization variables as well as the sample orientation dependence. Due to the anisotropy of the films, the polarization and angle measurements were parameterized relative to the orientation of the lamellar structures as depicted in Figure 2.18.

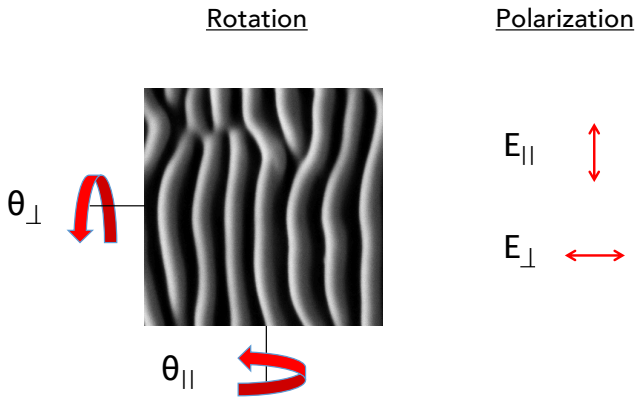

Figure 2.18: Orientation dependent coordinates for integrating sphere reflection measurements. The propagation direction of the illumination source was perpendicular to the page for all measurements.

Figures 2.19, 2.20 and 2.21 show the total reflection (both specular and diffuse) from samples grown under three wavelengths: 405 nm, 625 nm, and 780 nm respectively. Top-down SEM images of films grown under similar conditions can be found in Figures 2.4 and 2.15. The reflection of light polarized perpendicular to the long axis of the lamellae was generally lower than light polarized parallel to the structures for incidence angles below 40 degrees. However, one exception to this was observed for the film grown under 405 nm light where a highly absorptive region between 400 and 550nm for angles between 0 and 50 degrees had a reflection minimum of ≈ 0.05 for incidence angles along the $\theta_{\parallel}$ and $\theta_{\perp}$. This feature could be due to the additional periodicity along the long axis of the lamellae that was observed at shorter illumination wavelengths (Figures 2.4 and 2.15).

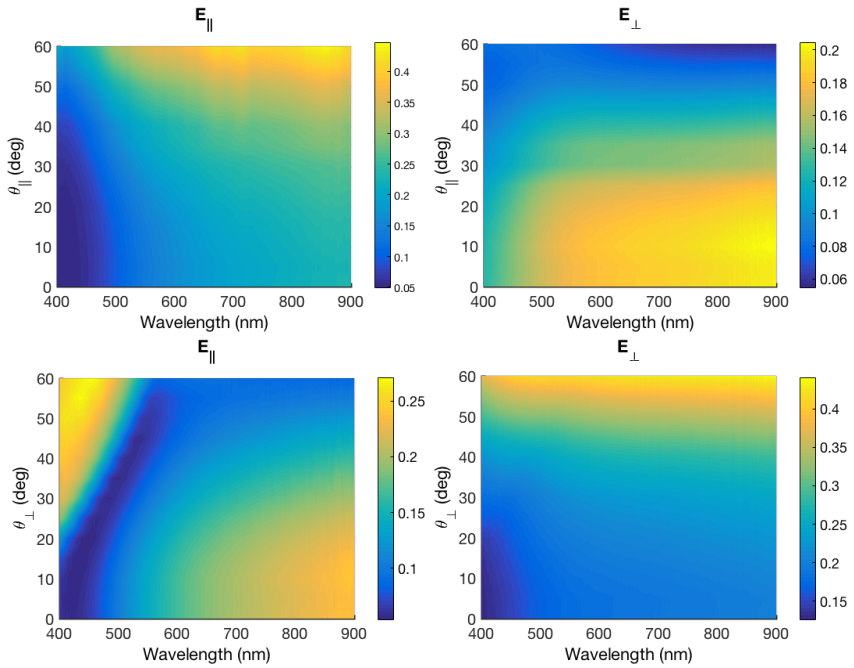

Figure 2.19: Measured reflection, normalized to incident intensity, from a film grown under linearly polarized 405 nm illumination.

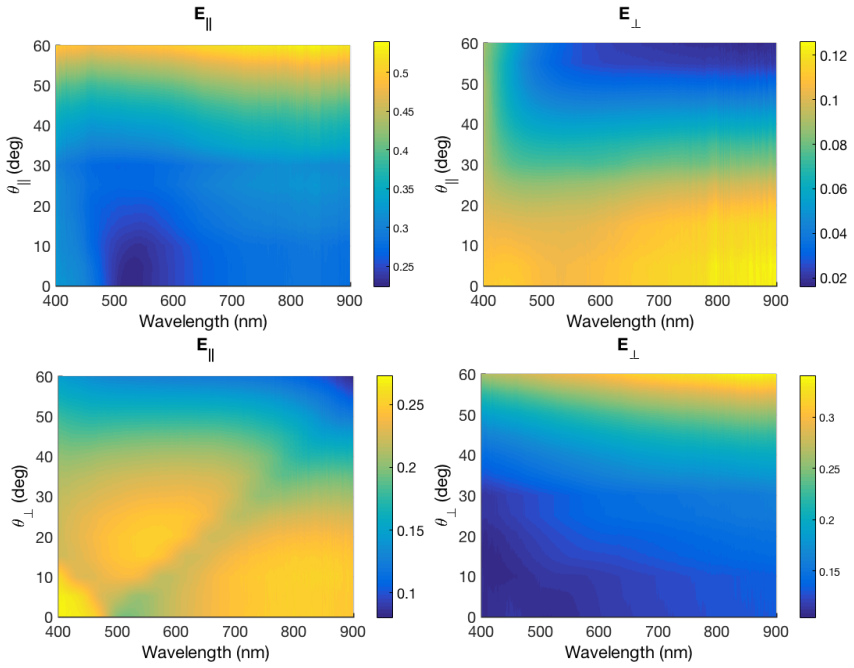

Figure 2.20: Measured reflection, normalized to incident intensity, from a film grown under linearly polarized 625 nm illumination.

Diffraction of Films

The films grown under linearly polarized illumination exhibited iridescence by eye. This iridescence is illustrated in Figure 2.22 A-C, which was captured with a hand-

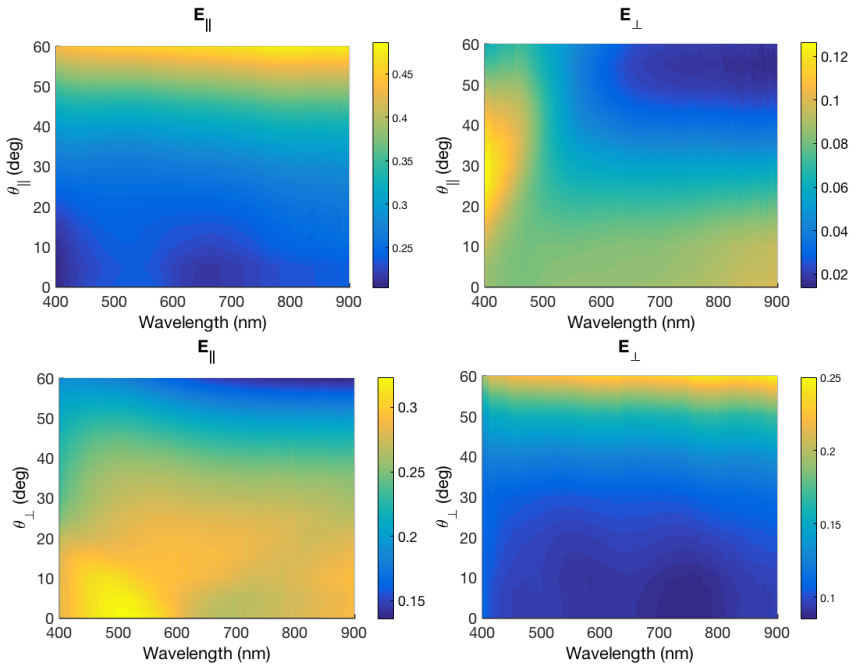

Figure 2.21: Measured reflection, normalized to incident intensity, from a film grown under linearly polarized 780 nm illumination.

held camera. A white LED illumination source near the camera lens was used as a broad band illumination source while images were recorded at different angles. The film reflected colors ranging from the blue to red as the camera angle was swept from normal incidence to in plane. Figure 2.22 D shows a top down SEM image of a film grown under similar conditions as the sample exhibited in panels A-C.

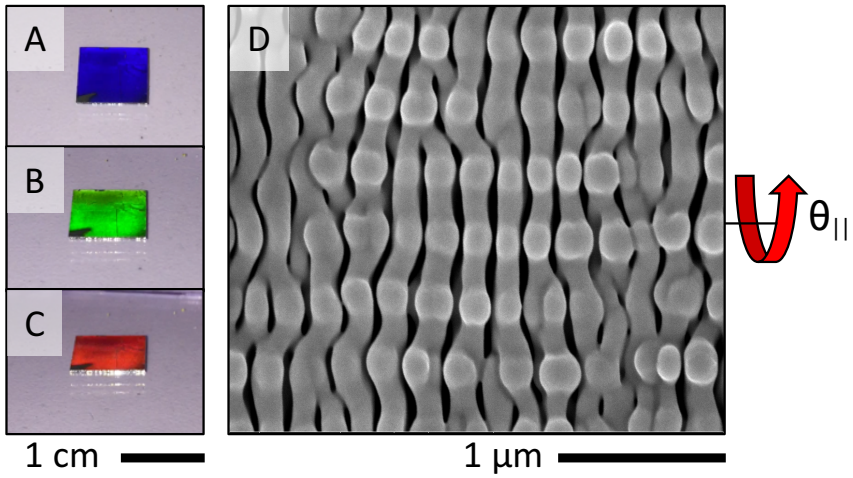

Figure 2.22: Observed iridescence for a lamellar film grown under short wavelengths.

The periodicity of the film was calculated through Fourier analysis (see the following chapter) as having a vertical period of 411 nm and a horizontal period of 211. By using the diffraction equation (Eq. 2.12), the expected diffraction angles for a grating period of 411 nm were calculated.

$$\theta_m = arcsin\left(\frac{m\lambda}{d} - sin(\theta_i)\right) \tag{2.12}$$

The predicted diffraction of a several illumination wavelengths are depicted in Figure 2.23 for three different illumination angles. These calculations show that for a pitch of 411 nm, the diffracted light in the visible range is expected to be directed to the same side of the grating surface normal. Moreover, as the illumination angle is swept from normal incidence (0 degrees) towards the grating plane (90 degrees), one would expect to observe different colors of light to be directed back towards the illumination source. For example, an illumination angle of 45° produce orange diffracted light angled back at the source. Smaller angles of incidence would produce shorter wavelength light at the source position while larger angles of incidence would produce longer wavelengths at the source position. These results agree with the trend observed experimentally in Figure 2.22.

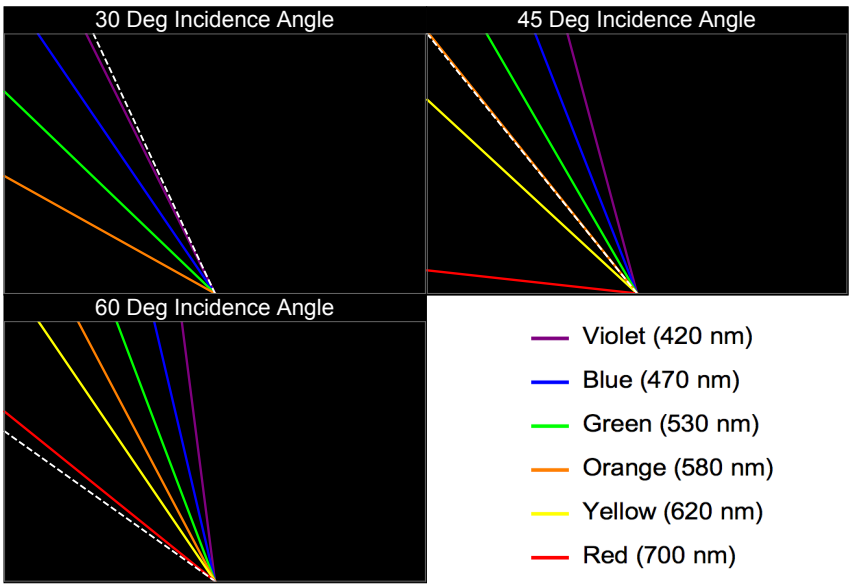

Figure 2.23: Predicted first order diffraction angles for a 411nm pitch grating. Incident illumination is shown arriving from the left.

Chapter 3

PATTERN FORMATION UNDER TWO ILLUMINATION WAVELENGTHS

In the previous chapter, we observed that the photoelectrochemical growth of Se-Te alloy films using polarized, incoherent light produced highly anisotropic, nanoscale lamellar patterns wherein the spacing and size of the lamellar features was a function of the illumination wavelength. The light source was not structured physically nor required to have a long-coherence length, and the electrolyte was isotropic, yet the morphology of the photoelectrodeposited material realized a self-organized, highly anisotropic nanoscale pattern due to the light-matter interactions between the constituents of the system during growth. Deposition occurred in the dark but at a rate much slower than under illumination. The morphology of the deposit generated in the dark was isotropic and unpatterned, whereas the morphology of the deposit generated under polarized illumination was patterned and anisotropic, and the long axes of the lamellae align parallel to the transmission axis of the polarizer. We also saw phenomenon can be exploited to generate complex, patterned three-dimensional structures.

In this chapter we detail an investigation between the morphologies of photoelectrodeposited Se-Te films and the spectral profiles of the illumination utilized during growth of the films. Deposition has been performed in the presence of an array of narrowband, broadband and multi-modal illumination profiles, respectively, to determine the morphology produced by changes in the properties of the optical excitation. Subsequent Fourier analysis was utilized to provide a quantitative description of the patterns, and the patterns were accurately reproduced by computational modeling and simulation of the light-material interactions during growth of the films.

The experimental methods section provides detailed descriptions of the methods used for the photoelectrodeposition of the Se-Te films. Briefly, the films were electrochemically deposited at room temperature from an aqueous acidic solution (0.0200 M SeO_2, 0.0100 M TeO_2, in 2.00 M H_2SO_4) onto a freshly etched n+-Si substrate that was biased potentiostatically at -0.40 V versus a Ag/AgCl (3 M KCl) reference electrode for 2.5 min. The substrate was illuminated during deposition with variety of light-emitting diode (LED), halogen-lamp, and/or laser sources that

had controlled intensity profiles.

3.1 Experimental Observations

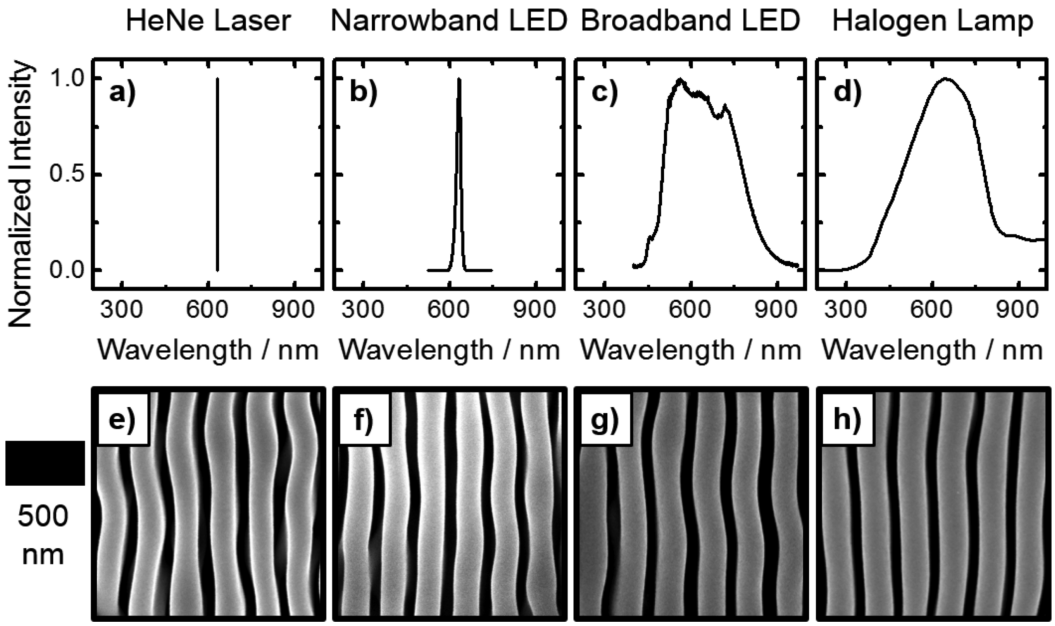

Figure 3.1: Effect of the spectral bandwidth of the vertically polarized illumination sources on the morphology of the photoelectrodeposited Se-Te films. (a)-(d) Spectral profiles for indicated sources. (e)-(h) Corresponding scanning electron micrographs representative of the resulting photoelectrodeposited films.

Se-Te photoelectrodeposits produced by illumination with polarized, narrowband coherent or incoherent light form lamella that are aligned along the optical polarization direction, with a periodicity proportional to the incident optical wavelength. Figure 3.1(a)-(d) presents spectral profiles of four light sources that had very similar intensity-weighted average wavelengths (λavg) but had very different spectral bandwidths: a HeNe laser with λavg = 633 nm and a bandwidth (full-width at half-max, FWHM) « 1 nm; a narrowband light-emitting diode (LED) with λavg = 630 nm and FWHM = 18 nm; a broadband LED with λavg = 646 nm and FWHM = 283 nm; and a tungsten-halogen lamp with λavg = 640 and FWHM = 420 nm. Figure 3.1(e)-(h) presents representative scanning-electron micrographs (SEMs) of photoelectrodeposits generated by the potentiostatic electrochemical reduction of SeO_2 and TeO_2 under illumination with each separate, vertically polarized light source. The Se-Te films exhibited mutually similar morphologies regardless of which illumination source was utilized (Figure 3.1). These morphologies are similar to ripple patterns that are generated using laser surface processing, known as laser-induced periodic

surface structures (LIPSS).[14, 24, 29] However, formation of LIPSS requires coherent, highly monochromatic and extremely intense (typically at kW cm^{-2} or MW cm^{-2} scales) laser excitation, whereas none of the illumination sources utilized in this work had all of these qualities.[20, 28] Moreover, the broadband LED and halogen lamps produced light that was incoherent and highly polychromatic, with intensities on the order of mW cm^{-2}. Thus, it is apparent that a distinct mechanism must control the pattern formation in this system.

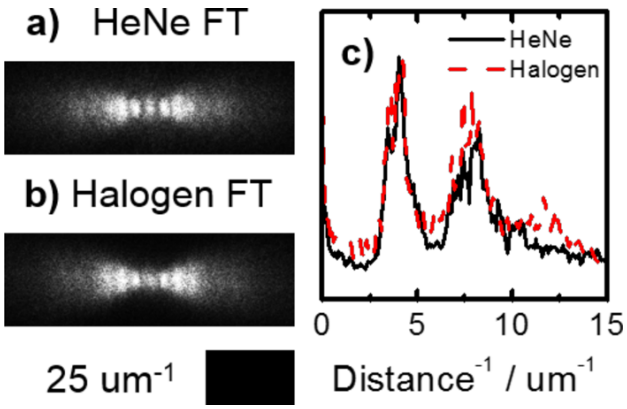

Figure 3.2: (a) and (b) Representative 2D Fourier transforms generated from SEMs of the films photoelectrodeposited using the indicated sources. (c) Fourier spectra generated by integrating the grayscale intensity along a narrow band starting at the center and extending out along the horizontal axis of the Fourier images presented in (a) and (b).

Figure 3.2(a) and (b) present two-dimensional Fourier transforms (2D FTs) of the SEM data of the photoelectrodeposited films using the HeNe laser and the tungsten-halogen lamp, respectively. A bright spot in a 2D FT corresponds to a periodic component in the SEM from which the 2D FT was derived. Moreover, in a 2D FT, the distance of any spot from the center indicates the frequency of the component, and the relative location indicates the direction of the periodicity. Thus the spots along the horizontal axes in Figures 3.2(a) and (b) are indicative of horizontal periodicity in the SEMs and thus in the morphologies of the deposits. The similarity between the 2D FTs suggests that similar periodicities of the lamellar morphologies were generated with both the laser and the lamp. By integrating the gray-scale intensity along a narrow band starting at the center and extending out along the horizontal axis of the 2D FT, a Fourier spectrum was generated to enable quantitative analysis of the data. Figure 3.2(c) presents Fourier spectra corresponding to the 2D FTs in Figure 3.2(a) and (b). The extremely close agreement between the Fourier spectra

describing the morphologies generated with the laser and lamp indicates a very similar periodic nature of these two morphologies despite a difference of several orders of magnitude between the bandwidths of the two sources.

The inverse of the lowest frequency maximum in each Fourier spectrum was equal to the lamellar periodicity (i.e. distance between identical points on two neighboring lamellae). The higher frequency maxima were integral multiples of the lowest maximum, and thus simply represent overtones of a fundamental frequency. The presence of overtones at higher frequencies is expected because the shapes of the lamellae are not perfectly described by a single sinusoidal function. The lack of any other components beyond a singular set of harmonics suggests that each morphology can be well-described by a single period. Thus despite the broadband source providing photons with widely differing excitation wavelengths, only a singular morphological periodicity was produced, exactly as is observed when a single periodicity results from a laser source that instead provides photons having only an extremely narrow distribution of wavelengths. Quantitatively, the real-space lamellar periodicity determined from the Fourier spectra was 245 ± 4 nm for deposits generated with the laser and 250 ± 3 nm for the lamp based on at least 5 independent measurements of each type of sample. Similar analysis of the deposits generated with LED sources resulted in a value of 244 ± 4 nm for the narrowband LED and 252 ± 8 nm for the broadband LED, again based on at least 5 independent measurements of each type of sample.

Collectively, the results obtained with the sources of varying bandwidths indicate that the lamellar periodicity is determined by an effective average source wavelength. This concept was investigated further by performing the photoelectrodeposition with spectral profiles that produced an intensity-weighted average spectral wavelength at a value at which the source had no actual intensity. Such profiles were obtained by simultaneously illuminating the sample with two narrowband LED sources. Figure 3.3(a) presents the spectral profile that resulted from illumination with a narrowband LED with λavg = 630 nm in conjunction with illumination from another narrowband LED having λavg = 461 nm. Figure 3.3(b) presents a SEM of a deposit generated with only 461 nm illumination and Figures 3.3(c) and (d) present SEMs of deposits generated with simultaneous illumination at 461 nm and 630 nm, as a function of the fraction of the total delivered intensity that was provided by each narrowband light source. Figure 3.10 presents a larger set of representative SEMs of photoelectrodeposits generated using different fractions of 461 nm and

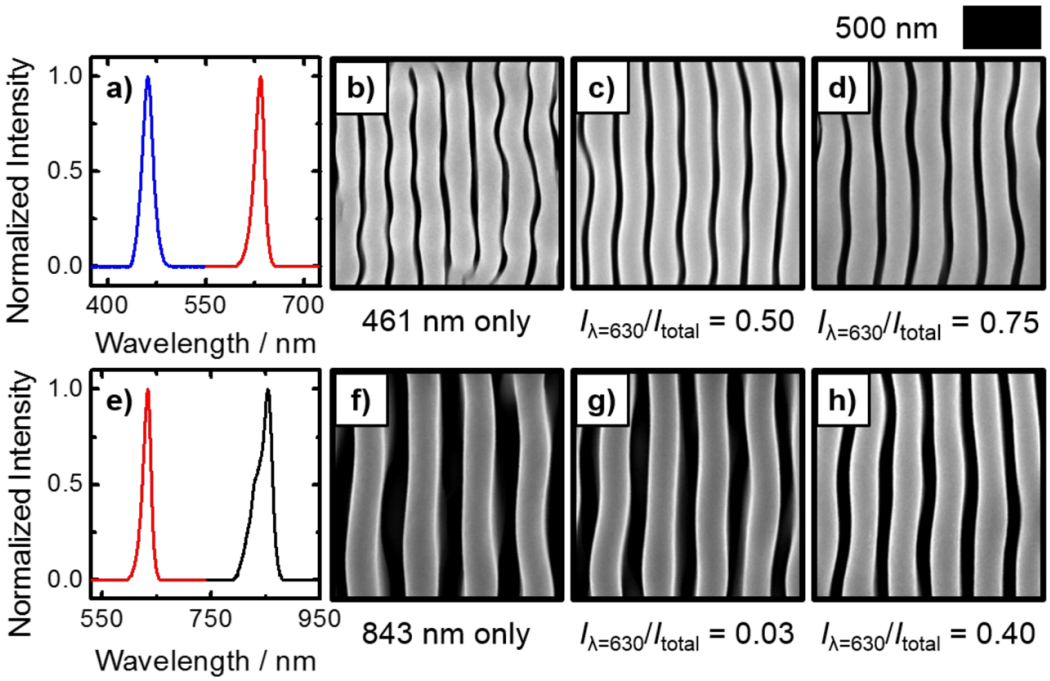

Figure 3.3: Effect of simultaneous illumination with two discrete narrowband sources on the morphology of the photoelectrodeposited Se-Te films. (a) Spectral profile of the illumination resulting from the combination of two narrowband LED sources with λavg values of 461 nm and 630 nm (at an arbitrary intensity ratio). (b)-(d) SEMs representative of the photoelectrodeposits resulting from illumination with a similar spectral profile as in (a) with the indicated intensity ratio between the two sources. (e)-(h) Same as (a)-(d), but with a source with a λavg value of 843 nm rather than 461 nm.

630 nm illumination. The SEMs observed from a deposit generated using 461 nm illumination displayed a smaller lamellar periodicity than was observed for the corresponding deposit grown using 630 nm illumination. Deposits generated using illumination with both wavelengths appeared to display intermediate periodicities. Figures 3.3(e)-(f) present analogous data, but with an LED having λavg = 843 nm rather than 461 nm. A larger set of SEMs is additionally presented in Figure 3.11. As noted in the experiment using 461 nm and 630 nm sources, the deposition under illumination with the longer wavelength source alone generated what appeared to be the largest periodicity, while deposits formed under illumination by both sources simultaneously resulted in lamellar periods intermediate between those observed for deposition with either source alone.

Fourier analysis was also used to analyze the periodicity of the patterns in the photoelectrodeposits grown using simultaneous illumination from two narrowband

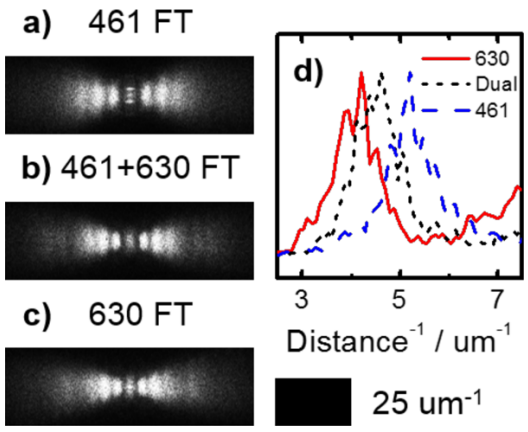

Figure 3.4: Representative 2D Fourier transforms of SEMs of photoelectrodeposits generated using (a) a single narrowband source with a λavg value of 461 nm, (b) two narrowband sources with λavg values of 461 nm and 630 nm, and (c) a single narrowband source with a λavg value of 630 nm. (c) Fourier spectra generated by integrating the grayscale intensity along a narrow band starting at the center and extending out along the horizontal axis of the Fourier images presented in (a)-(c).

sources. Figure 3.4(a)-(c) presents 2D FTs of SEMs of the deposits generated with illumination provided by the 461 nm source alone, the 461 and 630 nm sources together, and the 630 nm source alone. Each 2D FT displayed discrete bright spots along the horizontal axis, and the spacing of these spots was the greatest in the 2D FT of the 461 nm sample and smallest in the 2D FT of the 630 nm sample. The spacing in the 2D FT of the dual-wavelength sample was intermediate between the spacings for the 461 nm and 630 nm samples. In all three cases, the corresponding Fourier spectra generated from integration of these three 2D FTs revealed that the only observable components were a fundamental and the corresponding overtones. Figure 3.4(d) presents the corresponding Fourier spectra in the region of the fundamental. The fundamental peak in each spectrum was centered at a different value along the abscissa, and the center of the dual-wavelength peak was intermediate between the centers of both related single-wavelength peaks. Thus, under the conditions investigated, photoelectrochemical growth with two discrete narrowband sources resulted in a deposit that had only a single characteristic morphological period, and had no detectable beat frequencies in contrast to expectations based on simple interference.

Figure 3.5(a) presents a plot of the lamellar period derived from the 2D FTs of SEM images of photoelectrodeposits generated with simultaneous illumination at 461 nm and 630 nm as a function of the source composition (in order of increasing

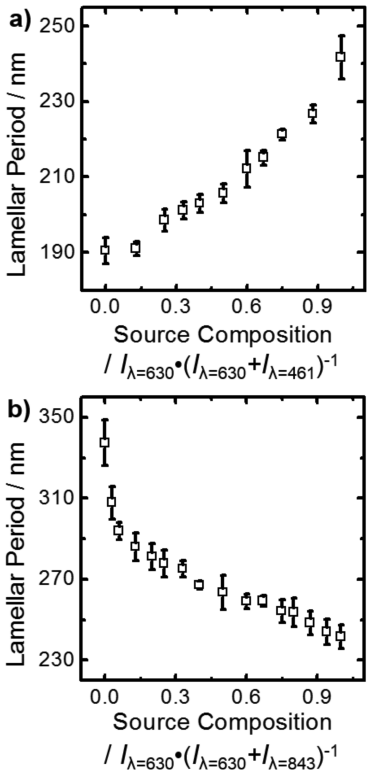

Figure 3.5: a) and (b) Plots of lamellar period of the photoelectrodeposit as a function of the fraction of the total intensity provided by the 630 nm source utilized during growth.

630 nm content). Figure 3.5(b) presents analogous data characteristic of photoelectrodeposits generated with 630 nm and 843 nm illumination. In both cases, the lamellar periods observed for photoelectrodeposits generated using simultaneous illumination with two different wavelengths were intermediate between those observed for photoelectrodeposits generated with either one of the two constituent wavelengths alone. In both cases, the lamellar period scaled monotonically between these limits as a function of source composition, in an inverse logistic-like curve. Such behavior has several implications. First, by utilization of two sources with differing wavelengths, a structure with any period between the limits defined by the periods observed for growth with either source alone can be generated simply by varying the relative intensity of the two sources. Second, under such conditions the growth is sensitive to the characteristics of both sources, because the lamellar period reflected the engineered spectral profile of the illumination under every condition investigated. In fact, near the extremes of the source composition, wherein one source supplied the majority of the intensity, the lamellar period was generally the

most sensitive to a change in source composition.

3.2 Elemental Composition of Photoelectrodeposits

The elemental composition of all of the photoelectrodeposits was analyzed using energy-dispersive X-ray spectroscopy (EDS). All analyzed films were found to be wholly composed of Se and Te. Photoelectrodeposits generated using the HeNe laser (λavg = 633 nm) were found to on average to have compositions of 38 atomic % Se (remainder Te). Photoelectrodeposits generated with the narrowband LED with λavg = 630 nm, the broadband LED with λavg = 646 nm, and the tungsten-halogen lamp with λavg = 640 nm were found to on average have compositions of 37, 37 and 39 atomic % Se, respectively. The uncertainty inherent in the EDS measurement was 5 atomic % and thus the differences between these values are not significant. Figure 3.6(a) presents a plot of the elemental composition (in terms of atomic % Se) of the photoelectrodeposits generated with simultaneous illumination at 461 nm and 630 nm as a function of the source composition (in order of increasing 630 nm content). Figure 3.6(b) presents analogous data pertaining to the photoelectrodeposits generated with simultaneous illumination at 630 nm and 843 nm. In both cases, photoelectrodeposits were found to on average have compositions of 37 atomic % Se and all the average compositions were found to range between 37 and 39 atomic % Se. Again, these values were within experimental uncertainty and as such these values are statistically equivalent. Thus, no variation in photoelectrodeposit elemental composition was found between any of the experimental parameters investigated in this work.

Additionally, EDS analysis was also performed on several different spatial locations on each photoelectrodeposit. The variability in observed elemental composition was 2 atomic % Se. This variability is less than the experimental uncertainty, indicating that the photoelectrodeposits are spatially conformal within the certainty afforded by EDS analysis.

3.3 Modeling of Pattern Formation under Two Discrete Wavelengths

Modeling and simulation of the photoelectrochemical growth process was performed to determine if the morphologies observed for films generated using simultaneous illumination with narrowband sources evolved as a result of the fundamental light-matter interactions that occurred during the deposition. The same two-step, iterative model described in the previous chapter was utilized. Figure 3.7(a), (b), and (c), respectively, present 2D simulations (cross-sectional view) of the morphologies of

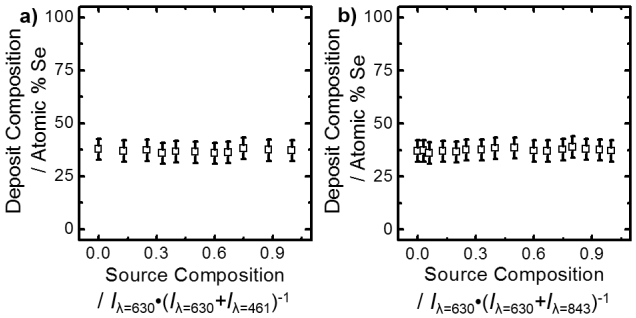

Figure 3.6: (a) and (b) Plots of the elemental composition of the photoelectrodeposit in terms of atomic % of Se as a function of the fraction of the total intensity provided by the 630 nm source utilized during growth. Photoelectrodeposits were composed wholly of Se and Te.

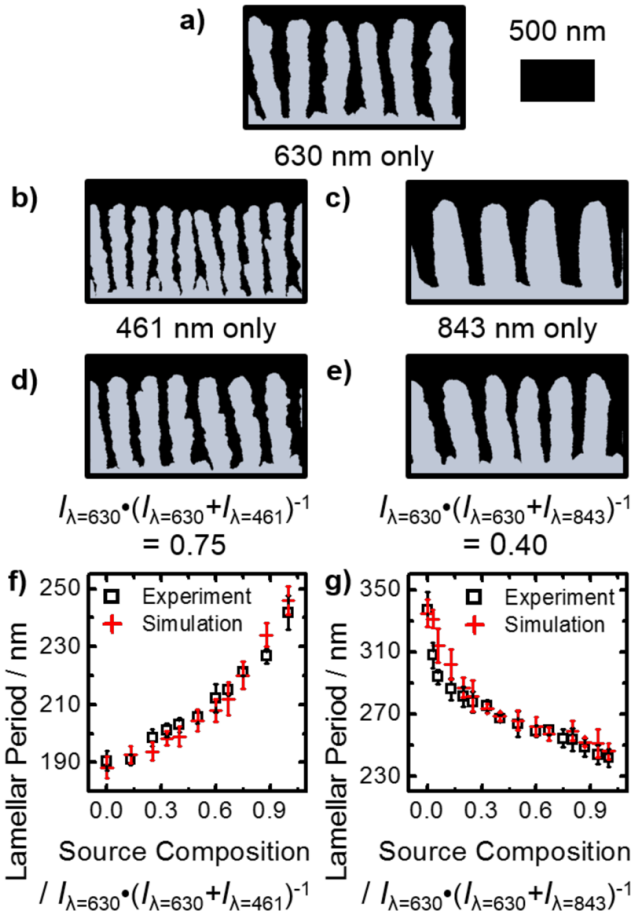

Figure 3.7: (a)-(e) 2D simulations of photoelectrodeposits generated with indicated illumination source(s). (f) and (g) Plots of lamellar period of the experimental and simulated photoelectrodeposit morphologies as a function of the fraction of the total intensity provided by the 630 nm source utilized during growth/modeling.

photoelectrodeposits generated using illumination at 630 nm, 461 nm, and 843 nm alone. The morphological periodicity in each presented simulation was in good agreement with that observed experimentally (Figure 3.1(f), Figure 3.3(b) and (f)). Figure 3.7(d) and (e) present 2D simulations of the morphologies of photoelectrodeposits generated with illumination at 630 nm simultaneously with illumination at either 461 nm or 843 nm, respectively. In both cases, the simulated morphologies displayed periodicities that were intermediate between those observed in the simulations of morphologies generated under illumination with either of two sources alone. Moreover, the simulated morphologies were in good agreement with those observed experimentally (Figure 3.3(d) and (h)). Thus, the modeling and simulation agreed qualitatively with the experimental data.

The lamellar period in the simulated structures was derived from FT analysis, in an analogous fashion to analysis of the structures that were observed experimentally (Figure 3.2). Figure 3.7(f) presents the lamellar period of the morphologies of the simulated photoelectrodeposits, as well as the corresponding experimental morphologies, for growth under simultaneous illumination at 461 nm and 630 nm sources as a function of source composition (in order of increasing 630 nm content). Figure 3.7(g) presents analogous data characteristic of simulations and photoelectrodeposits that were obtained by simultaneous use of 630 nm and 843 nm illumination. The experimental and simulated values of the lamellar period matched quantitatively in both cases. Such quantitative agreement between the model and experiment indicates that any arbitrary illumination profile during growth encoded for a singular lamellar period. Additionally, the specific period appears spontaneously in the photoelectrodeposit due only to the interactions between the illumination and the evolving deposit during growth.

The generation of the highly anisotropic, periodic lamellar pattern is directly the result of highly differing rates of mass addition along the film surface. Specifically, to perpetuate the morphological asymmetry, the local growth rate must be greatest at the tip of the lamellar surface. Light absorption provides the driving force in the model for photoelectrochemical deposition, hence the success of the iterative growth model in reproducing the observations indicates that generation of the periodic lamellar pattern requires the absorption of light to be greatest in the tips of the lamellar structure and less than maximal in areas other than the tips of the structure. The experimental results and growth model also collectively indicated that a lamellar pattern having a single periodicity is always formed under the

conditions investigated, regardless of the spectral profile of the illumination. Collectively, the experiments and simulations suggest for a given illumination profile, the photoelectrodeposition process spontaneously self-selects the lamellar period that will maximize light absorption at the tips of the lamellar structures. A set of light-absorption simulations were performed considering an idealized lamellar structure, to verify that the experimentally observed periods were those that maximized the anisotropy of the light absorption.

Figure 3.8(a) provides a schematic for the simulation area that contained the idealized structure, consisting of a 400 nm tall lamella that had a hemispherical upper bound atop a 100 nm conformal layer of the electrodeposit. The illumination was simulated to be incident with a propagation vector parallel to the lamellar tip. Periodic boundary conditions were used to simulate an array of lamellae. The structure was considered as two segments, "top" and "bottom", with the boundary between the two segments located at the height at which the surface normal of the tip was 45 degrees from horizontal. A figure of merit, Ξ, was defined as the ratio of absorbed photons in the interfacial region of the top versus that of the bottom. For a given illumination profile, Ξ was calculated over a series of lamellar periods. Figure 3.8(b) illustrates the dependence of Ξ on the lamellar period for simultaneous illumination at 461 nm and 630 nm with several experimentally investigated source compositions. Each Ξ-curve had a single maximum, which shifted to a larger value of the lamellar period for illumination profiles as the 630 nm content of the illumination increased. Figure 3.8(c) presents a plot of the lamellar period at Ξmax for simulations involving simultaneous illumination at 461 nm and 630 nm, as a function of the source composition. The experimentally observed values are also presented in Figure 3.8(c). The stair-step shape of the Ξ-derived curve is an artifact that arose because the simulations considered the structure as many finite, but insufficiently small, units. Identical simulations that instead involved smaller units exceeded the available computational resources. Nevertheless, the values of the lamellar period that maximized Ξ matched semi-quantitatively with the analogous experimental values. To accommodate computational limitations while improving the accuracy of the model, Ξ was recalculated with simulations that utilized a finer discretization of the structure, but only was performed in a narrow range of lamellar periods near the previously observed maxima (using the coarser discretization), for every experimentally investigated source composition. Figure 3.8(d) presents the derived plot of the lamellar period at new the values of Ξmax, along with the related experimental data. Figure 3.8(e) presents an analogous

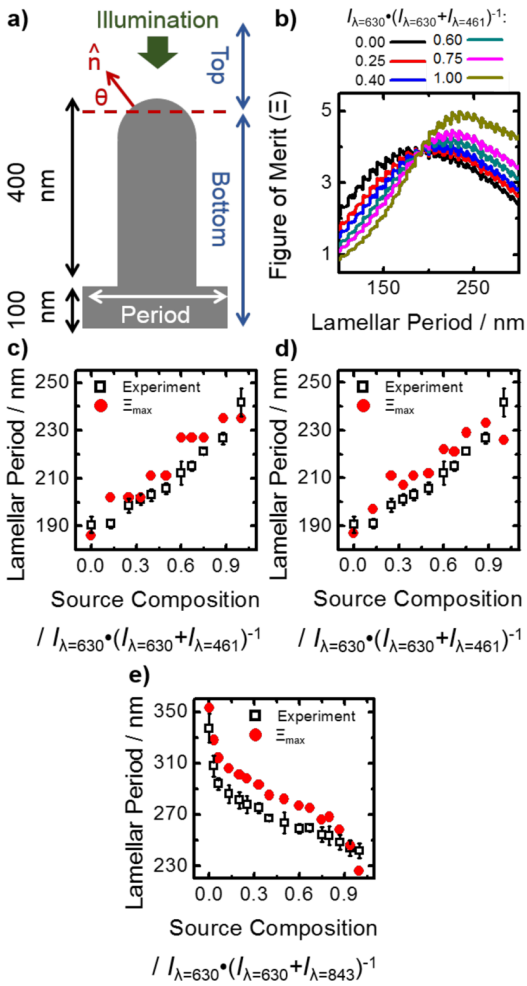

Figure 3.8: (a) Diagram of the simulation area containing an idealized lamellar structure utilized for calculations of the spatial concentration of light absorption. The lamella was divided into top and bottom segments at the height at which the surface normal of the tip ($\hat{n}$) was at an angle $\theta = 45$ degrees from the horizontal. Plane-wave illumination was incident from the top of the structure, with a propagation oriented normal to the substrate. (b) Plots of figure of merit, Ξ, or light absorption in the top surface of the idealized structure normalized by that in the bottom, as a function of lamellar period for simultaneous illumination at 461 nm and 630 nm with the indicated source composition. (c) Plot of the experimentally observed lamellar period and the lamellar period which maximized Ξ as a function of the fraction of the total intensity provided by the 630 nm source utilized during growth/modeling. (d) and (e) Same as (c) but based on simulations utilizing a finer discretization of the lamellar structure.

plot for simultaneous illumination with 630 nm and 843 nm. The lamellar periods that maximized Ξ followed the same trend with respect to source composition as the experimentally measured periods, and the two sets of values matched essentially

quantitatively. The agreement between the experimental data and the simulations indicates that the observed photoelectrochemical growth spontaneously optimized the lamellar period in a way that maximized the anisotropy of the light absorption.

3.4 Conclusions

In summary, under the conditions investigated, photoelectrochemical deposition utilizing linearly polarized illumination has been shown to result spontaneously in an ordered nanoscale lamellar morphology, regardless of the wavelength distribution of the illumination source. Fourier analysis demonstrated that this morphology was consistently described by only a single periodicity. Utilization of several illumination profiles with different bandwidths but having a common intensity-weighted average wavelength resulted in structures that had a mutually common, singular periodicity. Similarly, illumination profiles that consisted of two narrowband sources generated structures that had singular periodicities which were a function of the relative contribution of each source to the total illumination intensity. Simulation of the growth process with such illumination spectral profiles showed that this phenomenon could be described by considering only the fundamental light-matter interactions that govern the photoelectrochemical growth process. Further simulations of light absorption under the same illumination profiles indicated that the photoelectrodeposition process is consistent with a self-optimization process that maximizes the anisotropy of light absorption in the structure along the growth front.

3.5 Experimental Methods

Materials and Chemicals $(CH_3)_2CO$ (ACS Grade, BDH), H_2SO_4 (ACS Reagent, J. T. Baker), HF (49 %, Semiconductor Grade, Puritan Products), In (99.999 %, Alfa Aesar), Ga (99.999 %, Alfa Aesar), SeO_2 (99.4 %, Alfa Aesar), and TeO_2 (99+ %, Sigma-Aldrich) were used as received. H_2O with a resistivity $\geq$ 18.2 MΩ cm (Barnstead Nanopure System) was used throughout. n+-Si(111) (0.004 – 0.006 Ω cm, As-doped, 400 ± 15 μm, single-side polished, Addison Engineering) was used as a substrate for deposition. Flash-Dry Silver Paint (SPI Supplies), Double/Bubble Epoxy (Hardman) and nitrocellulose-based nail polish were used to assemble the Si working electrodes.

Electrode Preparation One end of a Sn-coated Cu wire (22 AWG) was bent to form a small, flat coil and the wire was then threaded through glass tubing (6 mm O. D.) such that the coil was just outside the tubing. Epoxy was applied to seal the end of the tube from which the coil protruded. Square Si wafer sections (ca. 5 mm by 5

mm) were cut and a eutectic mixture of Ga and In was scratched into the unpolished surfaces with a carbide scribe. The wire coil was then contacted to the unpolished surface and affixed with Ag paint. Nail polish was applied to insulate the unpolished face, the wire-coil contact and the exposed wire between the coil and epoxy seal. Immediately before deposition, the Si surface of each electrode was cleaned with $(CH_3)_2CO$, and then the Si section of the electrode was immersed in a 49 wt. % solution of HF(aq) for 10 s, to remove any surficial SiO_x from the Si. The electrode was then rinsed with H_2O, and then dried under a stream of N_2(g).

Photoelectrochemical Deposition All photoelectrochemical deposition was a carried out using a Bio-Logic SP-200 potentiostat. Deposition was performed in a single-compartment glass cell with a quartz window. A three-electrode configuration was utilized with a graphite-rod counter electrode (99.999 %, Sigma-Aldrich) and a Ag/AgCl reference electrode (3 M KCl, Bioanalytical Systems). Films were deposited from an aqueous solution of 0.0200 M SeO_2, 0.0100 M TeO_2, and 2.00 M H_2SO_4. Deposition was effected by biasing the illuminated n+-Si electrode potentiostatically at -0.40 V vs. Ag/AgCl for 2.50 min at room temperature. After deposition, the electrode was immediately removed from the cell, rinsed with H_2O, and then dried under a stream of N_2(g). The Si substrate with top-facing Se-Te film was mechanically separated from the rest of the electrode assembly. The nitrocellulose-based insulation, as well as the majority of the Ag paint and In-Ga eutectic, were then removed mechanically.

Alloying Se with Te reduces the band gap of the material, enhancing light absorption.[72] The energetically favorable co-deposition of Se and Te reduces the influence of the solution composition on the generated alloy composition. If the alloy composition could be a varied, a change in the periodicity of the morphology that occurs as a result of photoelectrochemical preparation may be observed in response to a change in the relevant optical properties, such as the refractive index, of the material. We have not explicitly investigated the effects of the forced convection in the solution on the nature of the deposit, since the purpose of this study was to investigate the effects of varying the interaction between the light field and growing matter in the deposit under conditions similar to those used in prior work in the absence of specifically tuned spectral distributions of the incident illumination.

Electrode Illumination Illumination for the majority of the photoelectrochemical depositions was provided by narrowband diode (LED) sources (Thorlabs) with respective intensity-weighted λavg values and spectral bandwidths (FWHM) of 461

nm and 29 nm (M470L2), 630 nm and 18 nm (M625L3), and 843 nm and 30 nm (M850L3). Additionally, a HeNe laser (Aerotech LSR5P) emitting at 632.8 nm in a TEM00 mode with linear polarization, a broadband diode (LED, Thorlabs MBB1L3) with a relatively flat intensity profile between 500 and 750 nm (λavg = 646 nm) and a spectral bandwidth (FWHM) of 280 nm, and an ELH-type tungsten-halogen lamp (Phillips 13096) with a λavg value of 640 nm and a spectral bandwidth (FWHM) of 420 nm, were also used as light sources. The output of each diode source was collected and collimated with an aspheric condenser lens (Ø30 mm, f = 26.5 mm). The HeNe laser was fitted with a 10x beam expander (Melles-Griot) to create a spot that overfilled the working electrode. For experiments involving simultaneous illumination with two different wavelengths, a dichroic filter (Edmund Optics #69-900 or #69-219) was utilized. Both sources were incident upon a filter surface at an angle of 45 degrees from the surface normal, generating coaxial output. A dichroic film polarizer (Thorlabs LPVISE2X2 or LPNIRE200-B) was used to polarize the illumination from all of the narrowband diode sources. For experiments involving simultaneous illumination from two sources, the polarizer was placed after the dichroic filter to ensure that all of the light that reached the electrode shared a single polarization vector. Illumination from the broadband diode and from the tungsten-halogen lamp was polarized using an ultra-broadband wire-grid polarizer (Thorlabs WP25M-UB). No polarization optic was used in conjunction with the HeNe laser. A 1500 grit ground-glass (N-BK7) diffuser was placed immediately in front of the photoelectrochemical cell to ensure spatial homogeneity of the illumination. The light intensity incident on the electrode was measured by placing a calibrated Si photodiode (Thorlabs FDS100) in the place of an electrode assembly in a photoelectrochemical cell with electrolyte, and measuring the steady-state current response of that Si photodiode. Depositions that utilized a single diode as the illumination source were performed with a light intensity of 25.0 mW cm^{-2} at the electrode. Depositions with the HeNe laser were performed with a light intensity of 10.0 mW cm^{-2}. Depositions with the halogen lamp were performed with a light intensity of 50.0 mW cm^{-2}. Depositions utilizing the diodes with λavg values of 630 nm and 461 nm in conjunction were performed with a total light intensity of 25.0 mW cm^{-2}. Depositions utilizing the diodes with λavg values of 630 nm and 843 nm in conjunction were performed with a total light intensity of 50.0 mW cm^{-2}.

Microscopy Scanning electron micrographs (SEMs) were obtained with a FEI Nova NanoSEM 450 at an accelerating voltage of 5.00 kV with a working distance of 5 mm and an in-lens secondary electron detector. Micrographs obtained for quantitative

Fourier analysis were acquired with a resolution of 172 pixels μm-1 over ca. 120 μm2 areas. Micrographs utilized to produce display figures were acquired with a resolution of 344 pixels μm-1 over ca. 8 μm2 areas.

Energy-dispersive X-ray Spectroscopy Energy dispersive X-ray spectroscopy (EDS) was performed in the SEM using an accelerating voltage of 15.00 kV and a working distance of 12 mm. An Oxford Instruments X-Max silicon drift detector was utilized. Spectra were collected in the range of 0 to 10 keV and quantitative film compositions were derived from these spectra using the "INCA" software package (Oxford Instruments).

3.6 Modeling and Simulation Methods

Simulation of Film Morphology The growths of the photoelectrochemically deposited films were simulated with an iterative growth model wherein electromagnetic simulations were first used to calculate the local photocarrier-generation rates at the film surface. Then, mass addition was simulated via a Monte Carlo method wherein the local photocarrier-generation rate weighted the local rate of mass addition along the film surface.

Growth simulations began with a bare, semi-infinite planar Si substrate. In the first step, the light-absorption profile under a linearly polarized, plane-wave illumination source was calculated using full-wave finite-difference time-domain (FDTD) simulations with periodic boundary conditions along the substrate interface. In the second step, a Monte Carlo simulation was performed in which an amount of mass, equaling that of a 15 nm planar layer covering the simulation area, was added to the upper surface of the structure with a probability F:

$$F(G) = \left[1 + G\left(n_0\tau_p + p_0\tau_n\right) + G^2\frac{\tau_p\tau_n}{n_i^2}\right]\prod_{i=1}^{3}\frac{x_i}{r_i} \tag{3.1}$$

where G is the spatially-dependent photocarrier generation rate at the deposit-solution interface, n_i is the intrinsic carrier concentration, n_0 is the electron concentration, p_0 is the hole concentration, τn is the electron lifetime, τp is the hole lifetime, x_i is the fraction of i$^{\text{th}}$ nearest neighbors occupied in the cubic lattice, and r_i is the distance to the i$^{\text{th}}$ nearest neighbor. The multiplicative sum in the definition of this probability (Equation 3.1) serves to reduce the surface roughness of the film so as to mimic the experimentally observed surface roughness.

After the initial Monte Carlo simulation, the absorbance of the new, structured film was then calculated in the same manner as for the initial planar film, and an additional Monte Carlo simulation of mass addition was performed. This process of absorbance calculation and mass addition was repeated for a total of 30 iterations.

Simulation of Spatial Concentration of Light Absorption The spatial concentration of light absorption in idealized versions of the lamellar-type structure generated by photoelectrochemical growth was investigated via a series of full-wave electromagnetic simulations.

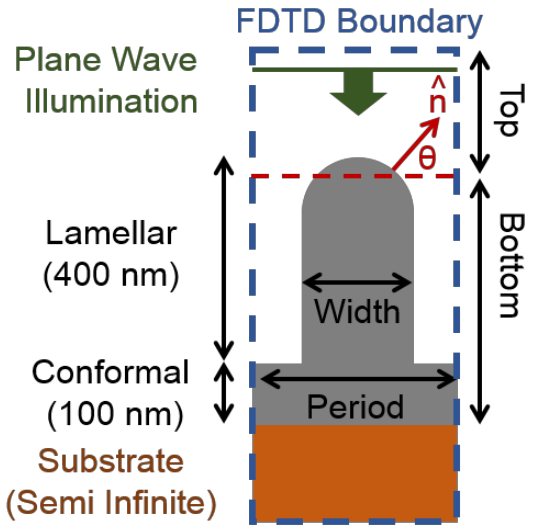

Figure 3.9: Diagram of simulation area containing an idealized lamellar structure utilized for calculations of spatial concentration of light absorption. A 400 nm tall lamellar deposit, a 100 nm conformal deposit, and a semi-infinite substrate were considered, with each component atop the next. The lamella was divided into top and bottom segments at the height at which the surface normal of the tip ($\hat{n}$) was at an angle $\theta = 45$ degrees from the horizontal. Periodic boundary conditions were utilized. Plane-wave illumination incident at the top of the structure and with a propagation direction oriented along the lamellar axis was considered.

Figure 3.9 provides a schematic of the simulation area. The idealized structure, from bottom to top, consisted of a semi-infinite Si substrate, a 100 nm conformal Se-Te layer, and a 400 nm tall Se-Te lamella with a hemispherical upper boundary. The lamella was separated into top and bottom regions at the height at which the surface normal to the hemispherical tip was 45 degrees from horizontal. A figure of merit, Ξ, was defined as the ratio of number of absorbed photons at the top solid/solution interface to the number of absorbed photons at the bottom solid/solution interface. The value of Ξ was thus proportional to the degree of light concentration in the

top of the lamellar structure. Calculation of Ξ was limited to photons that were absorbed within 10 nm of the interface. Ξ was calculated for lamellar periods ranging from 100 to 400 nm. The width of structures in the simulations was set as the product of the lamellar period and the empirically derived filling fraction for the illumination condition under analysis (quantified by contrast-thresholding the same SEMs utilized for Fourier analysis).

General Parameters Se–Te films were assumed to be undoped (i.e. $n_0 = p_0 = n_i$) and a value of $n_i = 10^{10}$ cm^{-3} was used for the intrinsic carrier concentration.[62] A value of 1 μs was used for both the electron and hole lifetimes.[63] Previously measured values of the complex index of refraction for Se-Te were utilized.[74] A value of n = 1.33 was used as the refractive index of the electrolyte regardless of wavelength.[75] Illumination intensities identical to those used experimentally (see Section 3.5) were used in the simulations. Illumination spectral profiles for each relevant source were the same as those presented in Figure 3.1 and Figure 3.3 (see main text) for the FOM calculations described above. Simulations of the film morphology utilized the peak intensity wavelength of the experimental sources described in Section 3.5. The electric field vector of the illumination was oriented parallel to the substrate. A two-dimensional square mesh with a lattice constant of 1 nm was used for the simulations. All FDTD simulations were performed using the "FDTD Solutions" software package (Lumerical).

3.7 Supporting Figures

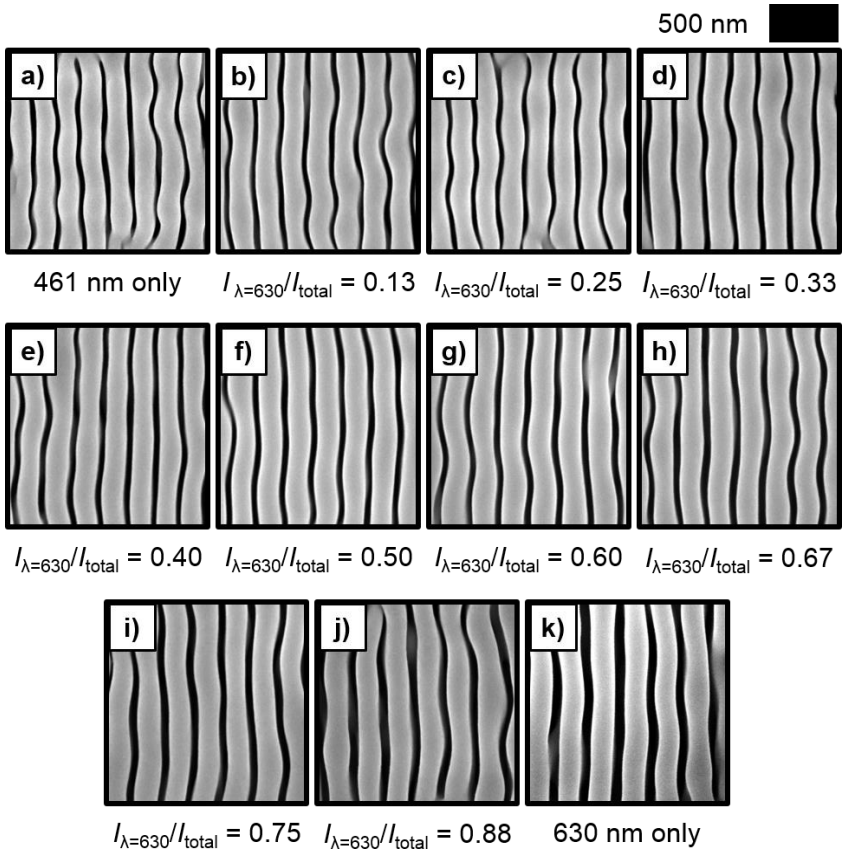

Figure 3.10: SEMs representative of resultant photoelectrodeposit from simultaneous illumination with LED sources with λavg values of 461 nm and 630 nm (spectral profiles as indicated in Figure 3.3(a)) with the indicated intensity ratio between the two sources.

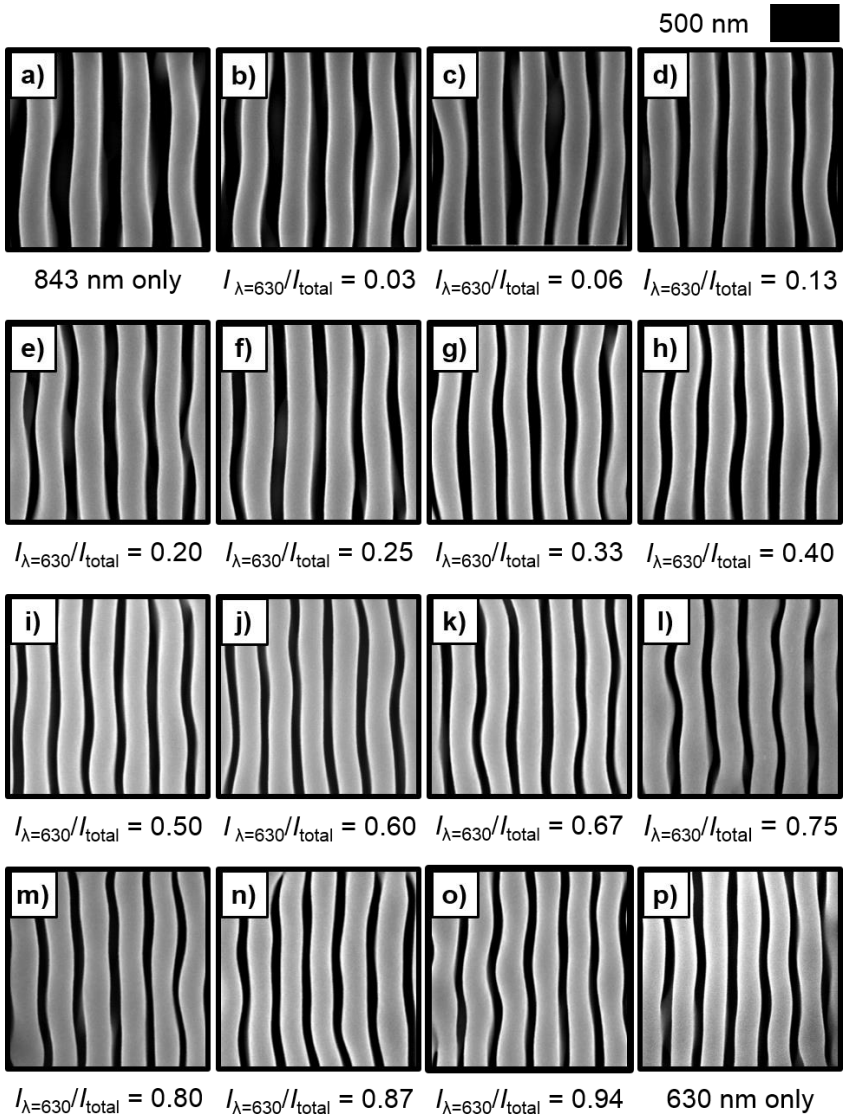

Figure 3.11: SEMs representative of resultant photoelectrodeposit from simultaneous illumination with LED sources with λavg values of 843 nm and 630 nm (spectral profiles as indicated in Figure 3.3(e)) with the indicated intensity ratio between the two sources.

Chapter 4

PATTERN FORMATION UNDER TWO POLARIZATIONS

Manipulation of the polarization of the light is another control mechanism that can be utilized to direct photodriven processes and produce targeted structures. Linearly polarized light can effect photopolymerization and/or photoalignment in liquid crystal systems, generating highly anisotropic structures oriented along or perpendicular to the electric field vector.[76–79] The photoinduced mass transport of photoisomerizable polymers in the immediate vicinity of Au or Ag nanoparticles can generate patterns in the subwavelength regime with an anisotropy dictated by the polarization of the light source.[80–83] Additionally, plasmon-mediated growth of surface-affixed triangular Ag nanoparticles during illumination with linearly polarized light results in spontaneous anisotropic orientation as well as consistent particle size.[84] This synthetic process is governed by the anisotropies in the light-material interactions resulting from sensitivity to both the wavelength and polarization of the illumination, and thus provides for the maskless generation of uniform, oriented nanostructures.[15]

We saw in the previous two chapters that the photoelectrochemical growth of semiconducting Se-Te films using linearly polarized illumination was shown to produce highly anisotropic, nanoscale lamellar patterns in which the orientation of the patterns is correlated with the electric field vector of the incident light. Such structures were formed without the use of any physical or chemical templating agents nor the use of a photomask unlike other techniques.[85–90] Rather, in analogy to the case of the plasmon-mediated growth of Ag nanostructures, patterning resulted spontaneously due to inherent anisotropies in the light-material interactions during film growth.

In this chapter, the patterns generated in photoelectrochemically grown Se-Te films utilizing two light sources with unique linear polarizations were investigated to understand the material growth response to the tailored excitation, as well as to identify strategies for obtaining morphology control and for generating three-dimensional morphological complexity. Films were generated using two same-wavelength sources with an array of polarization vector pairs as well as intensity ratios, and with two orthogonally polarized different-wavelength sources that had a series of

intensity ratios. The resulting film morphologies were assessed by scanning electron microscopy. Computational modeling of the light-material interactions during photoelectrochemical growth successfully reproduced the experimentally observed morphologies. Additional modeling of light scattering at the active film-solution interface, as well as simulations of light absorption in idealized lamellar arrays, were also performed to understand the emergence of the morphologies generated using two discrete linear polarizations of light to drive film growth.

4.1 Experimental Observations

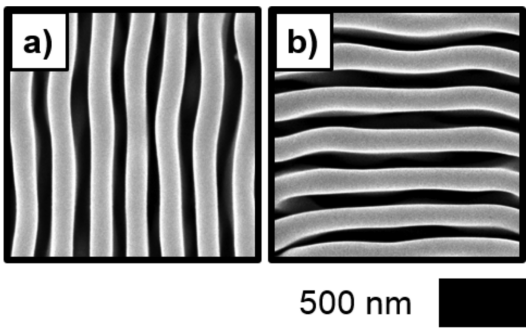

Figure 4.1: Effect of illumination source polarization on pattern orientation. SEMs representative of photoelectrodeposits generated with λ_{avg} = 630 nm illumination polarized (a) vertically and (b) horizontally.

Figure 4.1 presents representative scanning electron micrographs (SEMs) of Se-Te photoelectrodeposits that were generated by electrochemically reducing SeO_2 and TeO_2 potentiostatically while illuminating the electrode with a narrowband light-emitting diode (LED) having an intensity-weighted average wavelength (λ_{avg}) of 630 nm polarized vertically (a) and horizontally (b). In both cases, a highly anisotropic, lamellar-type morphology was observed. The long axes of the lamellar structures were oriented parallel to the polarization of the illumination; hence, vertical polarization resulted in vertically oriented lamellae whereas horizontal polarization yielded horizontally oriented lamellae. X-ray diffraction analysis has shown that Se-Te photoelectrodeposits generated in this manner are nanocrystalline with crystallites composed of a substitutional alloy of Se and Te in a hexagonal structure common to both elements in their pure phases.[74]

Figure 4.2a-c presents SEMs representative of photoelectrodeposits generated using two equal intensity LED sources with λ_{avg} = 630 nm. One source was polarized vertically and the polarization of the second source was offset clockwise from the vertical by θ_1 = 20° (a), 40° (b), or 60° (c). In each case, a lamellar pattern was

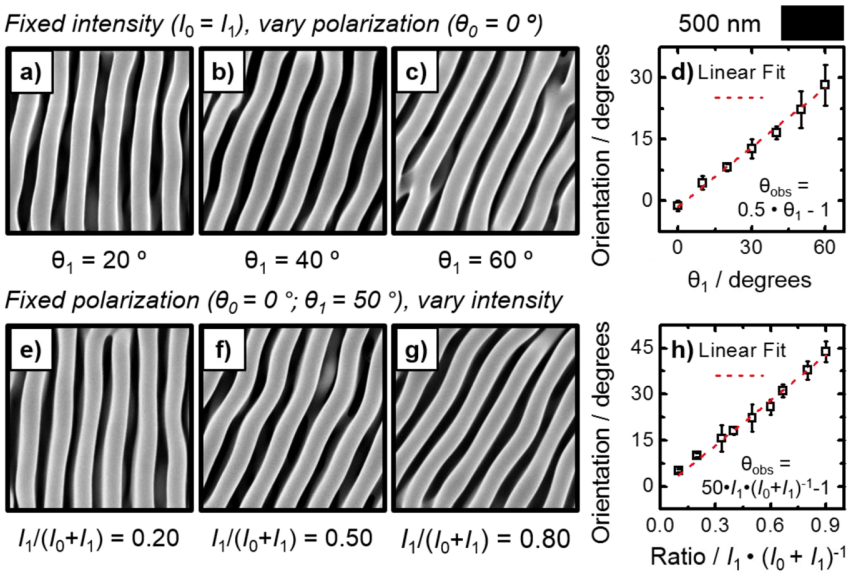

Figure 4.2: Pattern orientation in photoelectrodeposits generated using two same-wavelength (λ_{avg} = 630 nm) sources with differing linear polarizations. (a-c) SEMs representative of photoelectrodeposits generated using two sources with equal intensity, the first source polarized vertically ($\theta_0 = 0°$) and the second at the indicated rotation (θ_1) clockwise from the vertical. (d) Plot of the rotation of the orientation of the long axis of the pattern (θ_{obs}) measured clockwise from the vertical as a function of θ_1. (e-g) SEMs representative of photoelectrodeposits generated using two same-wavelength sources (λ_{avg} = 630 nm), each with a fixed linear polarization (first polarized vertically, the second offset $\theta_1 = 50°$ clockwise from the vertical) with the indicated fraction of the total intensity supplied by the second source [$I_1/(I_0 + I_1)$]. (h) Plot of θ_{obs} as a function of the fraction of the total intensity supplied by the second source.

observed that was similar to the pattern produced when only a single source was utilized. The long axis of the lamellar structures rotated clockwise away from the vertical in each case, and the magnitude of this rotation (θ_{obs}) increased with increasing values of θ_1. For $\theta_1 = 20°$, 40°, and 60°, values of θ_{obs} of 8 ± 1°, 17 ± 2°, and 28 ± 5°, respectively, were measured. Figure 4.2d presents a plot of the observed magnitude of the pattern rotation from the vertical (θ_{obs}) as a function of θ_1. The trend was well-fit by a line of the form $\theta_{obs} = 0.5\theta_1 - 1$. Figure 4.2e-g presents SEMs representative of photoelectrodeposits that were generated in a manner similar to those presented in Figure 4.2a. Here, θ_1 was fixed to a value of 50°, and the ratio of the intensity of this second source to the total intensity, [$I_1/(I_0 + I_1)$], was adjusted to 0.20 (e), 0.50 (f), and 0.80 (g), respectively. Again, the long axes of the lamellar structures were rotated clockwise away from the vertical in each case, and the magnitude of this rotation (θ_{obs}) increased with increasing values of

the quantity $I_1/(I_0 + I_1)$. For $I_1/(I_0 + I_1)$ = 0.20, 0.50, and 0.80, values of θ_{obs} of 10 ± 1°, 23 ± 5°, and 38 ± 3°, respectively, were observed. Figure 4.2h presents a plot of θ_{obs} as a function of the quantity $I_1/(I_0 + I_1)$. The trend was well-fit by a line of the form $\theta_{obs} = 0.5I_1/(I_0 + I_1) - 1$.

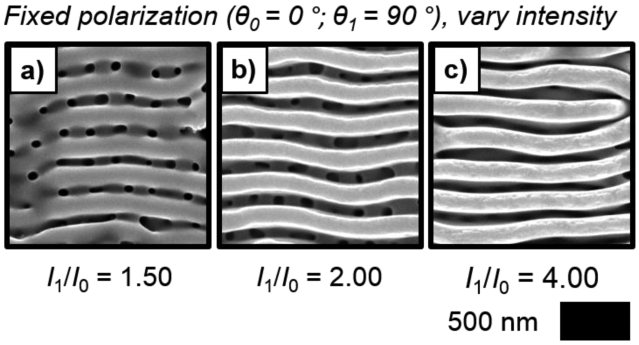

Figure 4.3: (a-c) SEMs representative of the photoelectrodeposits generated using two same-wavelength (λ_{avg} = 630 nm), orthogonally polarized sources (first polarized vertically, second horizontally) with the indicated intensity ratio between the horizontally and vertically polarized sources (I_1/I_0).

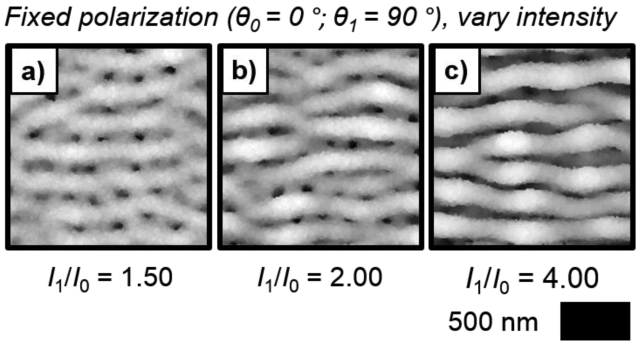

Figure 4.4: (a-c) Simulated morphologies of photoelectrodeposits generated using two same-wavelength (λ_{avg} = 630 nm), orthogonally polarized sources (first polarized vertically, second horizontally) with the indicated intensity ratio between the horizontally and vertically polarized sources (I_1/I_0).

Figure 4.3 presents SEMs representative of photoelectrodeposits that were generated using two LED sources with λ_{avg} = 630 nm, with one source polarized vertically with intensity I_0 and the other polarized horizontally with intensity I_1, wherein $I_0 \neq I_1$. The intensity ratio between the horizontally polarized source and the vertically polarized source (I_1/I_0) was 1.50 (a), 2.00 (b), and 4.00 (c). In (a), a square mesh morphology was observed in which a lamellar pattern was produced with the long axes of the lamellae running horizontally, superimposed over another similar

pattern in which the long axes of the lamellae ran vertically. The contrast in the SEM suggests that the vertically aligned lamellae were shorter (darker) than those running horizontally. The pattern in (b) is similar to that in (a), but the horizontally oriented lamellae appeared to increase in height relative to the lamellae that ran vertically. In (c), only horizontally running lamellae are visible, and the contrast in the SEM does not suggest the formation of any other structure.

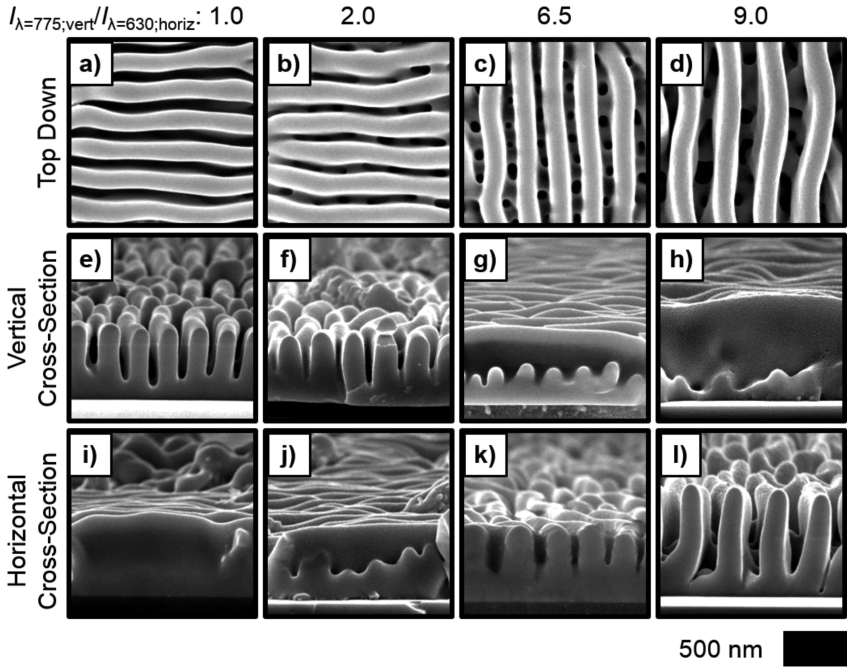

Figure 4.5: (a-d) Representative SEMs acquired in top down view of photoelectrodeposits generated using simultaneous illumination from a horizontally polarized λ_{avg} = 630 nm source and a vertically polarized λ_{avg} = 775 nm source with the indicated intensity ratio between the sources ($I_{\lambda=630;horiz}/I_{\lambda=780}$;vert). (e-h) Same as (a-d) but cleaved along the vertical axis (perpendicular to the polarization of the λ_{avg} = 630 nm illumination) and acquired in cross section. (i-l) Same as (a)-(d) but cleaved along the horizontal axis (perpendicular to the polarization of the λ_{avg} = 775 nm illumination) and acquired in cross section.

Figure 4.5a-d presents a series of top down SEMs that are representative of photoelectrodeposits generated using simultaneous illumination with a LED source with λ_{avg} = 775 nm polarized vertically and a LED source with λ_{avg} = 630 nm polarized horizontally, with intensity ratios between the two sources ($I_{\lambda=775;vert}/I_{\lambda=630;horiz}$) of 1.0 (a), 2.0 (b), 6.5 (c), and 9.0 (d), respectively. In (a), a lamellar structure was observed in which the long axes of the lamellae were oriented horizontally. The SEM in (b) is similar to that in (a) but displays a small amount of contrast in the spaces between the horizontally running lamellae. In (c), a lamellar structure in

which the long axes of the lamellae are oriented vertically is observed. This structure exhibited a larger periodicity than those in (a) and (b). Also, vertically periodic contrast was observed in the space between the lamellae, suggesting the presence of a second set of intersecting lamellae having long axes oriented along the horizontal direction. In (d), like (c), a lamellar structure in which the long axes of the lamellae were oriented vertically was observed, and again the periodicity of this structure was greater than that observed in (a) or (b). Some contrast is visible in the spaces between the vertically running lamellae, but unlike in (c) this contrast did not appear to be periodic. Figure 4.5e-h and i-l, respectively, present SEMs acquired from the same samples as in (a)-(d), but acquired in cross-sectional view by cleaving the substrate and film along the vertical (perpendicular to the polarization vector of the λ_{avg} = 630 nm illumination during growth), and along the horizontal (perpendicular to the polarization vector of the λ_{avg} = 775 nm illumination during growth), respectively. The cross sections in (e) and (f) depict horizontally oriented lamellae similar to those seen in (a) and (b) from a perspective looking down the lamellar axes. In (g), a shorter, less well-defined structure similar to those observed in (e) and (f) and with a similar periodicity was observed superimposed on a mostly featureless ridge that is the side of a vertically running lamella similar to those observed in the top down micrograph in (c). In (h), the micrograph reveals a ridge that is also the side of a vertically running lamella, as in (g). Some superimposed growth is again observed, with a varying height from left to right across the micrograph. In (i), the micrograph reveals a ridge that is the side of a horizontally running lamella similar to those presented in the top down micrograph in (a). In (j), a ridge similar to that observed in (i) is displayed. Superimposed on this ridge is growth with periodically varying height from left to right across the micrograph. The cross sections in (k) and (l) depict vertically oriented lamellae similar to those seen in (c) and (d), from a perspective looking down the lamellar axis.

4.2 Modeling of Pattern Formation Under Two Polarizations

Point dipole radiation sources were used to model the amplitude modulation of the electric field at the active film-solution interface during photoelectrochemical growth that was caused by the inherent surface roughness of the deposited film. The time-averaged field amplitude resulting from two coherent dipole sources was calculated using two-dimensional finite-difference time-domain (FDTD) simulations. Figure 4.6 presents the normalized time-average of the electric-field magnitude from two dipoles emitting radiation with a free-space wavelength of λ = 630 nm in a medium

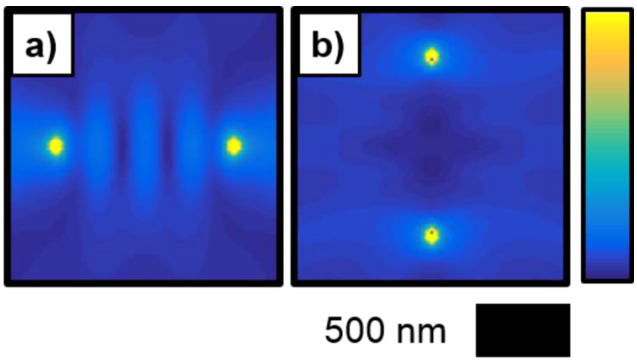

Figure 4.6: Normalized time-average of electric field magnitude from two dipoles emitting radiation with a free space wavelength of λ = 630 nm in a medium of index n = 1.33. Dipoles separated by a distance of two wavelengths in the direction (a) perpendicular and (b) parallel to the dipoles' oscillation axes.

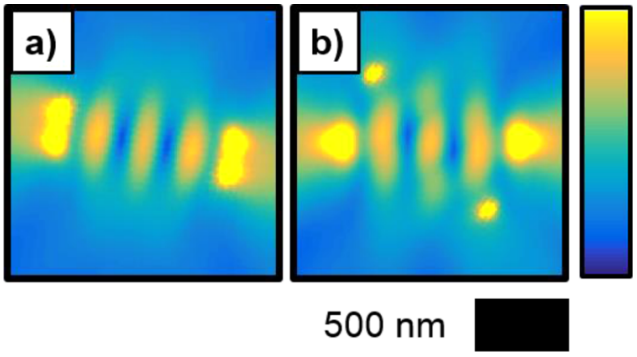

Figure 4.7: Normalized time-average of electric field magnitude resulting from two incoherently summed sets of dipole pairs each aligned perpendicular to a direction of oscillation. Dipoles are emitting radiation with a free space wavelength of λ = 630 nm in a medium of index n = 1.33. (a) One dipole set separated by two wavelengths along the horizontal axis and the axis of separation of the other set is rotated θ = 20° clockwise from the horizontal, both sets emit radiation with equal intensity. (b) One dipole set separated by two wavelengths along the horizontal axis and the axis of separation of the other set is rotated by θ = 50° clockwise from the horizontal, and the two sets emit radiation with relative intensity $I_{rotated}/(I_{rotated} + I_{horizontal}) = 0.2$.

of index n = 1.33 wherein the dipoles are separated by a distance of two wavelengths. In (a), the dipoles are separated perpendicular to the oscillation axis and from left to right three strong vertically running interference fringes are observed in the area between the dipoles. In (b), the dipoles are separated parallel to the oscillation axis, and constructive interference between the dipoles was not observed. Figure 4.7 presents simulations similar to those in Figure 4.6 but with two incoherently

summed sets of coherent dipole pairs each aligned perpendicular to a direction of oscillation. In (a), one dipole set is separated along the horizontal axis while the axis of separation of the other set is rotated θ = 20° clockwise from the horizontal, and both sets emit radiation with equal intensity. Interference fringes similar to those displayed in Figure 4.6a were observed but were rotated clockwise from the vertical by θ_{obs} = 10°. In (b), one dipole set is separated along the horizontal axis while the axis of separation of the other set is rotated θ = 50° clockwise from the horizontal, and the two sets emit radiation with a relative intensity $I_{rotated}/(I_{rotated} + I_{horizontal})$ = 0.2. Interference fringes similar to those in (a) were observed, and the most intense parts of the fringes were measured to be rotated clockwise from the vertical by θ_{obs} = 9°.

Computer modeling of the photoelectrochemical growth process was performed to analyze the morphologies expected for films generated as a result of the fundamental light-matter interactions during the deposition, using simultaneous illumination with two same-wavelength sources having different linear polarizations. A two-step, iterative model was utilized wherein electromagnetic simulations were first used to calculate local photocarrier generation rates at the electrode/solution interface. In the second step, electrochemical mass addition was simulated via a Monte Carlo method that utilized the local photocarrier generation rate to weight the local probabilities of mass addition (see Methods section for further details). The only empirical data used in the simulations were literature-derived estimates of the complex index of refraction, the charge-carrier concentrations, and the excited state lifetimes, of the electrodeposited Se-Te material, and the refractive index of the solution. During the early stages of deposition, dipole sources could be used to represent pointlike scattering features due to surface roughness of the deposit and help to visualize the periodic absorption profile that occurs between two scattering features along the growth front. However, at later times, these interfacial features evolved into anisotropic structures that had an extended spatial structure. Utilization of the modeling algorithm, which recalculated the scattering and absorption profile as the film morphology evolved, enabled the growth process to be fully reproduced. Although computationally expensive, the two step growth model both incorporated the absorption modulation resulting from surface roughness during the early stages of growth and also captured the dynamic feedback between light absorption and material growth which resulted in 3D structures that agreed with experiment.

The experiment described in Figure 4.2a-d was simulated, wherein two equal inten-

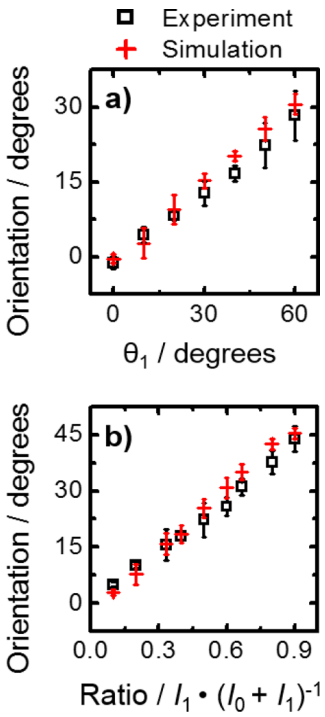

Figure 4.8: (a) Plot of the observed rotation of the orientation of the long-axis of the pattern (θ_{obs}) measured clockwise from the vertical as a function of the rotation of the polarization of one source (θ_1) in two-source illuminated photoelectrodepositions with same-wavelength (λ_{avg} = 630 nm), equal intensity sources when the other source was polarized vertically ($\theta_0 = 0°$). (b) Plot of θ_{obs} as a function of the fraction of the total intensity [$I_1/(I_0 + I_1)$] delivered by a source polarized linearly $\theta_1 = 50°$ clockwise from the vertical in two-source illuminated photoelectrodepositions with same-wavelength sources when the other source was polarized vertically. Data points corresponding to experimental results as well as results derived computationally from growth modeling are presented.

sity sources with $\lambda_{avg} = 630$ nm were utilized and one source was polarized vertically while the polarization of the second source was offset clockwise from the vertical by θ_1, and the observed rotation of the long-axis of the lamellar pattern clockwise away from the vertical (θ_{obs}) was derived. Figure 4.8a presents a plot of both the experimentally and computationally derived values of θ_{obs} as a function of θ_1. The experiment described in Figure 4.2e-h was also simulated, wherein the two sources with λ_{avg} = 630 nm were again utilized, with one source polarized vertically and the other at $\theta_1 = 50°$ from the vertical in the clockwise direction, while the fraction of the total intensity delivered by the second source [$I_1/(I_0 + I_1)$] was varied. Figure 4.8b presents a plot of both the experimentally and computationally derived values of θ_{obs} for this experiment as a function of [$I_1/(I_0 + I_1)$]. For both experiments,

the empirically and computationally derived values of θ_{obs} were in good agreement, and were linear functions of either θ_1 or [I_1/ (I_0 + I_1)].

Additionally, computer modeling of the growth process was also performed to simulate the morphologies expected for films generated using simultaneous illumination from two orthogonally polarized, same-wavelength sources with unequal intensities. The experiment described in Figure 4.3(a)-(c) was modeled (Figure 4.4), wherein two unequal intensity sources with λ_{avg} = 630 nm were utilized with one source polarized vertically and the other horizontally. The intensity ratio between the horizontally polarized source and the vertically polarized source (I_1/I_0) was 1.50 (a), 2.00 (b), and 4.00 (c). The simulated morphologies were in close accord with those observed experimentally (Figure 4.3), producing a square mesh morphology wherein the horizontally oriented lamellae were taller than those oriented vertically for I_1/I_0 = 1.50 and 2.00, and producing a single, horizontally oriented lamellar morphology for I_1/I_0 = 4.00.

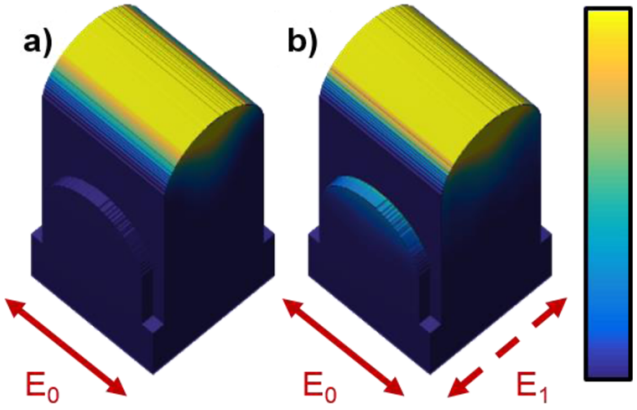

Figure 4.9: (a) Simulated power absorption of two idealized, orthogonal lamellae under a λ = 630 nm plane wave source polarized parallel to the taller feature (E_0). The width of each structure is typical of lamellar structures generated via photoelectrodeposition with λ_{avg} = 630 nm illumination, and the length of each lamella is typical of one period of such structures. (b) Same as (a) but with the addition of a second λ = 630 nm source with half the intensity of the first and polarized perpendicular to the taller feature (E_1) (sources assumed to be incoherent).

To further understand the growth of the morphologies that were observed when two orthogonally polarized sources of differing intensities and/or wavelengths were utilized, three sets of simulations of light absorption in idealized intersecting lamellar features were performed. First, films that had been experimentally photoelectrodeposited under vertically polarized λ_{avg} = 630 nm illumination alone and 775 nm

illumination alone were analyzed using SEM to derive the lamellar periods and widths of the resultant structures. These values were then used as the inputs for the lengths and widths of the idealized structures. Two idealized lamellae were oriented so as to intersect at a 90° angle and were assigned heights of 200 and 400 nm. In the first set of simulations, designed to help understand the growth of the morphologies that were observed when two orthogonally polarized sources with the same wavelength were used (λ_{avg} = 630 nm; Figure 4.3), the two lamellae both had widths that corresponded to the width of the lamellar structures observed for deposition with λ_{avg} = 630 nm illumination alone, and both had lengths equal to the corresponding lamellar period. Figure 4.9 presents the power absorption profile calculated (a) from a single λ = 630 nm plane wave source polarized parallel to the long axis of the taller lamella and (b) from two λ = 630 nm plane wave sources wherein one source was polarized parallel and the other perpendicular to the long axis of the taller lamella, with the source polarized perpendicular having half the intensity of the one polarized parallel. Figure 4.9a shows that significant absorption was observed only near the tip of the taller lamella. Figure 4.9b indicates that absorption was observed both at the tip of the taller lamella as well as at the tip of the shorter lamella.

The second and third sets of light absorption simulations were designed to help understand the generation of the morphologies observed when two orthogonally polarized sources with λ_{avg} = 630 nm and λ_{avg} = 775 nm were utilized simultaneously (Figure 4.5). In the second set of simulations, the taller lamellar feature had a width corresponding to the width of the lamellar structures observed for deposition with λ_{avg} = 630 nm illumination alone, and the length of the shorter lamella was equal to the corresponding lamellar period. The shorter lamellar feature had a width corresponding to the width of the lamellar structures observed for deposition with λ_{avg} = 775 nm illumination alone, and the length of the taller lamella was equal to the corresponding lamellar period. Figure 4.10a and b, respectively, present the power absorption profile calculated from a single λ = 630 nm plane-wave source polarized parallel to the long axis of the taller lamella alone, and from the same source as in (a) as well as a secondary λ = 775 nm plane-wave source polarized perpendicular to the long axis of the taller lamella that was twice as intense as the λ = 630 nm source. In Figure 4.10a, significant absorption was observed only near the tip of the taller lamella. In Figure 4.10b, absorption was observed both at the tip of the taller lamella as well as at the tip of the shorter lamella. The third set of simulations utilized lamellar structures having similar dimensions as the second set but with the

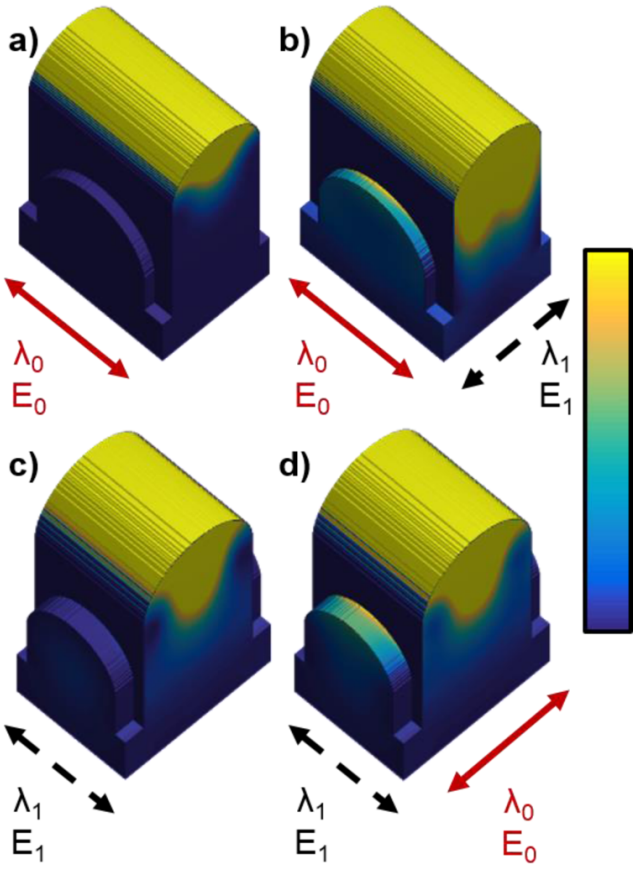

Figure 4.10: (a) Simulated power absorption of two idealized, orthogonal lamellae under a λ_0 = 630 nm plane wave source polarized parallel to the taller feature (E_0). The width of the taller structure is typical of lamellar structures generated via photoelectrodeposition with λ_{avg} = 630 nm illumination whereas the width of the shorter structure is typical of the structures generated with λ_{avg} = 775 nm illumination. (b) Same as (a) but with the addition of a λ_1 = 775 nm plane wave source 2 times more intense than the 630 nm source and polarized perpendicular to the taller feature (E_1) (sources assumed to be incoherent). (c) Simulated power absorption of two idealized, orthogonal lamellae under a λ_1 = 775 nm plane wave source polarized parallel to the taller feature (E_1). The width of the taller structure is typical of lamellar structures generated via photoelectrodeposition with λ_{avg} = 775 nm illumination whereas the width of the shorter structure is typical of the structures generated with λ_{avg} = 630 nm illumination. (d) Same as (c) but with the addition of a λ_0 = 630 nm plane wave source 6.5 times less intense than the 775 nm source and polarized perpendicular to the taller feature (E_0) (sources assumed to be incoherent).

heights of the two lamellae exchanged. Figure 4.10c and d, respectively, present the power absorption profile calculated from a single λ = 775 nm plane-wave source polarized parallel to the long axis of the taller lamella alone and from the same

source as in (c) as well as a secondary λ = 630 nm plane wave source polarized perpendicular to the long axis of the taller lamella that was 6.5 times less intense than the λ = 775 nm source. As with the second set of simulations (Figure 4.10a, b) in Figure 4.10c, significant absorption was observed only near the tip of the taller lamella, whereas in Figure 4.10d absorption was observed both at the tip of the taller lamella as well as at the tip of the shorter lamella.

4.3 Discussion

When two sources having the same wavelength (λ_{avg} = 630 nm) but having differing, linear, non-orthogonal polarizations were utilized simultaneously (Figure 4.2a-c and e-g), a lamellar pattern identical to those observed with only a single source (Figure 4.1) was observed, except for an in-plane rotation. This result can be readily understood because any linear polarization can be equivalently expressed as the sum of two orthogonal linear polarizations, for example, vertical and horizontal. Thus, no difference may be observed between the morphology generated if a single illumination source is utilized relative to the morphology generated if two sources are used simultaneously, as long as the intensity-weighted average of the polarization orientations of the two tandem sources is the same as the polarization of the single source. The experimental data quantitatively supports this hypothesis, because the observed orientation of the pattern (θ_{obs}) for the two-source experiments was almost exactly equal to the intensity-weighted average polarization orientation: $(I_0\theta_0 + I_1\theta_1)/(I_0 + I_1)$. For the experiment wherein the intensity of the sources was equal ($I_0 = I_1$), the first source was polarized vertically ($\theta_0 = 0°$) and the angle between the polarization vectors (θ_1) was varied, θ_{obs} would be expected to have the form $0.5\theta_1$. This expectation is very close to the experimentally observed relation of $\theta_{obs} = 0.5\theta_1$ - 1. Similarly, for the experiment in which the polarizations of the two sources were fixed ($\theta_0 = 0°$ and $\theta_1 = 50°$) and the relative contribution of the two sources to the total intensity was varied, θ_{obs} would be expected to have the form $50[I_1/(I_0 + I_1)]$, which again is very close to the experimentally observed relation of $\theta_{obs} = 50[I_1/(I_0 + I_1)]$ - 1. The difference between the expected and experimentally observed relations for θ_{obs}, a -1° offset, is likely a minor systematic error arising from a minor calibration error in a polarizer setting. This notion is supported by the facts that a value ofθ_{obs} =-1±1° was observed whenθ_0 =θ_1 =0°,and that the experimentally observed values of θ_{obs} were generally marginally lower than expected.

The quantitative agreement between the values of θ_{obs} measured in the experiments using same-wavelength (λ_{avg} = 630 nm) sources with mutually different linear, non-

orthogonal polarizations simultaneously, and in the analogous computer simulations (Figure 4.8), which utilized minimal empirical data, for all investigated conditions, suggests that the empirically observed behavior is the result of a fundamental optical phenomenon. This notion is supported by the results of the dipole scattering simulations (Figures 4.6 and 4.7). The interference fringes observed between two simulated radiation-emitting dipoles separated along the horizontal axis, and perpendicular to the oscillation axis (Figure 4.6a), are reminiscent of the lamellar morphology observed in the photoelectrodeposit generated with vertically polarized illumination (Figure 4.1a), and have been hypothesized to promote the initial growth of this periodic and anisotropic structure by providing the necessary spatially varying distribution of light intensity.[74] When two sets of dipoles were simulated with some angle, θ, between their axes of separation, the resultant interference fringes were observed to rotate by an angle, θ_{obs}, that is in good agreement with relation of $\theta_{obs} = \theta[I_{rotated}/ (I_{rotated} + I_{horizontal})]$. Thus, the dipole scattering simulations suggest that the orientation of the lamellar structures in the non-orthogonal, same-wavelength experiments is a manifestation of the elementary phenomenon of superposition of waves.

When two orthogonally polarized same-wavelength (λ_{avg} = 630 nm) sources that had unequal mutual intensities were utilized, the resultant structures appeared to consist of two intersecting sets of orthogonally oriented lamellae wherein the relative heights of each set of lamellae were directly proportional to the relative source intensities (Figure 4.3). These observations indicate that the utilization of orthogonally polarized sources can enable independent control over different features of the resultant film morphology, and thus comprises a potentially useful tool for generating application-specific structures. The reproduction of the experimental morphologies by the growth model (Figure 4.4) suggests that the generation of the intersecting structures when orthogonally polarized light is used is a result of the intrinsic light-matter interactions that occur during the deposition process. Moreover, the continued growth of such intersecting structures under the aforementioned conditions is consistent with the simulations of light absorption in the idealized versions of the structures (Figure 4.9) wherein illumination from two orthogonally polarized sources is preferentially absorbed in the tips of both structures. These areas represent the photoelectrochemical growth fronts: preferential light absorption in these areas supports continued anisotropic growth in a manner that preserves the cross sections of the features. Furthermore, visualization of the difference in the absorption profile with and without the contribution from the source parallel to the

shorter feature indicated that this source was solely responsible for absorption along the shorter feature.

Intersecting lamellar structures were also observed when two orthogonally polarized sources with differing wavelengths (λ_{avg} = 630 and 775 nm) were utilized. Again, the relative heights of each set of lamellae were proportional to the relative source intensities. However, for $I_{\lambda=775;vert}/I_{\lambda=630;horiz}$ = 1.0, SEM analysis provided little evidence for the presence of periodic, anisotropic structures with long axes oriented along the vertical, and, for $I_{\lambda=775;vert}/I_{\lambda=630;horiz}$ = 2.0, such structures were found to be shorter than the simultaneously observed, horizontally oriented structures. Also, for $I_{\lambda=775;vert}/I_{\lambda=630;horiz}$ = 6.5 and 9.0, structures with horizontal periodicity were observed. These observations are consistent with previous physical characterization suggesting lower rates of photoelectrodeposition may be observed when utilizing λ = 775 nm illumination than when utilizing λ = 630 nm illumination. The nanocrystalline nature of the photoelectrodeposited films suggests free carriers generated near the solution interface may contribute to the deposition of additional material in a disproportionally large manner as free carriers generated in the bulk have a greater probability of recombining before reaching the interface. The electromagnetic penetration depth of a material is inversely proportional to the imaginary component of its complex refractive index, κ. Spectroscopic ellipsometry measurements have shown that photoelectrodeposited Se-Te films exhibit monotonically decreasing values of κ with increasing values of λ for λ = 450 to 850 nm.[74] Thus, for lower values of λ, it is expected that more free carriers will be generated near the solution interface, correlating to a higher deposition rate.

Unlike the intersecting lamellar structures generated using two orthogonally polarized same-wavelength sources (λ_{avg} = 630 nm), when two orthogonally polarized sources with differing wavelengths (λ_{avg} = 630 and 775 nm) were used, the periodicities of the two sets of lamellae were unequal. The set with their long axes oriented parallel to the polarization vector of the λ_{avg} = 775 nm source displayed a greater periodicity than those oriented parallel to the polarization vector of the λ_{avg} = 630 nm source. This difference in periodicity is a consequence of differing anisotropic light absorption profiles in the growing structures in response to the different wavelengths which cause the lamellar period to increase monotonically with λ.[74] Moreover, these results indicate that not only is it possible to control the relative heights of structures with orthogonal periodicities, but also indicate that the magnitudes of those periodicities can also be controlled, which may be of use in the

construction of purpose-designed structures. Simulations in idealized versions of these intersecting structures were again consistent with their growth (Figure 4.10): illumination polarized along the long axis of a lamellar structure (of the same wavelength used to generate that structure) is preferentially absorbed in the tip of that structure relative to light polarized perpendicularly (of a different wavelength).

Dynamic photoelectrochemical growth may find potential in the generation of nanophotonic optical elements including planar lenses and mirrors,[91–93] polarization-sensitive filters and photodetectors,[39] and nanostructured scaffolds.[94, 95] The results described in this work have several implications for the use of this process to design application-targeted structures. First, controlling the pattern orientation with respect to the substrate does not require changing the polarization state of a single source, for example, rotating a linear polarizer. Instead, two sources could be used with static linear polarizations and the pattern orientation could be controlled by changing the relative intensity of the sources. Manipulating such a quantity continuously or in discrete steps over time could be used to generate morphological complexity. The utilization of orthogonal sources also presents another method to generate intricate structures wherein control of the feature size in three dimensions of two patterns may be obtained simultaneously and independently.

4.4 Conclusions

Nanopatterned Se-Te films were photoelectrochemically prepared using simultaneous illumination from two light sources with discrete linear polarizations. Films grown with two non-orthogonally polarized, same-wavelength sources displayed lamellar morphologies wherein the long axes of the structures were aligned along the intensity-weighted average polarization vector. Such behavior was consistent with simulations of light scattering at the solution-film interface at the onset of photoelectrochemical growth. Simulations of the growth with such illumination showed that the emergence of the observed morphologies could be understood by considering the fundamental light-matter interactions during deposition. Structures consisting of two sets of intersecting, orthogonal lamellae were generated when two orthogonally polarized illumination sources were utilized wherein the periodicity and feature size of each set of lamellae was proportional to the wavelengths of the illumination source polarized along their long axes. The evolution of such morphologies was consistent with simulations of light absorption in idealized intersecting lamellar structures, which indicated that the lamellae preferentially absorbed light polarized with the electric field vector parallel to their long axes. The cumu-

lative data suggests that under the conditions investigated, the morphology of the photoelectrodeposit is sensitive simultaneously to the polarization of both sources utilized during growth. Additionally, the use of such tailored optical excitation provides control over the pattern orientation and enables the generation of three-dimensional structures that cannot be produced with a single polarization.

4.5 Experimental Methods

Materials and Chemicals. $(CH_3)_2CO$ (ACS grade, BDH), CH_3OH (ACS grade, EMD), H_2SO_4 (ACS Reagent, J. T. Baker), HF (49%, Semiconductor grade, Puritan Products), In (99.999%, Alfa Aesar), Ga (99.999%, Alfa Aesar), SeO_2 (99.4%, Alfa Aesar), and TeO_2 (99+ % Sigma-Aldrich) were used as received. H_2O with a resistivity of $\geq$18.2 MΩ cm (Barnstead Nanopure System) was used throughout. n+-Si(111) (0.004-0.006 Ω cm, As-doped, 400 ± 15 μm, single-side polished, Addison Engineering) was used as a substrate for deposition. Flash-Dry Silver Paint (SPI Supplies), Double/Bubble Epoxy (Hardman), and nitrocellulose-based nail polish were used to assemble the Si working electrodes.

Electrode Preparation. One end of a Sn-coated Cu wire (22 AWG) was bent to form a small, flat coil and the wire was then threaded through glass tubing (6 mm O. D.) such that the coil was just outside the tubing. Epoxy was applied to seal the end of the tube from which the coil protruded. Square Si wafer sections (ca. 5 mm by 5 mm) were cut, and a eutectic mixture of Ga and In was scratched into the unpolished surfaces with a carbide scribe. The wire coil was then contacted to the unpolished surface and affixed with Ag paint. Nail polish was applied to insulate the unpolished face, the wire-coil contact, and the exposed wire between the coil and epoxy seal. Immediately before deposition, the Si surface of each electrode was clean sequentially with $(CH_3)_2CO$, CH_3OH and H_2O, and then the Si section of the electrode was immersed in a 49 wt % solution of HF(aq) for ~10 s to remove any SiO_x present at the surface of the Si. The electrode was then rinsed with H_2O and dried under a stream of N_2(g).

Photoelectrochemical Deposition. Photoelectrochemical deposition was performed using a Bio-Logic SP-200 potentiostat. Deposition was performed in a single-compartment glass cell with a pyrex window. A three-electrode configuration was utilized with a graphite-rod counter electrode (99.999%, Sigma-Aldrich) and a Ag/ AgCl reference electrode (3 M KCl, Bioanalytical Systems). Films were deposited from an aqueous solution of 0.0200 M SeO_2, 0.0100 M TeO_2, and 2.00

M H_2SO_4. Deposition was effected by biasing the illuminated n+-Si electrode potentiostatically at -0.40 V vs Ag/AgCl for 5.00 min at room temperature. After deposition, the electrode was immediately removed from the cell, rinsed with H_2O, and then dried under a stream of N_2(g). The Si substrate with a top-facing Se-Te film was mechanically separated from the rest of the electrode assembly. The nitrocellulose-based insulation, as well as the majority of the Ag paint and In-Ga eutectic, were then removed mechanically.

Electrode Illumination. The illumination utilized during photoelectrochemical deposition was provided by narrowband diode (LED) sources (Thorlabs) with respective intensity-weighted λ_{avg} values and spectral bandwidths (fwhm) of 630 and 18 nm (M625L2 or M625L3), and 775 and 31 nm (M780L2). The output of each diode source was collected and collimated with an aspheric condenser lens (Ø30 mm, f = 26.5 mm). For experiments involving simultaneous illumination with the two 630 nm sources, a polka dot beam splitter (Thor Laboratories BPD508-G) was utilized to combine the outputs. Both sources were incident upon the beamsplitter at an angle of 45° from the surface normal and thus generated coaxial output. For experiments involving simultaneous illumination with a 630 nm source and a 775 nm source, a dichroic filter (Edmund Optics #69-219) was utilized in the same geometry that was utilized for combining two same-wavelength sources with the beam splitter. A dichroic film polarizer (Thorlabs LPVISE2X2 or LPNIRE200-B) was placed between each source and the appropriate combining optic to enable independent control of the polarization of each source. The 775 nm source was used exclusively with the LPNIRE200-B polarizer. A 1500 grit ground-glass (N-BK7) diffuser was placed immediately in front of the photoelectrochemical cell to ensure spatial homogeneity of the illumination. The light intensity incident on the electrode was measured by placing a calibrated Si photodiode (Thorlabs FDS100) in place of an electrode assembly in the photoelectrochemical cell with electrolyte, and measuring the steady-state current response of that Si photodiode. Depositions utilizing a single diode with λ_{avg} = 630 nm or two such diodes simultaneously to provide illumination were performed with a total light intensity of 13.7 mW cm^{-2} at the electrode. Depositions utilizing the diodes with λ_{avg} = 630 and 775 nm in conjunction were performed with a total light intensity of 30.0 mW cm^{-2}.

Microscopy. SEMs were obtained with a FEI Nova NanoSEM 450 at an accelerating voltage of 5.00 kV with a working distance of 5 mm and an in-lens secondary electron detector. Micrographs obtained for quantitative analysis were acquired

with a resolution of 172 pixels μm^{-1} over ca. 120 μm^2 areas. Micrographs utilized to produce display figures were acquired with a resolution of 344 pixels μm^{-1} over ca. 8 μm^2 areas.

4.6 Modeling and Simulation Methods

Simulation of Film Morphology. The growths of the photo-electrochemically deposited films were simulated with an iterative growth model wherein electromagnetic simulations were first used to calculate the local photocarrier-generation rates at the film surface. Then, mass addition was simulated via a Monte Carlo method wherein the local photocarrier-generation rate weighted the local rate of mass addition along the film surface.

Growth simulations began with a bare, semi-infinite planar Si substrate. In the first step, the light-absorption profile under one or two linearly polarized, plane-wave illumination source(s) was calculated using full-wave finite-difference time-domain (FDTD) simulations with periodic boundary conditions along the substrate interface. In the second step, a Monte Carlo simulation was performed in which an amount of mass, equaling that of a 10 nm planar layer that covered the simulation area, was added to the upper surface of the structure with a probability F:

$$F(G) = \left[1 + G\left(n_0\tau_p + p_0\tau_n\right) + G^2\frac{\tau_p\tau_n}{n_i^2}\right]\prod_{i=1}^{3}\frac{x_i}{r_i} \tag{4.1}$$

where G is the spatially dependent photocarrier generation rate at the deposit-solution interface, n_i is the intrinsic carrier concentration, n_0 is the electron concentration, p_0 is the hole concentration, τn is the electron lifetime, τp is the hole lifetime, x_i is the fraction of i^{th} nearest neighbors occupied in the cubic lattice, and r_i is the distance to the i^{th} nearest neighbor. The product in the definition of this probability (Equation 4.1) serves to reduce the surface roughness of the film so as to mimic the experimentally observed surface roughness.

After the initial Monte Carlo simulation, the absorbance of the new, structured film was then calculated in the same manner as for the initial planar film, and an additional Monte Carlo simulation of mass addition was performed. This process of absorbance calculation and mass addition was repeated for a total of 30 iterations.

General Parameters for Computational Modeling. Se-Te films were assumed to be undoped (i.e. $n_0 = p_0 = n_i$) and a value of $n_i = 10^{10}$ cm^{-3} was used for the intrinsic carrier concentration.[62] A value of 1 μs was used for both the electron

and hole carrier lifetimes.[63] A value of n = 1.33 was used for the refractive index of the electrolyte regardless of wavelength.[75] Previously measured values of the complex index of refraction for Se-Te were utilized.[74] Illumination intensities identical to those used experimentally (see above) were used in the simulations. The electric field vector of the illumination was oriented parallel to the substrate. All FDTD simulations were performed using the "FDTD Solutions" software package (Lumerical).

Simulations of Dipole Emitters. The time-averaged field amplitude resulting from two coherent dipole sources was calculated using two-dimensional FDTD simulations. For simulations representing two illumination sources with different polarizations, the field amplitude profile was rotated about the simulation center and summed with the original field amplitude. A two-dimensional square simulation mesh with a lattice constant of 14 nm was used.

Simulated Absorption Profile of Idealized Intersecting Lamella. Three-dimensional FDTD simulations were used to calculate the normalized absorption profile of two intersecting idealized lamellar features. A three-dimensional cubic simulation mesh with a lattice constant of 2 nm was used. The idealized structure, from bottom to top, consisted of a semi-infinite Si substrate, a 100 nm conformal Se-Te layer, and two Se-Te lamellae with hemispherical upper boundaries. The lamellae were either 200 or 400 nm tall as indicated in the main text, as measured from the upper boundary of the conformal layer.

Chapter 5

EFFECTS OF RELATIVE PHASE AND MUTUAL COHERENCE

In this chapter, the morphologies of Se-Te photoelectrodeposits generated using two same-wavelength illumination sources were investigated with a series of discrete linear polarizations in tandem, either both mutually incoherent or mutually coherent with defined phase differences. In conjunction with the experiments, the morphologies of the resulting deposits were simulated by computational modeling of the light-material interactions intrinsic to the photoelectrochemical growth process. This collective assessment examines the capacity of the deposition process to generate unique morphologies in response to discrete net polarization states and thus to display sensitivity toward the coherency, phase difference, and polarization orientations of the optical inputs. Such further elaboration of the relationship between the illumination and resultant morphology enables the use of deliberately tailored excitation to effect the programmable growth of the deposited material. Additionally, the encoding of optical input polarization and relative phase in nonvolatile physical media is immediately relevant to advanced polarization holography. In this technique, data is written by using two polarized optical beams with arbitrary phase differences in summation to generate unique morphologies that are characteristic of the polarizations and relative phases of the writing beams. Polarization holography can provide significantly higher volumetric data storage capacity than conventional holography and thus is of potential interest for application in high density optical storage of digital data.[96–98]

5.1 Experimental Observations

Se-Te photoelectrodeposits were generated using illumination from a single light-emitting diode (LED) source that had an intensity-weighted average wavelength, λ_{avg}, of 630 nm and that was linearly polarized such that the E-field component was oriented at an angle θ = 45° clockwise from the vertical as indicated in the plot presented in Figure 5.1, panel a. Figure 5.1, panel b presents a representative top down scanning electron micrograph (SEM) of the deposit morphology, which reveals a highly anisotropic lamellar-type morphology wherein the long axes of the lamellae are oriented parallel to the direction of the E-field during growth.[50, 51, 74] Quantitatively, the long axes of the lamellae were oriented at 45 ± 3°

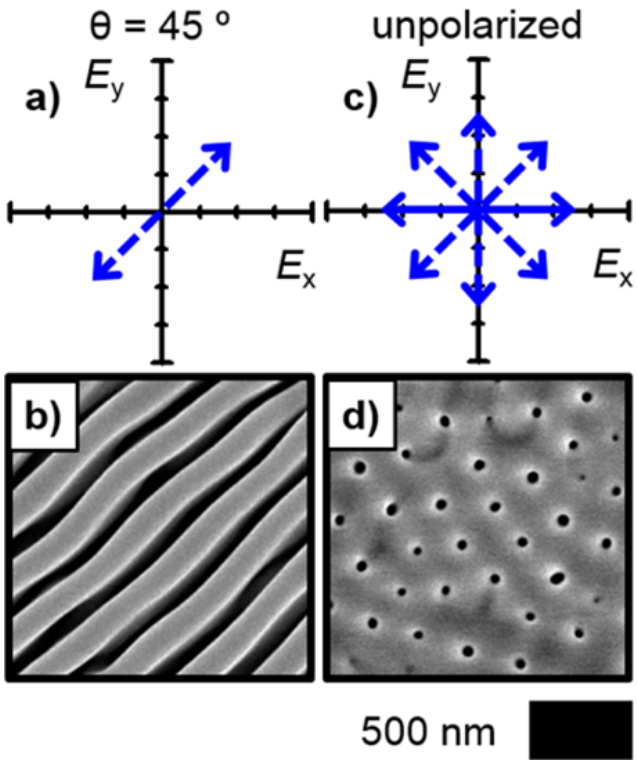

Figure 5.1: Effect of illumination source polarization on pattern anisotropy and orientation. (a) Plot of the E-field vector of a LED source with λ_{avg} = 630 nm linearly polarized 45° clockwise from the vertical, and (b) SEM representative of a photoelectrodeposit generated with this source. (c) Plot illustrative of the many E-field vectors characteristic of the same source as in panel (a) when unpolarized, and (d) SEM representative of a photoelectrodeposit generated with such source in the unpolarized state.

clockwise from the vertical (θ_{obs}). Figure 5.2, panel b presents a corresponding cross-sectional SEM and indicates an average film thickness of 450 nm. Deposits were also generated in the same manner as in Figure 5.1, panel b, but without the use of any polarizing optic, so that the illumination was unpolarized as indicated in the plot presented in Figure 5.1, panel c, and representative top down and cross-sectional SEMs are presented in Figure 5.1, panel d and Figure 5.2, panel d, respectively. The use of unpolarized light resulted in the generation of an ordered, isotropic mesh-type morphology that consisted of an array of nanopores. Thus, both linearly polarized and unpolarized illumination effect material patterning, but the asymmetry inherent in the linearly polarized illumination creates morphological anisotropy and directs the orientation of the lamellae in the photoelectrodeposit.

Subsequent deposits were generated by simultaneously using two incoherent LED

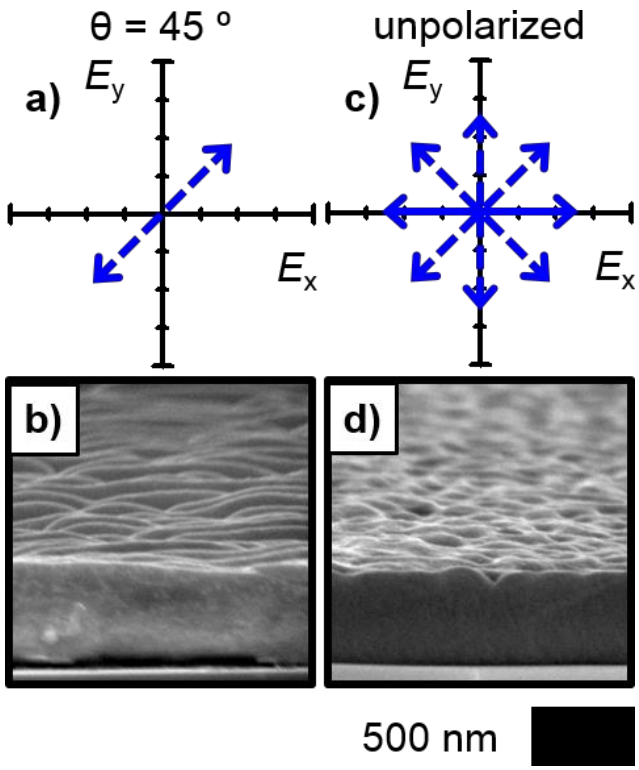

Figure 5.2: (a) Plot of the E-field vector of a LED source with λ_{avg} = 630 nm linearly polarized 45 ° clockwise from the vertical, and (b) cross-sectional SEM representative of a photoelectrodeposit generated with this source (cleaved parallel to the long axis of the anisotropic lamellar-type pattern). (c) Plot illustrative of the many E-field vectors characteristic of the same source as in panel a when unpolarized, and (d) cross-sectional SEM representative of a photoelectrodeposit generated with such a source in the unpolarized state.

sources that had λ_{avg} = 630 nm and equal intensities, with the first source polarized vertically (θ_0 = 0°) and the second source offset clockwise from the vertical by θ_1 = 60°, 70°, 80°, or 90°. The E-field vectors of each of the two tandem sources are plotted for each condition in Figure 5.3, panels a-d. Top down and cross-sectional SEMs representative of the resultant deposit morphologies are presented in Figure 5.3, panels e-h and Figure 5.4, panels e-h, respectively. With θ_1 = 60°, a lamellar-type morphology, similar to that generated with a single illumination source, was observed (Figure 5.3e) with a value of θ_{obs} = 27 ± 4°. This value agrees with the intensity-weighted average polarization orientation, 0.5 × θ_1 for the conditions here, or specifically 30° for the case of θ_1 = 60°, and is consistent with behavior observed previously for 0° < θ_1 < 60° [50]. Such agreement suggests that essentially identical morphologies should be generated using either a single

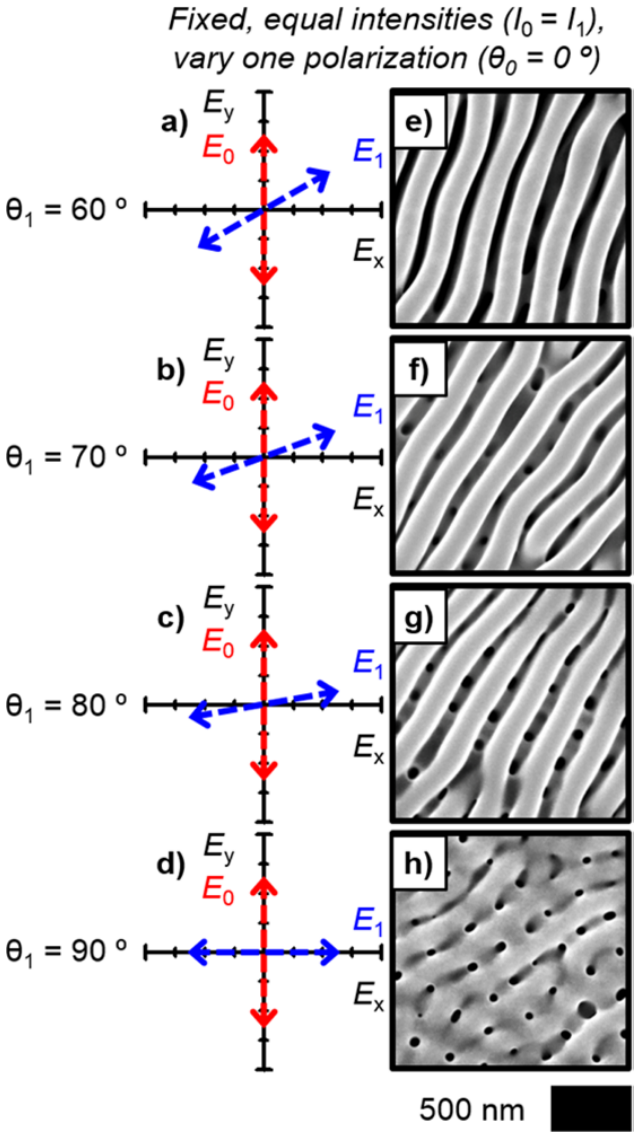

Figure 5.3: Two-source illumination polarization effect on photoelectrodeposit morphology for near-orthogonal and orthogonal polarizations. (a-d) Plots of the E-field vectors, E0 and E1, of two incoherent LED sources with λ_{avg} = 630 nm and equal intensity, the first source polarized vertically ($\theta_0 = 0°$) and the second at the indicated rotation (θ_1) clockwise from the vertical, and (e-h) SEMs representative of photoelectrodeposits generated using these sources.

linearly polarized source with orientation θ or two linearly polarized sources having an average polarization orientation θ. However, when the difference between the polarization orientations of the sources increased past $\theta_1 \approx 60°$, the morphologies observed for the use of two same-wavelength (630 nm) sources with equal intensities, but differing linear polarizations, were more complex than simple lamellar patterns

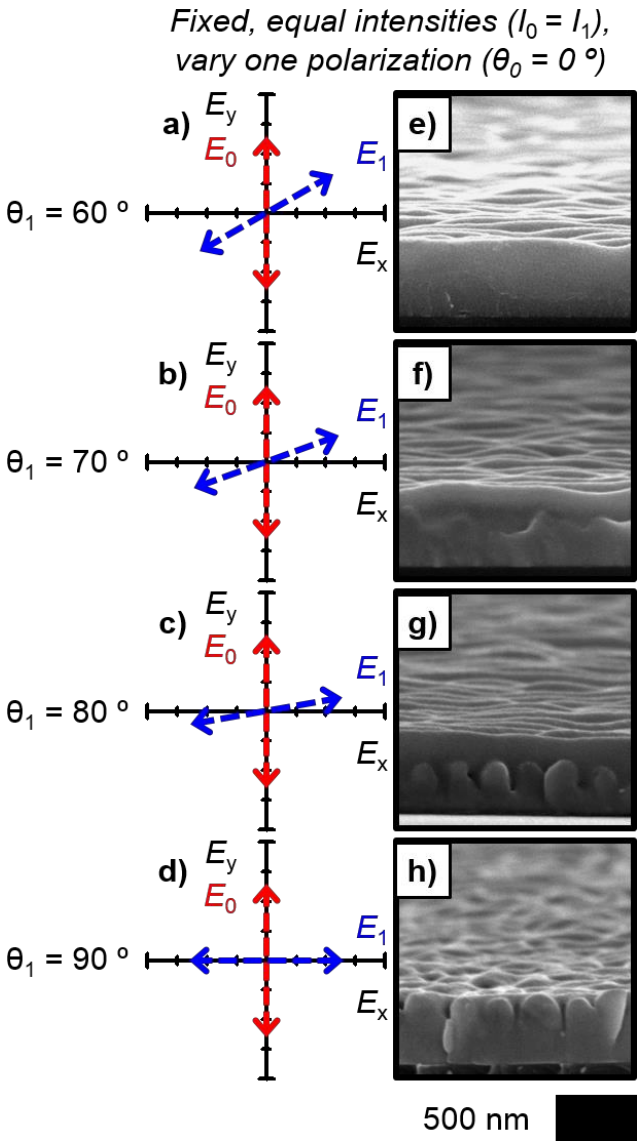

Figure 5.4: Two-source illumination polarization effect on photoelectrodeposit morphology for near-orthogonal and orthogonal polarizations. (a)-(d) Plots of the E-field vectors, E0 and E1, of two incoherent LED sources with λ_{avg} = 630 nm and equal intensity, the first source polarized vertically (θ_0 = 0 °) and the second at the indicated rotation (θ_1) clockwise from the vertical, and (e)-(h) cross-sectional SEMs representative of photoelectrodeposits generated using these sources (cleaved parallel to the long axis of the anisotropic lamellar-type pattern).

(Figure 5.3f-h). Beyond this limit, oriented lamellae were still observed, and, for θ_1 = 70°,80°,and90°,θ_{obs} =32±6°,38±5°,and46±8°, respectively. The behavior is thus consistent with expectations based on the average polarization orientation. However, as θ_1 was increased, a mesh-type pattern at a height lower than the

diagonal-running lamellae also became apparent (Figure 5.3f-h), and when $\theta_1 = 90°$ (Figure 5.3h), the height of this pattern approached the height of the lamellae. The cross-sectional micrographs (Figure 5.4f-h) directly depict the increase in height and definition of the mesh-type pattern relative to the lamellae with increasing values of θ_1. The morphology observed when $\theta_1 = 90°$ (Figure 5.3h) was not identical to that generated with a single source oriented at $\theta = 45°$ (Figure 5.1b), but rather it exhibited significantly less-defined anisotropy, resembling an average of the morphologies observed for the single source oriented at $\theta = 45°$ and for the unpolarized source (Figure 5.1d).

5.2 Modeling of Effects of Phase and Mutual Coherence

The appearance of the mesh-like component of the morphology, and the associated reduction of the uniaxial anisotropy, is consistent with the incoherent nature of the illumination sources utilized in these experiments. Computer modeling of the photoelectrochemical growth process was consequently performed to simulate the morphologies expected for films generated using simultaneous illumination with two coherent sources. In brief, a two-step, iterative model was utilized wherein electromagnetic simulations were first used to calculate local photocarrier-generation rates at the electrode/ solution interface. In the second step, electrochemical mass addition was simulated via a Monte Carlo method that utilized the interfacial photocarrier-generation rate to thereby weight the local probabilities of mass addition. The empirical data included in the simulations were limited to literature-derived estimates of the complex index of refraction, the charge-carrier concentrations, and the excited-state lifetimes of the electrodeposited Se-Te material. Thus, the computational results were principally defined by the fundamental light-matter interactions during deposition. Simulations similar to the experiments described in Figure 5.3 were performed, wherein two equal-intensity sources with $\lambda_{avg} = 630$ nm were utilized, with one source polarized vertically and the polarization of the second source offset clockwise from the vertical by θ_1. However, unlike the experiment wherein incoherent sources were utilized, the simulations considered coherent sources. Simulations were performed for phase angles (ϕ) of either 0° or 90° between the two coherent sources. Figure 5.5, panels a-d present simulations for $\theta_1 = 60°$, 70°, 80°, and 90°, respectively, for $\phi = 0°$. The E-field vectors of the considered sources were identical to those plotted in Figure 5.3, panels a-d. In each case, a lamellar pattern was observed, and the orientation of the lamellar long axes displayed increasing rotations from the vertical with increasing values of θ_1. Specifically, values of θ_{obs}

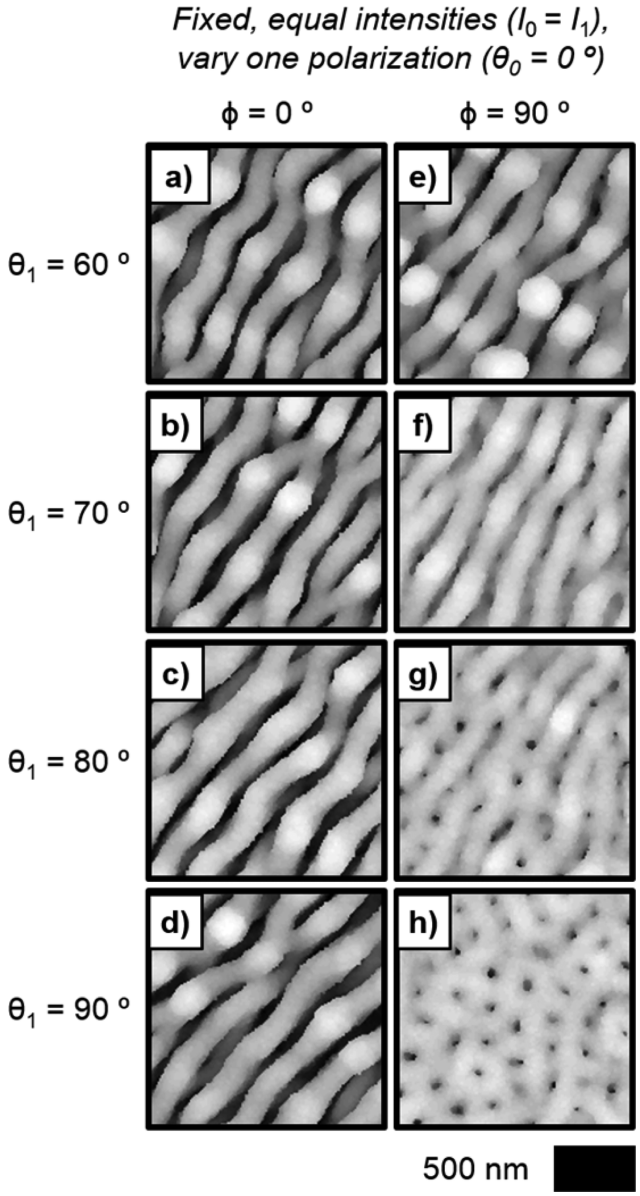

Figure 5.5: Three-dimensional simulations of photoelectrodeposit morphologies generated using two coherent λ = 630 nm wavelength sources with equal-intensity, the first source polarized vertically ($\theta_0 = 0°$) and the second at the indicated rotation (θ_1) clockwise from the vertical. Simulations are presented under two conditions: (a-d) one with a phase angle between the two coherent sources of ϕ = 0° (fully in-phase), and (e-h) with ϕ = 90° (fully out-of-phase). In both panels a-d and e-h, the E-field vectors of the two sources are as indicated in Figure 5.3, panels a-d, respectively.

of 33±3°, 36±2°, 40±2°, and45±1°were measured for θ_1 = 60°, 70°, 80°, and 90°, respectively. Figure 5.5, panels e-f present simulations analogous to those shown

in Figure 5.5, panels a-d, but for a phase angle of $\phi = 90°$. The E-field vectors of the sources were again identical to those presented in Figure 5.3, panels a-d. For $\theta_1 = 60°$ (Figure 5.5e), the simulated morphology was lamellar and qualitatively similar to that observed with $\phi = 0°$ (Figure 5.5a), whereas for $\theta_1 = 70°$ (Figure 5.5f), the simulated morphology also displayed an oriented, lamellar-type component but appeared to be superimposed upon a mesh-type pattern. When $\theta_1 = 80°$ (Figure 5.5g), the lamellar pattern was less well-defined and more similar in height to the mesh-type pattern, relative to the case of $\theta_1 = 70°$. Moreover, when $\theta_1 = 90°$ (Figure 5.5h), the morphology lacked any apparent anisotropy and orientation and was thus similar to the morphology observed experimentally for growth stimulated by a single, unpolarized, incoherent source (Figure 5.1d).

The simulated morphologies displayed in Figure 5.5, panels a-d showed that in the case of coherent sources with a phase difference of $\phi = 0°$, only lamellar morphologies were observed. The sum of the output of two completely in-phase, coherent, linearly polarized, same-wavelength sources cannot be differentiated from the output of a single coherent, linearly polarized source that has an equivalent net intensity and the same polarization orientation as the weighted average polarization orientation of the tandem sources. Consequently, the photoelectrodeposit morphology observed for the case of a single incoherent source polarized at $\theta = 45°$ (Figure 5.1b) was qualitatively matched by the simulated morphology for two equal intensity, in-phase ($\phi = 0°$) coherent sources polarized at $\theta_0 = 0°$ and $\theta_1 = 90°$ (Figure 5.5d), with both exhibiting equivalent values of θ_{obs}. In addition, when $\phi = 0°$, the measured values of θ_{obs} were equivalent to the intensity-weighted average polarization orientation, $0.5 \times \theta_1$. In contrast, the sum of the output of two coherent, linearly polarized, same-wavelength sources that are not completely in-phase ($\phi \neq 0°$) can be differentiated from the output of a single coherent, linearly polarized source with equivalent net intensity and the same polarization orientation as the weighted average polarization orientation of the tandem sources. In this case, the summing of the output of the tandem sources generates elliptically rather than linearly polarized illumination. The difference in the morphologies predicted by the simulations for growths with $\phi = 0°$ and $\phi = 90°$ suggests that the photoelectrodeposition process is capable of differentiating elliptically polarized from linearly polarized illumination. Thus, the resulting photoelectrodeposit physically encodes information concerning the relative phase of the illumination inputs.

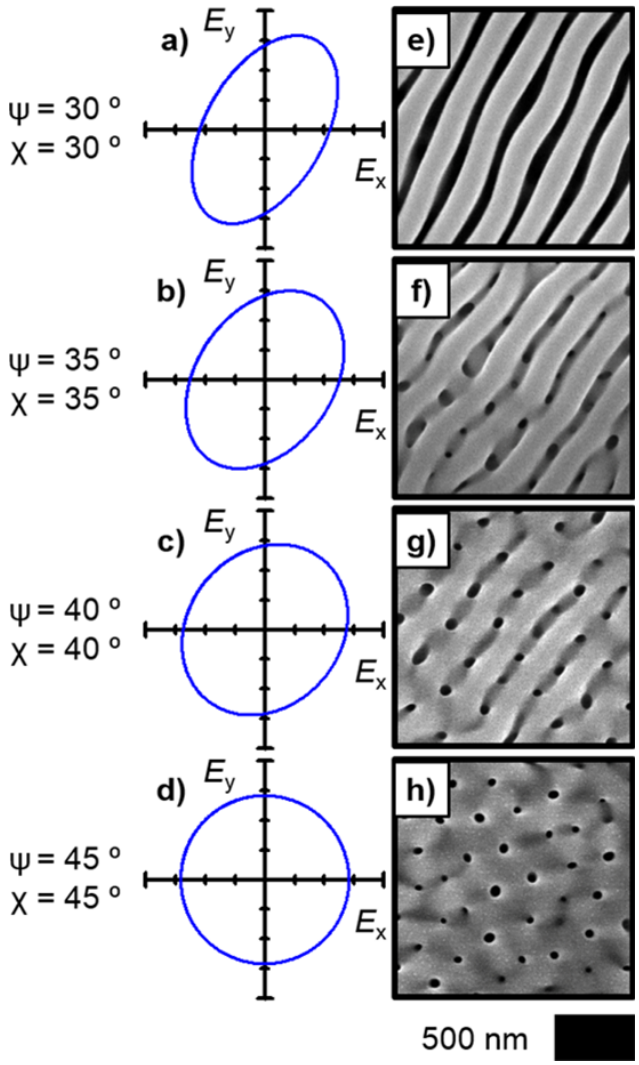

Figure 5.6: (a-d) Plots of the E-field vector traced over time at a fixed point for illumination provided by a HeNe laser λ_{avg} = 632.8 nm with defined elliptical polarizations. ψ indicates the orientation of the major axis of the ellipse measured clockwise from the vertical. χ represents the angle between the major axis and a line connecting a vertex on the major axis with one on the minor axis and relates the eccentricity and asymmetry of the ellipse. (e-h) SEMs representative of photoelectrodeposits generated with the elliptical illumination profiles indicated in panels a-d, respectively.

5.3 Further Experimental Observations and Comparison With Modeling

Figure 5.6, panels a-d present plots of the polarization ellipses that result from the out-of-phase addition (ϕ = 90°) of sources with E-field vectors the same as those plotted in Figure 5.3, panels a-d and thus describe the illumination utilized in the simulations presented in Figure 5.5, panels e-h. The orientation of the major axis

of the ellipse, measured clockwise from the vertical, is denoted as ψ. The angle between the major axis of the ellipse and a line connecting a vertex on the major axis with one on the minor axis, denoted as χ, quantifies the asymmetry, or eccentricity, of the ellipse. For the conditions investigated in the simulations presented in Figure 5.5, panels e-h, $\psi = \chi = 0.5 \times \theta_1$. By using these same elliptical polarizations, deposits were generated experimentally (with HeNe laser illumination with λ_{avg} = 632.8 nm) to corroborate the conclusions from the simulations that the photoelectrochemical growth process can discriminate between linearly and elliptically polarized illumination and thus responds to phase data contained in the incident illumination. The growth modeling indicated that this phenomenon manifests itself in the degree of nanoscale pattern anisotropy and is potentially an effect of variable anisotropy in the illumination polarization. The addition of out-of-phase orthogonal polarization components results in the generation of an elliptical polarization state, and increasing amounts of such components decrease the asymmetry of the relevant polarization ellipse (quantified by χ). The simulations predict that as this asymmetry is reduced beyond a threshold ($\chi > 30°$), the observable morphological patterning begins to transition from anisotropic to isotropic, and, in the limiting case of circular polarization ($\chi = 45°$), the patterning becomes completely isotropic.

Figure 5.6, panels e-h present SEMs of the deposits that were generated utilizing the elliptical polarizations corresponding to those presented in Figure 5.6, panels a-d. Corresponding cross-sectional SEMs are presented in Figure 5.8, panels e-h. Deposition with elliptical polarization with $\chi = 30°$ (Figure 5.6e) resulted in the generation of lamellar structures with highly uniaxial anisotropy, as in the case of linear polarization (Figure 5.1b; $\chi = 0°$ equivalent). For $\chi = 35°$ (Figure 5.6f), the overall morphological anisotropy was reduced compared to the case for χ = 30°, and an isotropic mesh-type pattern was observed underlying the anisotropic lamellar pattern. For $\chi = 40°$ (Figure 5.6g), this mesh-type morphology became more prominent, with a height approaching that of the anisotropic pattern. For χ = 45° (Figure 5.6g), no anisotropic pattern was observed; rather, the morphology was highly similar to that produced by a single unpolarized incoherent source (Figure 5.1d). Thus, the experimental morphologies presented in Figure 5.6, panels e-h matched those predicted by the growth model (Figure 5.5e-h). Such collective agreement demonstrates the capacity of the deposition to produce unique morphologies in response to elliptically polarized illumination and thus to store relative phase information. Specifically, superimposed isotropic mesh-type patterns and anisotropic lamellar-type patterns are generated wherein the weighting between the two types of

patterns is correlated with the phase difference between the orthogonal polarization components of the optical field (and thus the resultant ellipticity of the output).

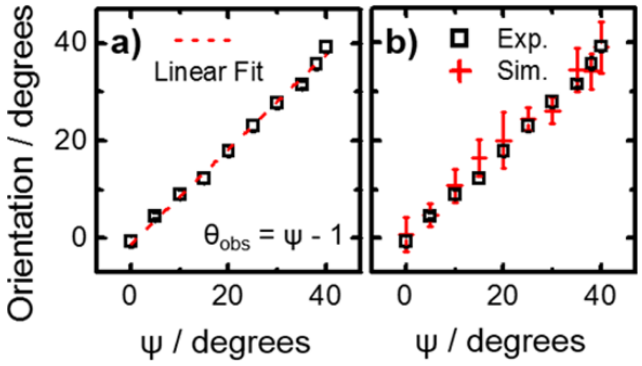

Figure 5.7: (a) Plot of the rotation of the orientation of the long axis of the pattern (θ_{obs}) measured clockwise from the vertical as a function of ψ for photoelectrodeposits generated with elliptically polarized illumination. Error bars generally smaller than displayed symbols. (b) Same as panel a but with addition of values derived computationally from growth modeling.

Auxiliary information regarding the polarization state of the incident illumination is also inherent in the lamellar-type pattern because the pattern anisotropy is associated with an orientation. To characterize the relation between an elliptical polarization and the encoded orientation, additional deposits were generated experimentally using polarizations having $0° \leq \psi \leq 25°$ and $\chi = \psi$. Figure 5.7, panel a presents values of θ_{obs} for $0° \leq \psi \leq 40°$ (wherein $\chi = \psi$) as a function of ψ. The trend is well-fit by a line of the form $\theta = \psi$ - 1. Additional growth obs modeling was performed to generate simulated morphologies for all of the experimentally investigated elliptical polarizations. Figure 5.7, panel b plots the values of θ_{obs} derived from these simulations as a function of ψ, along with the corresponding experimental observations. Quantitative agreement was observed between the simulation and experiment. The near equivalence between θ_{obs} and ψ indicates that the directional component of the anisotropy of an elliptical polarization state is directly recorded in the deposit morphology. Moreover, this anisotropy is discernible not only when the polarization is defined by a highly asymmetric ellipse (small values of χ, approximating linear polarization), but also when the polarization is defined by a near-circular ellipse, for example, $\chi = 40°$ (Figure 5.6h). This behavior indicates that when the illumination used in the deposition process is supplied by tandem sources, the lamellar component of the morphology arises from the in-phase addition of orthogonal polarization components, whereas the mesh component arises from out-of-phase addition. This

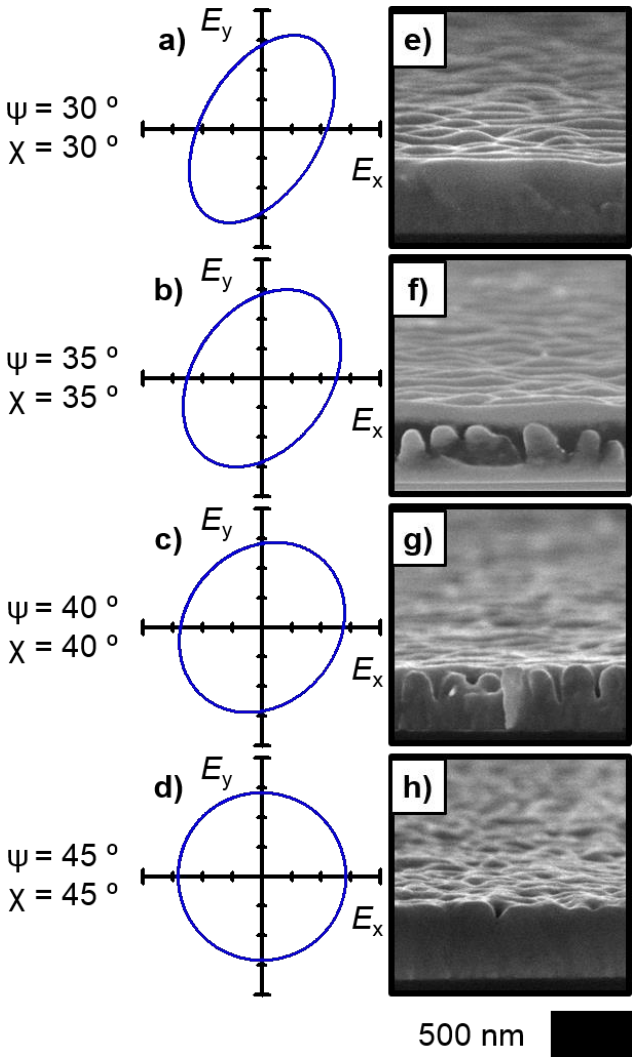

Figure 5.8: (a)-(d) Plots of the E-field vector traced over time at a fixed point for illumination provided by a HeNe laser λ_{avg} = 632.8 nm with defined elliptical polarizations. ψ indicates the orientation of the major axis of the ellipse measured clockwise from the vertical. χ represents the angle between the major axis and a line connecting a vertex on the major axis with one on the minor axis and relates the eccentricity and asymmetry of the ellipse. (e)-(h) Cross-sectional SEMs representative of photoelectrodeposits generated with the elliptical illumination profiles indicated in panels a-d respectively (cleaved parallel to the long axis of the anisotropic lamellar-type pattern for (e)-(g)).

behavior and rationale also are consistent with the observations of the morphologies generated using two near-orthogonal or orthogonal equal intensity incoherent sources (Figure 5.3). As observed for the analogous simulations (Figure 5.5e-h) and experiments (Figure 5.6e-h) with coherent sources with $\phi = 90°$, only a lamellar-type morphology was observed for $\theta_1 = 60°$ ($\theta_0 = 0°$), whereas a lamellar-type morphol-

ogy superimposed on a mesh-type was observed for $\theta_1 = 70°$ and 80°. In each case, the lamellar morphology was oriented along the intensity-weighted average polarization orientation. However, in contrast to deposits generated using coherent sources with $\phi = 90°$, the lamellar morphologies were more prominent for $\theta_1 = 70°$ and 80°, and for $\theta_1 = 90°$, some anisotropy was still observed. This behavior results from the presence of in-phase addition in complement to the out-of-phase addition solely present in the coherent with $\phi = 90°$, as the summing of the incoherent sources involves many additions with a continuous range of phase angles ($0° \leq \phi \leq 90°$), in contrast to the coherent case for which ϕ was fixed at 90°. Similarly, the absence of a discernible mesh-type morphological component in the incoherent case with $\theta_1 = 60°$ is consistent with an insufficient amount of out-of-phase addition of orthogonal polarization components.

5.4 Conclusions

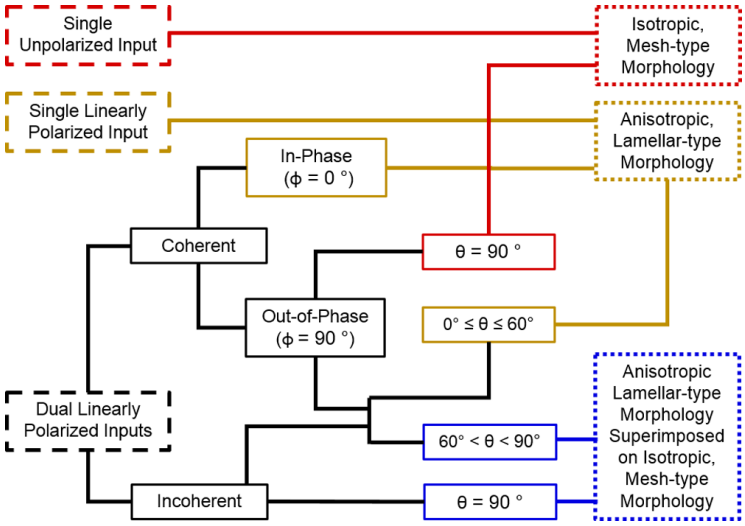

Figure 5.9: Flowchart detailing expected morphology of the photoelectrodeposit as a function of the polarization characteristics of the optical inputs. θ represents the angle between the polarization vectors of two linearly polarized inputs, and ϕ represents the phase angle between two coherent inputs. Simultaneous inputs are assumed to be of equal intensity. Anisotropic morphologies orient with long axes parallel to the average polarization vector of the input(s).

Figure 5.9 presents a flowchart that outlines the expected morphology of the photoelectrodeposit as a function of the polarization characteristics of the optical inputs. In summary, photoelectrodeposition using a single, linearly polarized source resulted in the generation of a highly anisotropic, lamellar-type morphology, whereas the use of an unpolarized source resulted in the generation of an isotropic, mesh-type

morphology. The use of tandem simultaneous same-wavelength, linearly polarized, coherent and in-phase sources also resulted in the generation of lamellar-type structures because such illumination is equivalent to that produced by a single linearly polarized coherent source. Summing two linearly polarized, coherent sources that are not completely in-phase results in elliptically polarized illumination. The use of such illumination generated a spectrum of related morphologies that were dependent on the ellipticity, which correlates with the amount of out-of-phase addition between orthogonally polarized components of the optical inputs. For sufficiently low degrees of ellipticity ($\chi \leq 30°$), lamellar morphologies that appear equivalent to those generated using a single linearly polarized source were observed. For greater degrees of ellipticity, lamellar-type patterns were superimposed on a mesh-type pattern that was similar to the pattern observed when unpolarized illumination was used. Relative to the lamellar-type pattern, the mesh-type pattern increased in height and definition as the degree of the polarization ellipticity increased. Only the mesh-type pattern was observed in the limiting case of circular polarization (χ = 45°). The results of deposition using two linearly polarized, incoherent sources were consistent with those observed for the use of two coherent sources that were not completely in-phase in that anisotropic, lamellar-type morphologies transitioned to isotropic, mesh-type morphologies as the amount of out-of-phase addition increased between the orthogonally polarized components of the light sources. When tandem sources were used and lamellar-type morphologies were generated, the long axis of the lamellar pattern always aligned parallel to the intensity-weighted average polarization orientation. The observed morphologies consistently matched those simulated by computational modeling, indicating that the specific morphology was fully determined by each set of defined optical inputs. Thus, the collective experimental and computational modeling data indicate that the photoelectrochemical growth process is sensitive to the coherency, relative phase, and polarization orientations of the utilized illumination inputs and that the resulting morphology expresses these inputs in a distinctive pattern in each case.

5.5 Experimental Methods

Materials and Chemicals $(CH_3)_2CO$ (ACS Grade, BDH), H_2SO_4 (ACS Reagent, J. T. Baker), HF (49 %, Semiconductor Grade, Puritan Products), In (99.999 %, Alfa Aesar), Ga (99.999 %, Alfa Aesar), SeO_2 (99.4 %, Alfa Aesar), and TeO_2 (99+ %, Sigma-Aldrich) were used as received. H_2O with a resistivity $\geq$ 18.2 MΩ cm (Barnstead Nanopure System) was used throughout. n+-Si(111) (0.004 – 0.006 Ω

cm, As-doped, 400 ± 15 μm, single-side polished, Addison Engineering) was used as a substrate for deposition. Flash-Dry Silver Paint (SPI Supplies), Double/Bubble Epoxy (Hardman) and nitrocellulose-based nail polish were used to assemble the Si working electrodes.

Electrode Preparation One end of a Sn-coated Cu wire (22 AWG) was bent to form a small, flat coil and the wire was then threaded through glass tubing (6 mm O. D.) such that the coil was just outside the tubing. Epoxy was applied to seal the end of the tube from which the coil protruded. Square Si wafer sections (ca. 5 mm by 5 mm) were cut and a eutectic mixture of Ga and In was scratched into the unpolished surfaces with a carbide-tipped scribe. The wire coil was then contacted to the unpolished surface and affixed with Ag paint. Nail polish was applied to insulate the unpolished face, the wire-coil contact, and the exposed wire between the coil and epoxy seal. Immediately before deposition, the Si surface of each electrode was cleaned with $(CH_3)_2CO$, and then the Si section of the electrode was immersed in a 49 wt. % solution of HF(aq) for 10 s to remove any surficial SiO_x from the Si. The electrode was then rinsed with H_2O and dried under a stream of N_2(g).

Electrode Illumination Illumination for the photoelectrochemical depositions was provided by narrowband diode (LED) sources with an intensity-weighted λ_{avg} value of 630 nm and a spectral bandwidth (FWHM) of 18 nm (Thorlabs M625L2 and M625L3). The output of each diode source was collected and collimated with an aspheric condenser lens (Ø30 mm, f = 26.5 mm). For experiments involving simultaneous illumination with two LED sources, a polka dot beam splitter (Thorlabs BPD508-G) was utilized to combine the outputs. Both sources were incident upon the beam splitter at an angle of 45 ° from the surface normal, and thus generated coaxial output. A dichroic film polarizer (Thorlabs LPVISE2X2 or LPNIRE200-B) was placed between each source and the beam splitter to enable independent control of the polarization of each source. A 1500 grit ground-glass (N-BK7) diffuser was placed immediately in front of the photoelectrochemical cell to ensure spatial homogeneity of the illumination.

Additionally, a HeNe laser (Aerotech LSR5P) emitting at 632.8 nm in a TEM00 mode with linear polarization was also used an illumination source. The HeNe laser was fitted with a 10x beam expander (Melles-Griot) to create a spot that overfilled the working electrode. The output from the HeNe laser was directed at normal incidence through a zero-order λ/4 plate (Thorlabs WPQ10E-633). The λ/4 plate was rotated about the optical axis such that the fast axis of the plate was oriented

at angles between 0 and 45° clockwise from the polarization axis of the laser. The presence of the $\lambda/4$ plate generated a ϕ = 90° phase angle between the orthogonal components of the laser illumination and provided for the generation of defined elliptical polarizations.

The light intensity incident on the electrode was measured by placing a calibrated Si photodiode (Thorlabs FDS100) instead of an electrode assembly in the photoelectrochemical cell with electrolyte, and the steady-state current response of that Si photodiode was measured. All depositions were performed with an intensity of 13.7 mW cm^{-2} at the electrode.

Photoelectrochemical Deposition Photoelectrochemical deposition was performed using a Bio-Logic SP-200 potentiostat. Deposition was performed in a single-compartment glass cell with a pyrex window. A three-electrode configuration was utilized with a graphite-rod counter electrode (99.999 %, Sigma-Aldrich) and a Ag/AgCl reference electrode (3 M KCl, Bioanalytical Systems). Films were deposited from an aqueous solution of 0.0200 M SeO_2, 0.0100 M TeO_2, and 2.00 M H_2SO_4. Deposition was effected by biasing the n+-Si electrode, illuminated as detailed under the above subheading (Electrode Illumination), potentiostatically at -0.40 V vs. Ag/AgCl for 5.00 min at room temperature. After deposition, the electrode was immediately removed from the cell, rinsed with H_2O, and then dried under a stream of N_2(g). The Si substrate with top-facing Se-Te film was mechanically separated from the rest of the electrode assembly. The nitrocellulose-based insulation and the majority of the Ag paint and In-Ga eutectic were then removed mechanically.

Microscopy Scanning electron micrographs (SEMs) were obtained with a FEI Nova NanoSEM 450 at an accelerating voltage of 5.00 kV with a working distance of 5 mm and an in-lens secondary electron detector. Micrographs obtained for quantitative analysis were acquired with a resolution of 172 pixels μm-1 over ca. 120 μm2 areas. Micrographs utilized to produce display figures were acquired with a resolution of 344 pixels μm-1 over ca. 8 μm2 areas.

Energy-dispersive X-ray Spectroscopy Energy dispersive X-ray spectroscopy (EDS) was performed in a Zeiss 1550VP SEM with an accelerating voltage of 15.00 kV and a working distance of 12 mm. An Oxford Instruments X-Max silicon drift detector was utilized. Spectra were collected in the range of 0 to 10 keV, and quantitative film compositions were derived from these spectra using the “INCA” software package (Oxford Instruments).

Raman Spectroscopy Raman spectra were collected with a Renishaw inVia Raman microprobe equipped with a Leica DM 2500 M microscope, a Leica N Plan 50x objective (numerical aperture = 0.75), a 1800 lines mm-1 grating, and a CCD detector configured in a 180° backscatter geometry. A 532 nm diode-pumped solid-state (DPSS) laser (Renishaw RL532C50) was used as the excitation source and a 10 μW radiant flux was incident on the surface of the sample. A line focus lens was utilized to transform the circular incident beam in one dimension to generate a ca. 50 μm line at the sample. A $\lambda/4$ plate was used to circularly polarize the incident excitation. No polarizing collection optic was used.

5.6 Modeling and Simulation Methods

Simulation of Film Morphology The growths of the photoelectrochemically deposited films were simulated with an iterative growth model wherein electromagnetic simulations were first used to calculate the local photocarrier-generation rates at the film surface. Then, mass addition was simulated via a Monte Carlo method wherein the local photocarrier-generation rate weighted the local rate of mass addition along the film surface.

Growth simulations began with a bare, semi-infinite planar Si substrate. In the first step, the light-absorption profile under a linearly polarized, plane-wave illumination source was calculated using full-wave finite-difference time-domain (FDTD) simulations with periodic boundary conditions along the substrate interface. In the second step, a Monte Carlo simulation was performed in which an amount of mass, equaling that of a 15 nm planar layer covering the simulation area, was added to the upper surface of the structure with a probability F:

$$F(G) = \left[1 + G\left(n_0\tau_p + p_0\tau_n\right) + G^2\frac{\tau_p\tau_n}{n_i^2}\right]\prod_{i=1}^{3}\frac{x_i}{r_i} \tag{5.1}$$

where G is the spatially dependent photocarrier-generation rate at the deposit/solution interface, n_i is the intrinsic carrier concentration, n_0 is the electron concentration, p_0 is the hole concentration, τn is the electron lifetime, τp is the hole lifetime, xi is the fraction of i^{th} nearest neighbors occupied in the cubic lattice, and r_i is the distance to the i^{th} nearest neighbor. The multiplicative sum in the definition of this probability (Equation 5.1) serves to reduce the surface roughness of the film so as to mimic the experimentally observed surface roughness.

After the initial Monte Carlo simulation, the absorbance of the new, structured

film was then calculated in the same manner as for the initial planar film, and an additional Monte Carlo simulation of mass addition was performed. This process of absorbance calculation and mass addition was repeated for a total of 20 iterations.

General Parameters Se–Te films were assumed to be undoped (i.e. $n_0 = p_0 = n_i$) and a value of $n_i = 10^{10}$ cm^{-3} was used for the intrinsic carrier concentration.[62] A value of 1 μs was used for both the electron and hole lifetimes.[63] Previously measured values of the complex index of refraction for Se-Te were utilized.[74] A value of n = 1.33 was used as the refractive index of the electrolyte, regardless of wavelength.[75] Illumination intensities identical to those used experimentally were used in the simulations. Simulations of the film morphology utilized the peak intensity wavelength of the experimental sources described in Section 5.5. The electric field vector of the illumination was oriented parallel to the substrate. A two-dimensional square mesh with a lattice constant of 1 nm was used for the simulations. All FDTD simulations were performed using the "FDTD Solutions" software package (Lumerical).

5.7 Elemental Composition Analysis of Photoelectrodeposits

The elemental composition of all of the photoelectrodeposits was analyzed using energy- dispersive X-ray spectroscopy (EDS). All analyzed films were found to be wholly composed of Se and Te. Photoelectrodeposits generated using a single incoherent LED source with λ_{avg} = 633 nm were found to on average have compositions of 56 atomic % Se (remainder Te) both when the illumination was polarized and when the illumination was unpolarized. Figure 5.10 presents a plot of the elemental composition (in terms of atomic % Se) of the photoelectrodeposits generated by simultaneously using two incoherent LED sources that had λ_{avg} = 630 nm and equal intensities, with the first source polarized vertically ($\theta_0 = 0°$) and the second source offset clockwise from the vertical by θ_1, as a function of θ_1. Figure 5.11 presents analogous data pertaining to the photoelectrodeposits generated using a HeNe laser with λ_{avg} = 632.8 nm with defined elliptical polarizations wherein $\psi = \chi$, as a function of ψ. In all cases, the average compositions of the photoelectrodeposits were found to range between 53 and 56 atomic % Se.

5.8 Structural Analysis of Photoelectrodeposits

Figure 5.12 presents a Raman spectrum representative of the Se-Te photoelectrodeposits generated in this work. The spectrum displays modes centered at 96 cm^{-1}, 120 cm^{-1}, 170 cm^{-1}, 201 cm^{-1}, and 240 cm^{-1}. The presence of these modes is consistent

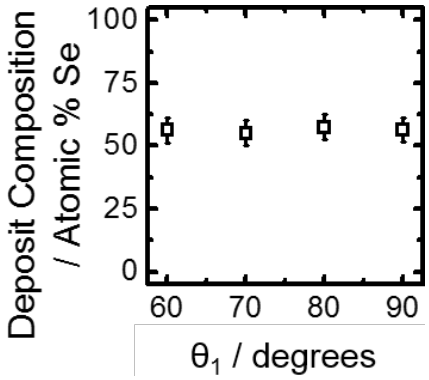

Figure 5.10: Plot of the elemental composition, in terms of atomic % of Se, of photoelectrodeposits generated using two incoherent LED sources with λ_{avg} = 630 nm and equal intensity, the first source polarized vertically (θ_0 = 0 °) and the second at a defined rotation (θ_1) clockwise from the vertical, as a function of θ_1. Photoelectrodeposits were composed wholly of Se and Te.

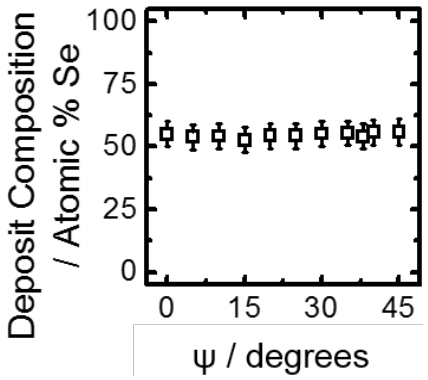

Figure 5.11: Plot of the elemental composition, in terms of atomic % of Se, of photoelectrodeposits, generated using a HeNe laser with λ_{avg} = 632.8 nm with defined elliptical polarizations wherein $\psi = \chi$, as a function of ψ. ψ indicates the orientation of the major axis of the ellipse measured clockwise from the vertical. χ represents the angle between the major axis and a line connecting a vertex on the major axis with one on the minor axis and relates the eccentricity and asymmetry of the ellipse. Photoelectrodeposits were composed wholly of Se and Te.

with the presence of a substitutional alloy of Se and Te in a hexagonal (trigonal) structure common to both elements in their pure phases.[99]

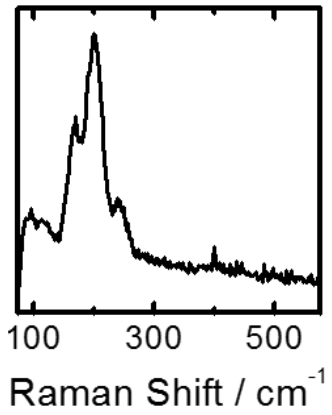

Figure 5.12: Raman spectrum of a Se-Te photoelectrodeposit generated using an incoherent LED source with λ_{avg} = 630 nm.

Chapter 6

SUMMARY AND OUTLOOK

The work presented in this thesis details a maskless, bottom-up patterning technique based on photoelectrodeposition which allows the direct fabrication of periodically-nanostructured thin films of semiconductor material over macroscale substrates.

In chapter II we demonstrated that a single source can be used to define the period, orientation and angle of the films by tuning the wavelength, polarization axis and incidence angle of illumination respectively. We developed an understanding of the pattern formation to be the result of interference of light scattered across the surface of the interface. By building a probabilistic computational model that correlates the local light absorption with the local growth rate at the interface of the film we were able to reproduce the lamellar morphology observed experimentally.

In Chapter III we investigated pattern formation while illuminating the substrate with two mutually incoherent sources having different illumination wavelengths. We observed that the period of patterned films adopted a period intermediate to that of a film deposited under either source alone. We observed that our computational model quantitatively reproduced the same period. We defined a figure of merit which represented the anisotropy of light absorption between the lamellae tops and rest of the film. By calculating the light absorption in representative structures of the lamellar films we observed that the lamellar structures adopted a period to maximize the anisotropy of light absorption

In Chapter IV we investigated pattern formation under two mutually incoherent sources with differing polarizations. We found that when the polarization angles of the two sources had a difference of $\leq 60°$ a lamellar morphology similar to that of one source with an intensity weighted polarization of two sources. In contrast, when the two sources were polarized orthogonally, the a morphology developed with two intersecting sets of lamellae. Furthermore, we found the periodicities could be independently tuned by using different source wavelengths. We generalized our computational model to three dimensions and observed that it produced films which exhibited the same features as our experimental results. We constructed ideal intersecting lamellae based on our experimental parameters and simulated the absorption profile due to each source. We found that the absorption profile on each

set of lamellae was dominated by the source polarized parallel to the long axis of the structure.

In chapter V we furthered our understanding of the previous investigation by examining the effect of mutual coherence between two sources with differing polarizations. We observed that the time averaged polarization intensity could be tuned to effect the anisotropy of the structures. Our computational model was again used to show that the morphologies could be quantitatively reproduced through a simple relationship of local absorption and growth. This finding suggests that the film morphology can be tuned by changing the relative phase or angle between two mutually coherent sources.

The electrodeposition process we have outlined in this thesis provides an arbitrarily large parameter space for directly synthesizing nanopatterned semiconductor films. Further experimental conditions to investigate include the substrate geometry, deposition solution index and temperature, and time dependence of illumination conditions, and deposition material. Thus, there are numerous opportunities for further scientific and application-based investigation. A more complex computational model would allow us to make more detailed predictions about the growth rate and deposit morphology prior to performing experiments. Some considerations to further improve the model are surface adatom diffusion and nucleation, solution-deposit interface dynamics, electrical charge transport through the deposit and near the interface and ionic species transport in the solution.

Many applications of nanostructures such as diffractive optics or polarization selective optical elements require highly ordered structures. A systematic study of parameters that affect film disorder would be useful in understanding the limits of order in films deposited in this manner.

Additionally, the encoding of optical input polarization and relative phase in non-volatile physical media is immediately relevant to advanced polarization holography. In this technique, data is written by using two polarized optical beams with arbitrary phase differences in summation to generate unique morphologies that are characteristic of the polarizations and relative phases of the writing beams. Polarization holography can provide significantly higher volumetric data storage capacity than conventional holography and thus is of potential interest for application in high density optical storage of digital data.[96–98]

Electronic devices, such as photovoltaics and integrated circuits generally require

high quality semiconductor materials to operate at practical efficiencies. To this end, an investigation on increased charge-carrier mobility and lifetime on the photoelectrodeposited film's morphology could provide valuable insight on incorporating the above outlined photoelectrodeposition process on the fabrication of such devices. For example, it is not yet known if an increased electronic mobility would enable photogenerated carriers to drive material growth in a more diffused manner, thus causing the lamellar patterns to "wash out". Our simulations of the process have thus far assumed that photogenerated carriers could only drive deposition if they were generated at the interface and could not diffuse from the location where they were generated. The inclusion of charge transport effects in the model would enable predictions regarding the morphological dependence on material quality, and the feasibility of using the above outlined process for the fabrication of useful electronic devices.

Appendix A

GROWTH SIMULATION SOFTWARE

Over the duration of time that the work included in this thesis was carried out, a program consisting of matlab and lumerical scripts was developed to simulate the growth of semiconductor nanostructures via electrodeoposition. The code is freely available at github.com/nbatara/o_lmg. As described in the previous chapters, these simulations were based on iteratively calculating the absorption of a film and evolving the structure based on the mass. It was written for use on Mac OS X and Linux based systems with the assumption that Lumerical FDTD and Matlab are installed in the default installation directories. The following is a description of the simulation code base as of October 2016.

A.1 Installing the Software

The software can be downloaded either at the hyperlink above or through a command line interface with "git clone https://github.com/nbatara/o_lmg.git".

A.2 Included Files

lmgSetup.m : Prompts user for simulation parameters and assembles simulation directories

lmg.fsp : Lumerical simulation file which includes modified analysis groups and optical constants for growth material

setup.lsf : Sets up initial simulation

nCores.txt : Specifies number of simulation cores to use during each simulation.

lmgAnalysis.m : Analyzes simulation results. Saves images of final structure.

run_lmg.m : Runs simulations in each directory by calling lmg.m

lmg_update.lsf : Creates next .fsp iteration using the previous iteration and a structure file

lmg_extract.lsf : Extracts absorption data from .fsp simulation, saves data as .mat, and returns simulation to layout mode in order to save disk space.

lmg.m : Main script which keeps track of simulation status, calls lmg_update.lsf and lmg_extract.lsf to update FDTD simulation and extract results respectively.

A.3 Starting simulations

A batch of simulations can be setup by running lmgSetup.m. An window will appear which provides field for the simulation parameters (A.1). Multiple identical simulations can be specified by setting the number of simulations to greater than one while only providing one value for each of the other inputs. Alternatively, a parameter sweep can be constructed by providing a set of parameters separated by spaces that is equal to the number of simulations. After hitting "ok" the script will create a directory of containing simulation directories and necessary files.

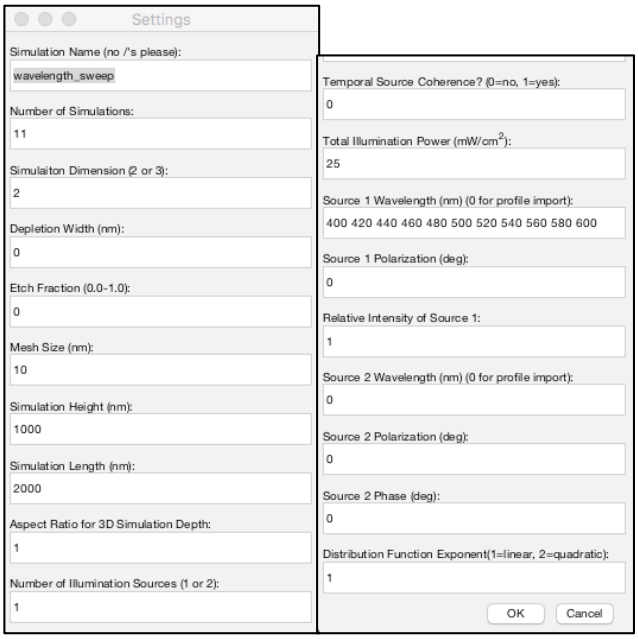

Figure A.1: Graphical interface for setting up a batch of simulations.

A.4 Running Simulations

The user can transfer the batch directory to a machine (node) suitable for the size of the simulation. Typically, two dimensional simulations with a simulation length below 10 μm and a mesh size of $\geq$ 2nm can be executed on a personal computer (2-4 cores, 4-16 GB RAM) at the time of writing this thesis. Three dimensional simulations ideally should be run on many core system with $\geq$ 16 GB of RAM for simulation size greater than 500 x 500 x 1000 nm with a mesh size of 10 nm. The batch of simulations can be run by navigating to the batch directory in the Matlab environment and executing the run_lmg.m script. This script will successively run each individual simulation and use the number of simulation cores specified in nCores.txt for the FDTD calculations. Multiple concurrent calls to run_lmg.m can

be made by opening multiple instances of Matlab. In this case, multiple simulations can be run at the same time however, the user should be aware of the total number of cores and total memory available to avoid locking up the system.

A.5 Software Flow Charts

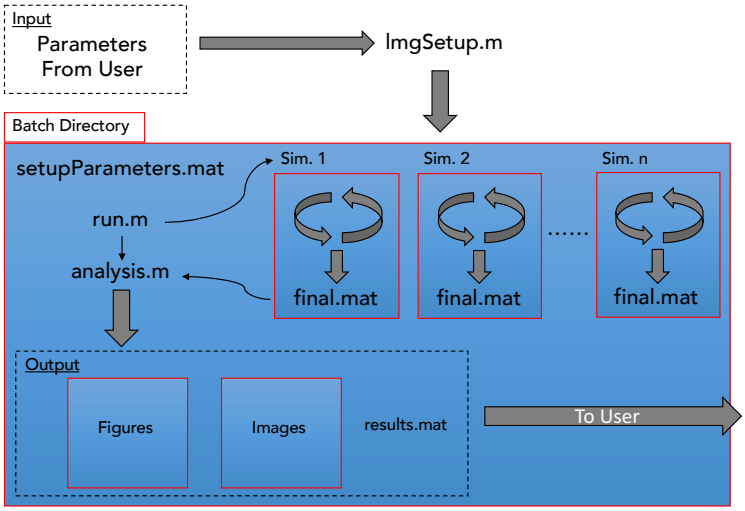

Figure A.2: Software flowchart for a batch of simulations.

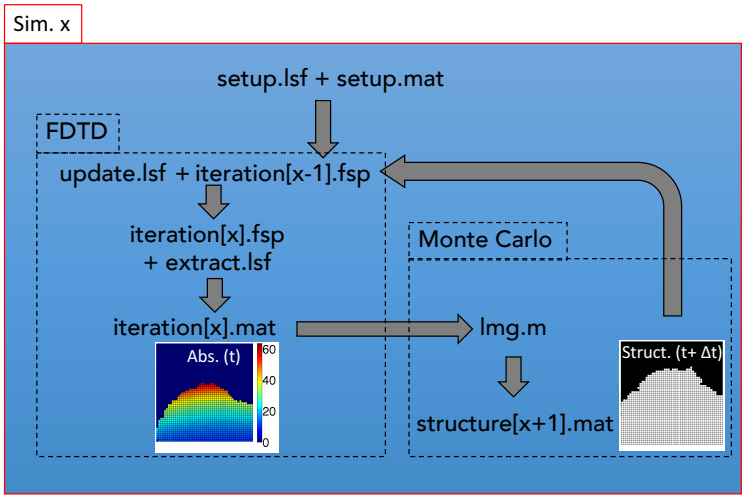

Figure A.3: Software flowchart for individual simulation within a batch.

A.6 Analyzing Simulations

After all simulations have finished, the analysis script (lmgAnalysis.m) will be called to produce figures and images of the simulations separate sub-directories. These figures and images can be analyzed for features such as periodicity through fourier analysis.

BIBLIOGRAPHY

1. Chen, G., Imanishi, Y. & Ito, Y. pH-Sensitive Thin Hydrogel Microfabricated by Photolithography. *Langmuir* **14,** 6610–6612 (1998).

2. Revzin, A., Russell, R. J., Yadavalli, V. K., Koh, W.-G., Deister, C., Hile, D. D., Mellott, M. B. & Pishko, M. V. Fabrication of Poly(ethylene glycol) Hydrogel Microstructures Using Photolithography. *Langmuir* **17,** 5440–5447 (2001).

3. Totzeck, M., Ulrich, W., Göhnermeier, A. & Kaiser, W. Pushing Deep Ultraviolet Lithography to its Limits. *Nature Photonics* **1,** 629–631 (2007).

4. Kik, P. G., Martin, A. L., Maier, S. A. & Atwater, H. A. Metal nanoparticle arrays for near-field optical lithography. *Proceedings of SPIE* **4810,** 7–13 (2002).

5. Luo, X. & Ishihara, T. Surface plasmon resonant interference nanolithography technique. *Applied Physics Letters* **84,** 4780–4782 (2004).

6. Srituravanich, W., Fang, N., Sun, C., Luo, Q. & Zhang, X. Plasmonic nanolithography. *Nano Letters* **4,** 1085–1088 (2004).

7. Shao, D. B. & Chen, S. C. Direct patterning of three-dimensional periodic nanostructures by surface-plasmon-assisted nanolithography. *Nano Letters* **6,** 2279–2283 (2006).

8. Campbell, M., Sharp, D. N., Harrison, M. T., Denning, R. G. & Turberfield, A. J. Fabrication of photonic crystals for the visible spectrum by holographic lithography. *Nature* **404,** 53–56 (2000).

9. Jeon, S., Park, J.-U., Cirelli, R., Yang, S., Heitzman, C. E., Braun, P. V., Kenis, P. J. A. & Rogers, J. A. Fabricating complex three-dimensional nanostructures with high-resolution conformal phase masks. *Proceedings of the National Academy of Sciences* **101,** 12428–12433 (2004).

10. Arnold, C. B., Serra, P. & Piqué, A. Laser direct-write techniques for printing of complex materials. *MRS Bulletin-Materials Research Society* **32,** 23–31 (Jan. 2007).

11. Deutsch, T. F., Ehrlich, D. J. & Osgood, R. M. Laser Photodeposition of Metal-Films with Microscopic Features. *Applied Physics Letters* **35,** 175–177 (1979).

12. Tsao, J. Y. & Ehrlich, D. J. Patterned Photonucleation of Chemical Vapor-Deposition of Al by UV-Laser Photodeposition. *Applied Physics Letters* **45,** 617–619 (1984).

13. Rauh, R. D. & LeLievre, R. A. Microphotoelectrochemical Etching of n-GaAs Using a Scanned Focused Laser. *Journal of the Electrochemical Society* **132,** 2811–2812 (1985).

14. Destouches, N., Crespo-Monteiro, N., Vitrant, G., Lefkir, Y., Reynaud, S., Epicier, T., Liu, Y., Vocanson, F. & Pigeon, F. Self-organized growth of metallic nanoparticles in a thin film under homogeneous and continuous-wave light excitation. *Journal of Materials Chemistry C* **2,** 6256–6263 (2014).

15. Langille, M. R., Personick, M. L. & Mirkin, C. A. Plasmon-Mediated Syntheses of Metallic Nanostructures. *Angewandte Chemie International Edition* **52,** 13910–13940 (Dec. 2013).

16. Grzelczak, M. & Liz-Marzán, L. M. The relevance of light in the formation of colloidal metal nanoparticles. *Chem Soc Rev* **43,** 2089–2097 (Apr. 2014).

17. Temple, P. A. & Soileau, M. J. Polarization charge model for laser-induced ripple patterns on dielectric materials. *IEEE Journal of Quantum Electronics* **17,** 2067–2072 (1981).

18. Young, J. F., Sipe, J. E., Preston, J. S. & van Driel, H. M. Laser-induced periodic surface damage and radiation remnants. *Applied Physics Letters* **41,** 261–264 (1982).

19. Van Driel, H. M., Sipe, J. E. & Young, J. F. Laser-induced periodic surface structure on solids: A universal phenomenon. *Physical Review Letters* **49,** 1955–1958 (1982).

20. Sipe, J. E., Young, J. F., Preston, J. S. & van Driel, H. M. Laser-induced periodic surface structure. I. Theory. *Physical Review B* **27,** 1141–1154 (1983).

21. Siegman, A. E. & Fauchet, P. M. Stimulated Wood's anomalies on laser-illuminated surfaces. *IEEE Journal of Quantum Electronics* **22,** 1384–1403 (1986).

22. Tull, B. R., Carey, J. E., Mazur, E., McDonald, J. P. & Yalisove, S. M. Silicon surface morphologies after femtosecond laser irradiation. *MRS bulletin* **31,** 626–633 (2006).

23. Haller, K. L., Bumm, L. A., Altkorn, R. I., Zeman, E. J., Schatz, G. C. & Van Duyne, R. P. Spatially resolved surface enhanced second harmonic generation: Theoretical and experimental evidence for electromagnetic enhancement in the near infrared on a laser microfabricated Pt surface. *Journal of Chemical Physics* **90,** 1237–1252 (1989).

24. Brueck, S. R. J. & Ehrlich, D. J. Stimulated Surface-Plasma-Wave Scattering and Growth of a Periodic Structure in Laser-Photodeposited Metal Films. *Physical Review Letters* **48,** 1678–1681 (1982).

25. Wilson, R. J. & Houle, F. A. Composition, structure, and electric field variations in photodeposition. *Physical Review Letters* **55,** 2184–2187 (Nov. 1985).

26. Birnbaum, M. Semiconductor Surface Damage Produced by Ruby Lasers. *Journal of Applied Physics* **36,** 3688–3689 (1965).

27. Isenor, N. R. CO2 laser-produced ripple patterns on NixP1-x surfaces. *Applied Physics Letters* **31,** 148–150 (1977).

28. Young, J. F., Preston, J. S., van Driel, H. M. & Sipe, J. E. Laser-Induced Periodic Surface Structuring. II. Experiments on Ge, Si, Al, and brass. *Physical Review B* **27,** 1155–1172 (1983).

29. Osgood, R. M. & Ehrlich, D. J. Optically induced microstructures in laser-photodeposited metal films. *Optics Letters* **7,** 385–387 (1982).

30. Wilson, R. J. & Houle, F. A. Composition, structure, and electric field variations in photodeposition. *Physical Review Letters* **55,** 2184–2187 (1985).

31. Jelski, D. A. & George, T. F. Dynamics of patterned laser-induced chemical vapor deposition. *Journal of Applied Physics* **61,** 2353–2357 (1987).

32. Vlasov, Y. A., Bo, X.-Z., Sturm, J. C. & Norris, D. J. On-chip natural assembly of silicon photonic bandgap crystals. *Nature* **414,** 289–293 (2001).

33. Sveinbjornsson, B. R., Weitekamp, R. A., Miyake, G. M., Xia, Y., Atwater, H. A. & Grubbs, R. H. Rapid self-assembly of brush block copolymers to photonic crystals. *Proceedings of the National Academy of Sciences* **109,** 14332–14336 (2012).

34. Arpin, K. A., Mihi, A., Johnson, H. T., Baca, A. J., Rogers, J. A., Lewis, J. A. & Braun, P. V. Multidimensional architectures for functional optical devices. *Advanced Materials* **22,** 1084–1101 (2010).

35. Braun, P. V. & Wiltzius, P. Electrochemically grown photonic crystals. *Nature* **402,** 603–604 (1999).

36. Nishimura, S., Abrams, N., Lewis, B. A., Halaoui, L. I., Mallouk, T. E., Benkstein, K. D., van de Lagemaat, J. & Frank, A. J. Standing wave enhancement of red absorbance and photocurrent in dye-sensitized titanium dioxide photoelectrodes coupled to photonic crystals. *Journal of the American Chemical Society* **125,** 6306–6310 (2003).

37. Zhang, H., Yu, X. & Braun, P. V. Three-dimensional bicontinuous ultrafast-charge and -discharge bulk battery electrodes. *Nature Nanotechnology* **6,** 277–281 (2011).

38. McKone, J., Warren, E. L., Bierman, M. J., Boettcher, S. W., Brunschwig, B. S., Lewis, N. S. & Gray, H. B. Evaluation of Pt, Ni, and Ni-Mo electrocatalysts for hydrogen evolution on crystalline Si electrodes. *Energy & Environmental Science* **4,** 3573–3583 (2011).

39. Gansel, J. K., Thiel, M., Rill, M. S., Decker, M., Bade, K., Saile, V., von Freymann, G., Linden, S. & Wegener, M. Gold helix photonic metamaterial as broadband circular polarizer. *Science* **325,** 1513–1515 (2009).

40. Shelby, R. A., Smith, D. R. & Schultz, S. Experimental verification of a negative index of refraction. *Science* **292,** 77–79 (2001).

41. Lezec, H. J., Dionne, J. A. & Atwater, H. A. Negative refraction at visible frequencies. *Science* **316,** 430–432 (2007).

42. Cao, L., White, J. S., Park, J.-S., Schuller, J. A., Clemens, B. M. & Brongersma, M. L. Engineering light absorption in semiconductor nanowire devices. *Nature Materials* **8,** 643–647 (2009).

43. Knight, M. W., Sobhani, H., Nordlander, P. & Halas, N. J. Photodetection with Active Optical Antennas. *Science* **332,** 702–704 (2011).

44. Jin, R., Cao, Y. W., Mirkin, C. A., Kelly, K. L., Schatz, G. C. & Zheng, J. G. Photoinduced conversion of silver nanospheres to nanoprisms. *Science* **294,** 1901–1903 (2001).

45. Jin, R., Cao, Y. C., Hao, E., Métraux, G. S., Schatz, G. C. & Mirkin, C. A. Controlling anisotropic nanoparticle growth through plasmonic excitation. *Nature* **425,** 487–490 (Oct. 2003).

46. Maillard, M., Huang, P. & Brus, L. Silver Nanodisk Growht by Surface Plasmon Enhanced Photoreduction of Adsorbed [Ag+]. *Nano Letters* **3,** 1611–1615 (2003).

47. Lincot, D. Electrodeposition of semiconductors. *Thin Solid Films* **487,** 40–48 (Sept. 2005).

48. Ray, A. in *Electroplating of Nanostructures* (InTech, Dec. 2015).

49. BASOL, B. M. Electrodeposited Cdte and Hgcdte Solar-Cells. *Solar Cells* **23,** 69–88 (1988).

50. Carim, A. I., Batara, N. A., Premkumar, A., Atwater, H. A. & Lewis, N. S. Polarization Control of Morphological Pattern Orientation During Light-Mediated Synthesis of Nanostructured Se–Te Films. *ACS Nano* **10,** 102–111 (Jan. 2016).

51. Carim, A. I., Batara, N. A., Premkumar, A., Atwater, H. A. & Lewis, N. S. Self-Optimizing Photoelectrochemical Growth of Nanopatterned Se–Te Films in Response to the Spectral Distribution of Incident Illumination. *Nano Letters* **15,** 7071–7076 (Oct. 2015).

52. Sze, S. M. & Ng, K. K. *Physics of Semiconductor Devices* (John Wiley & Sons, Hoboken, New Jersey, 2007).

53. Warren, E. L., Boettcher, S. W. & Lewis, N. S. Solar Water Splitting Cells. *Chemical Reviews* **110,** 6446–6473 (Nov. 2010).

54. Bard, A. & Faulkner, L. *Electrochemical methods: fundamentals and applications* (Wiley New York, 2001).

55. Bockris, J. O., Reddy, A. K. N. & Gamboa-Aldeco, M. E. *Modern Electrochemistry 2A* (Springer Science & Business Media, 2002).

56. Pandey, R. K., Sahu, S. N. & Chandra, S. *Handbook of Semiconductor Electrodeposition* (New York: Marcel Dekker, 1996).

57. Mayers, B., Gates, B., Yin, Y. & Xia, Y. Large-scale synthesis of monodisperse nanorods of Se/Te alloys through a homogeneous nucleation and solution growth process. *Advanced Materials* **13,** 1380–1384 (2001).

58. Mikla, V. I. Photoinduced structural changes and related phenomena in amorphous arsenic chalcogenides. *Journal of Physics: Condensed Matter* **8,** 429–448 (1996).

59. Prieto-Alcon, R., Marquez, E., Gonzalez-Leal, J. M., Jimenez-Garay, R., Kolobov, A. V. & Frumar, M. Reversible and athermal photo-vitrification of As50Se50 thin films deposited onto silicon wafer and glass substrates. *Applied Physics A* **68,** 653–661 (1999).

60. Young, J. F., Preston, J. S., van Driel, H. M. & Sipe, J. E. Laser-induced periodic surface structure. II. Experiments on Ge, Si, Al, and brass. *Physical Review B* **27,** 1155–1172 (1983).

61. Sipe, J. E., Young, J. F., Preston, J. S. & van Driel, H. M. Laser-induced periodic surface structure. I. Theory. *Physical Review B* **27,** 1141–1154 (1983).

62. El-Korashy, A., El-Zahed, H., Zayed, H. A. & Kenawy, M. A. Effect of composition and structure on electrical conduction of Se(100-x)Te(x) films. *Solid state communications* **95,** 335–339 (1995).

63. Mott, N. F. & Davis, E. A. *Electronic Processes in Non-Crystalline Materials* (Clarendon-Press, Oxford, 1971).

64. Reznik, A., Klebanov, M. & Lyubin, V. Transient photorefraction in a-Se films. *Journal of Applied Physics* **105,** 013518–1–4 (2009).

65. Gueguen, Y., Sangleboeuf, J. C., Keryvin, V., Lépine, E., Yang, Z., Rouxel, T., Point, C., Bureau, B., Zhang, X.-H. & Lucas, P. Photoinduced fluidity in chalcogenide glasses at low and high intensities: A model accounting for photon efficiency. *Physical Review B* **82,** 134114 1–12 (2010).

66. Ishida, K. & Tanaka, K. Photoinduced anisotropic crysallization of amorphous Se. *Physical Review B* **56,** 206–209 (1997).

67. Shimakawa, K. Photon effects in chalcogenide glasses. *Journal of Optoelectronics and Advanced Materials* **9,** 2973–2978 (2007).

68. Trunov, M. L., Nagy, P. M., Takats, V., Lytvyn, P. M., Kokenyesi, S. & Kalman, E. Surface morphology of as-deposited and illuminated As-Se chalcogenide thin films. *Journal of Non-Crystalline Solids* **355,** 1993–1997 (2009).

69. Adachi, H. & Kao, K. C. Dispersive optical constants of amorphous Se1-xTex films. *Journal of Applied Physics* **51,** 6326–6331 (1980).

70. Beyer, W., Mell, H. & Stuke, J. Conductivity and thermoelectric power of trigonal SexTe1-x single crystals. *physica status solidi (b)* **45,** 153–162 (1971).

71. Bhatnagar, A. K., Srivastava, V. & Reddy, K. Te substitution in disordered dilute Se1-xTex alloys. *Applied Physics Letters* **73,** 2426–2428 (1998).

72. Reddy, K. V. & Bhatnagar, A. K. Electrical and optical studies on amorphous Se-Te alloys. *Journal of Physics D: Applied Physics* **25,** 1810–1816 (1992).

73. Kelzenberg, M. D. *Silicon Microwire Photovoltaics* PhD thesis (California Instute of Technology, 2010).

74. Sadtler, B., Burgos, S. P., Batara, N. A., Beardslee, J. A., Atwater, H. A. & Lewis, N. S. Phototropic growth control of nanoscale pattern formation in photoelectrodeposited Se-Te films. *Proceedings of the National Academy of Sciences of the United States of America* **110,** 19707–19712 (Dec. 2013).

75. Hale, G. M. & Querry, M. R. Optical Constants of Water in the 200-nm to 200-μm Wavelength Region. *Appl. Opt.* **12,** 555–563 (1973).

76. Gibbons, W. M., Shannon, P. J., Sun, S.-T. & Swetlin, B. J. Surface-Mediated Alignment of Nematic Crystals with Polarized Laser Light. *Nature (London, United Kingdom)* **351,** 49–50 (1991).

77. Shannon, P. J., Gibbons, W. M. & Sun, S.-T. Patterned Optical Properties in Photopolymerized Surface-Aligned Liquid-Crystal Films. *Nature (London, United Kingdom)* **368,** 532–533 (1994).

78. Ichimura, K. Photoalignment of Liquid-Crystal Systems. *Chemical Reviews* **100,** 1847–1873 (2000).

79. Barrett, C. J., Nathansohn, A. L. & Rochon, P. L. Mechanism of Optically Inscribed High-Efficiency Diffraction Gratings in Azo Polymer Films. *J. Phys. Chem.* **100,** 8836–8842 (1996).

80. Hubert, C., Rumyantseva, A., Lerondel, G., Grand, J., Kostcheev, S., Billot, L., Vial, A., Bachelot, R., Royer, P., Chang, S.-h., Gray, S. K., Wiederrecht, G. P. & Schatz, G. C. Near-Field Photochemical Imaging of Noble Metal Nanostructures. *Nano Letters* **5,** 615–619 (2005).

81. Hubert, C., Bachelot, R., Plain, J., Kostcheev, S., Lerondel, G., Juan, M., Royer, P., Zou, S., Schatz, G. C., Wiederrecht, G. P. & Gray, S. K. Near-Field Polarization Effects in Molecular-Motion-Induced Photochemical Imaging. *The Journal of Physical Chemistry C* **112,** 4111–4116 (2008).

82. Plain, J., Wiederrecht, G. P., Gray, S. K., Royer, P. & Bachelot, R. Multi-scale Optical Imaging of Complex Fields Based on the Use of Azobenzene Nanomotors. *The Journal of Physical Chemistry Letters* **4,** 2124–2132 (2013).

83. Ishitobi, H., Nakamura, I., Kobayashi, T.-a., Hayazawa, N., Sekkat, Z., Kawata, S. & Inouye, Y. Nanomovement of Azo Polymers Induced by Longitudinal Fields. *ACS Photonics* **1,** 190–197 (2014).

84. Paul, A., Kenens, B., Hofkens, J. & Uji-i, H. Excitation Polarization Sensitivity of Plasmon-Mediated Silver Nanotriangle Growth on a Surface. *Langmuir* **28,** 8920–8925 (June 2012).

85. Yin, A. J., Li, J., Jian, W., Bennett, A. J. & Xu, J. M. Fabrication of Highly Ordered Metallic Nanowire Arrays by Electrodeposition. *Applied Physics Letters* **79,** 1039 (2001).

86. Sander, M. S., Prieto, A. L., Gronsky, R. & Stacy, A. M. Fabrication of High-Density, High Aspect Ratio, Large-Area Bismuth Telluride Nanowire Arrays by Electrodeposition into Porous Anodic Alumina Templates. *Advanced Materials (Weinheim, Germany)* **14,** 665–667 (2002).

87. Choi, K.-S., Lichtenegger, H. C., Stucky, G. D. & McFarland, E. W. Electrochemical Synthesis of Nanostructured ZnO Films Utilizing Self-Assembly of Surfactant Molecules at Solid-Liquid Interfaces. *Journal of the American Chemical Society* **124,** 12402–12403 (2002).

88. Choi, K.-S. Shape Control of Inorganic Materials via Electrodeposition. *Dalton Transactions,* 5432–5438 (2008).

89. Attard, A. E. & Brown, D. E. Photoelectroplating Light Modulator. *Applied optics* **7,** 511–516 (1968).

90. Inoue, T., Fujishima, A. & Honda, K. Photoelectrochromic Characteristics of Photoelectrochemical Imaging System with a Semiconductor/Solution (Metallic Ion) Junction. *J. Electrochem. Soc.* **127,** 1582–1588 (1980).

91. Kildishev, A. V., Boltasseva, A. & Shalaev, V. M. Planar Photonics with Metasurfaces. *Science* **339,** 1232009 (Mar. 2013).

92. Verslegers, L., Catrysse, P. B., Yu, Z., White, J. S., Barnard, E. S., Brongersma, M. L. & Fan, S. Planar Lenses Based on Nanoscale Slit Arrays in a Metallic Film. *Nano Letters* **9,** 235–238 (2009).

93. Fattal, D., Li, J., Peng, Z., Fiorentino, M. & Beausoleil, R. G. Flat Dielectric Grating Reflectors with Focusing Abilities. *Nature Photonics* **4,** 466–470 (2009).

94. Chen, Z., Cummins, D., Reinecke, B. N., Clark, E., Sunkara, M. K. & Jaramillo, T. F. Core–shell MoO 3–MoS 2Nanowires for Hydrogen Evolution: A Functional Design for Electrocatalytic Materials. *Nano Letters* **11,** 4168–4175 (Oct. 2011).

95. Kong, D., Wang, H., Lu, Z. & Cui, Y. CoSe 2Nanoparticles Grown on Carbon Fiber Paper: An Efficient and Stable Electrocatalyst for Hydrogen Evolution Reaction. *Journal of the American Chemical Society* **136,** 4897–4900 (Apr. 2014).

96. Todorov, T., Nikolova, L., Stoyanova, K. & Tomova, N. Polarization holography. 3: Some applications of polarization holographic recording. *Applied optics* **24,** 785–788 (1985).

97. Kuroda, K., Matsuhashi, Y., Fujimura, R. & Shimura, T. Theory of Polarization Holography. *Opt. Rev.* **18,** 374–382 (2011).

98. Kawatsuki, N., Hasegawa, T., Ono, H. & Tamoto, T. Formation of Polarization Gratings and Surface Relief Gratings in Photocrosslinkable Polymer Liquid Crystals by Polarization Holography. *Advanced Materials (Weinheim, Germany)* **15,** 991–994 (2003).

99. Geick, R., Steigmeier, E. F. & Auderset, H. Raman Effect in Selenium-Tellurium Mixed Crystals. *Physica Status Solidi B: Basic Research* **54,** 623–630 (1972).